1-1-2010

Electro-Hydraulic Servo-Valve and Motion and Control Loading of Full Flight Simulator

Wei Shi
Ryerson University

ELECTRO-HYDRAULIC SERVO-VALVE AND MOTION AND CONTROL LOADING OF FULL FLIGHT SIMULATOR

by

WEI SHI

BAS (Applied Physics), Sichuan University, China, 1991

A thesis

presented to Ryerson University

in partial fulfilment of the

requirements for the degree of

Master of Applied Science

in the Program of

Aerospace Engineering

Toronto, Ontario, Canada, 2010

AUTHOR'S DECLARATION

I hereby declare that I am the sole author of this thesis.

I authorize Ryerson University to lend this thesis to other institutions or individuals for the purpose of scholarly research.

*

I further authorize Ryerson University to reproduce this thesis by photocopying or by other means, in total or in part, at the request of other institutions or individuals for the purpose of scholarly research.

*

ABSTRACT

ELECTRO-HYDRAULIC SERVO-VALVE AND

MOTION AND CONTROL LOADING OF FULL FLIGHT SIMULATOR

Master of Applied Science, 2010

Aerospace Engineering

By Wei Shi, Ryerson University

The present thesis is on the subject of electro-hydraulic servo-valve (EHV), and motion and control loading of a flight simulator with EHV. The fundamentals of EHV and hydraulic control systems are discussed in Part A. An electro-hydraulic servo-valve (MOOG 760 series) and a position servo control were constructed using an EHV and a linear hydraulic double-ended cylinder, which was modeled mathematically and implemented symbolically by Simulink.

Part B examines the motion and control loading systems of a full flight simulator. Motion simulation algorithms and implementation are discussed in moderate depth. As a generic example, a typical elevator control loading channel is represented in state space; whose stability, linkage compliance and control scheme implementation analysis are conducted in detail by means of MATLAB. The same elevator control loading channel was symbolically modelled through Simulink, based on the EHV/actuator model that was developed in Part A. The results of different control schemes are discussed and compared.

ACKNOWLEDGEMENTS

The simulation of aircraft motion and control loading is a complicated task involving multiple disciplines. This thesis is based on knowledge learned in several Ryerson University graduate courses—advanced system control, advanced fluid dynamics, computational dynamics, multi-disciplinary design optimization of aerospace systems, and flight dynamics and control of aircraft.

The support and assistance of Professor G. Liu, Ryerson University, is gratefully acknowledged.

The experience of working hands-on with flight simulators, and all the training received at Flight Safety Int. have helped me to ensure the integrity of this thesis, which is greatly appreciated. Also, without the tuition assistance received from Flight Safety Int., there would be no premise in the endeavour of this MASc Degree.

DEDICATION

Without the unconditional love, patience and support of my family, finishing my graduate study and this thesis would have been impossible. Greatest thanks to my parents, my wife, my son, and my daughter.

TABLE OF CONTENTS

AUTHOR'S DECLARATION II

ABSTRACT III

AKNOWLEDGMENTS IV

DEDICATION V

TABLE OF CONTENTS VI

LIST OF FIGURES VIII

LIST OF EQUATION XI

NOMENCLATURE XIII

Part A: Electro-hydraulic Servo-valve 1

1: Background 1

2: Objective 3

2.1 EHV 3

2.2 Linear hydraulic actuator 4

2.3 Hydraulic control system 4

3: Mathematical modelling 6

3.1Torque motor 6

3.2 Valve spool 6

3.3 Valve flow Pressure 7

3.4 Piston dynamics 10

4: MATLAB simulation 11

5: Parameter table 12

6: Simulation results and discussion 14

6.1 EHV step response 14

6.2 Cylinder position response 16

6.3 Sinusoidal response 17

7: Summary of Part A 20

Part B: Simulator Motion and Control Loading 21
8: Introduction 21
9: Motion simulation 22
9.1 Aircraft motion equation 22
9.2 Control derivatives 24
9.3 History of simulator motion 26
9.4 Motion simulation algorithm 29
9.5 Digital simulator motion system 34
10: Control loading simulation 38
10.1 Aircraft control system 38
10.2 Control surface dynamics 40
10.3 Simulator Aero Surface Model 42
10.4 Analog electro-hydraulic control loading system 43
10.5 State space representation 45
10.6 Stability analysis 49
10.7Regulatory Requirement 51
10.8 State space model results and discussion 53
10.9 Control loading Simulink model 58
10.9.1 Position follower 59
10.9.2 Velocity follower 63
10.10 Digital control loading system 66
11: Electric Motion and Control Loading 70
12: Conclusions 72
References 74
Appendix A: Simulink Block 77
Appendix B: MATLAB Code 86

LIST OF FIGURES

Fig.1 Block schematic of simulator interconnections 2

Fig.2 Potential component contributions to control loading 2

Fig.3 Cross section of nozzle-flapper type servo-valve 3

Fig.4 Linear servo-hydraulic actuator assemblies 4

Fig.5 Block diagram of a position control hydraulic servo system.....5

Fig.6 Physical model of electro-hydraulic servo-system 5

Fig.7 Servo-valve frequency response curve 7

Fig.8 Servo-valve spool configuration 8

Fig.9 Top level system diagram 11

Fig.10 EHV system diagram 12

Fig.11 Actuator system diagram 12

Fig.12 EHV spool displacement and flow step responses 14

Fig.13 Cylinder chamber pressure responses 15

Fig.14 Cylinder position response 16

Fig.15 Pulse responses 18

Fig.16 Sinusoidal responses 19

Fig.17 Notation for body axes 22

Fig.18 1909 training rig for the Antoinette aircraft with pilot seat in a half-barrel 26

Fig.19 Link Trainer.....27

Fig.20 Roeder's aeroplane model 28

Fig.21 Thales flight simulator at a pitch angle 29

Fig.22 Acceleration onset cueing 30

Fig.23 Six-post synergistic motion system 31

Fig.24 Tilting the platform to provide surge acceleration 31

Fig.25 Typical flight simulator installation 32

Fig.26 Classical motion algorithm 33

Fig.27 Simplified motion system block diagram and hardware diagram 34

Fig.28 Motion simulation algorithm (primary motion module block and motion control module).....35

Fig.29 Motion servo block diagram 37

Fig.30 Example of a typical reversible flight control system 38

Fig.31 Example of a typical irreversible flight control system 39

Fig.32 Q-feel system 40

Fig.33 Elevator and tab geometry 41

Fig.34 Schematic diagram of an elevator control system 41

Fig.35 Single mass aircraft control surface model 43

Fig.36 Electro-hydraulic control loading system 44

Fig.37 Rigid and compliant linkage models 45

Fig.38 $\boldsymbol{\delta/e_T}$ Bode diagram (open outer loop).....50

Fig.39 Under-damped step response.....52

Fig.40 Critically and over-damped step response 53

Fig.41 Trim force T step responses (lower damp case) 54

Fig.42 Trim force T step responses (high damp case) 55

Fig.43 Pilot force Fp step responses (lower damp case).....56

Fig.44 Pilot force Fp step responses (High damp case) 57

Fig.45 Linkage and Load cell 59

Fig.46 Position inner loop control loading structure 60

Fig.47 Actuator and linkage 60

Fig.48 Position follower trim force step responses 61

Fig.49 Position follower pilot force step responses 62

Fig.50 Velocity inner loop control loading structure 63

Fig.51 Velocity follower trim force step responses 60

Fig.52 Velocity follower pilot step responses 65

Fig.53 Model schematic 66

Fig.54 Topical force components 67

Fig.55 Hardware block diagram 67

Fig.56 Servo 68

Fig.57 All-electric flight simulator block diagram.....71

List of Equations

Equation 1 Torque motor dynamics 6
Equation 2 Valve spool dynamics 7
Equation 3 General orifice flow rate 7
Equation 4 Specific orifice flow rate 8
Equation 5 Chamber A flow rate 9
Equation 6 Chamber B flow rate 9
Equation 7 Valve restriction areas 9
Equation 8 Chamber A pressure 9
Equation 9 Chamber B pressure 9
Equation 10 Piston force 9
Equation 11 Load dynamics 10
Equation 12 Aircraft longitudinal equations 23
Equation 13 Aircraft Lateral equations 23
Equation 14 State Space vector form equation 24
Equation 15 Control vector 24
Equation 16 Longitudinal incremental aerodynamic force and moment 24
Equation 17 Lateral incremental aerodynamic force and moment 24
Equation 18 First order curve fitting 25
Equation 19 Second order curve fitting 25
Equation 20 Hinge moment function of elevator 41
Equation 21 Hinge moment and moment coefficient 41
Equation 22 Gearing ratio 42
Equation 23 Elevator surface dynamics 42
Equation 24 Simulator control dynamic model 42
Equation 25 Single mass aircraft control surface model 43

Equation 26 Analytical model of EHV 45
Equation 27 Actuator flow rate 45
Equation 28 Actuator flow rate due to continuity 45
Equation 29 Control column dynamics 46
Equation 30 Control column dynamics expression in $\ddot{x_b}$ 46
Equation 31 Control column dynamics expression in $\ddot{x_p}$ 46
Equation 32 Complaint linkage force expression 46
Equation 33 $\dot{x_p}$expression 46
Equation 34 Simulator control dynamic model with detail inputs 47
Equation 35 Load cell output 47
Equation 36 Free control state space equation for control loading system with rigid linkage 47
Equation 37 Free control state space equation for control loading system with complaint linkage 48
Equation 38 Pilot control state space equation for control loading system with rigid linkage 48
Equation 39 Pilot control state space equation for control loading system with complaint linkage 49
Equation 40 Open loop servo control current input 49
Equation 41 Open loop rigid linkage system state space equation 49
Equation 42 Open loop compliant linkage system state space equation 50

Nomenclature

M_p	Total moving mass
V_c	Cylinder initial chamber volume
A_p	Piston area
R_i	Resistance to internal leakage
R_e	Resistance to external leakage
M_v	Ratio of peaking in servo valve frequency response
ξ	Servo-valve damping ratio
ω_n	Servo-valve nature frequency
L_C	Servo-valve coil inductance
R_C	Servo-valve coil resistance
I_{sat}	Saturation for torque motor
c	Spool radial clearance
ω	Spool port width
C_d	Valve discharge coefficient
ρ	Fluid density
β	Bulk modulus
P_s	Supply pressure
P_r	Return pressure
B_L	Viscous damping coefficient
K_L	Spring stiffness
(X, Y, Z)	Components of resultant aerodynamic force acting on the airplane in body frame
(L, M, N)	Components of resultant external moment vector, about the mass center
(u, v, w)	Scalar components of $\boldsymbol{V}$ in F_b

$x_E,\ y_E, z_E$	Coordinates of airplane mass center relative to fixed axes
(ψ, θ, φ)	Euler angles, radians
(p, q, r)	Scalar components of angular velocity in F_b
δ_e ,δ_r , δ_a	Angles of elevator, rudder, and aileron
δ_t	Angle of elevator trim tab
δ_p	Propulsion control
α	Angle of attack
I_x, I_y, I_z	Moments of inertia about (x, y, z) axes
T_S	Transformation matrix from angular velocity to Euler angle rates
L_{IS}	Rotation matrix that transforms from simulator reference frame to inertial frame
a_{SI} ,S_I	Inertial components of the simulator reference-point acceleration and position
H_e	Aero hinge moment of elevator
$\frac{1}{2}\rho V^2 S_e$	Dynamic pressure Q
C_{he}	Aero hinge moment coefficient of elevator
A	Cross-sectional area of actuator piston, cm^2 (in^2)
B	Modeled damping coefficient, N-cm-sec (lb-in-sec)
c	Damping coefficient of linkage, N-sec/cm (lb-sec/in)
Ci	Valve current gain, cm^3/sec-mA (in^3 /sec-mA)
p	Pressure difference of cylinder chambers
q	Fluid flow rate, cm^3 /sec (in^3 /sec)
q_i	Component of linearized valve flow rate, cm^3/sec (in^3 /sec)
q_r	Rated valve flow rate, cm^3/sec (in^3/sec)
R_b	Lever arm of column base, cm (in)
R_a	Lever arm of pilot force, cm (in)
T	Column torque, N-cm (lb-in)
V_E	Effective volume of compressed fluid, cm 3 (in3)

x_b	Displacement of column base, cm (in)
x_p	Displacement of actuator piston, cm (in)
C_p	Valve pressure gain, cm 5 /N-sec (in5/lb-sec)
eT	Input test signal, V
Fc	Load cell force, N (lb)
Fp	Pilot input force, N (lb)
G	Modeled spring rate, N-cm/rad (Ib-in/rad)
$Gmax$	Maximum value of modeled spring rate, N-cm/rad (lb-in/rad)
i	Current, mA
ir	Rated valve current, mA
I	Modeled control inertia, N-cm-sec^2 (lb-in-sec^2)
J	Mass moment of inertia of column, N-cm-sec^2 (lb-in-sec^2)
k	Spring rate of linkage, N/cm (lb/in)
$K1$	Transducer gain, V/N (V/lb)
$K2$	Admittance of valve circuit, mA/V
$K3$	Gain of potentiometer circuit, V/cm (V/in)
l_1	Distance between link attachments on bell crank, cm (in)
l_2	Distance between piston link attachment and bell crank pivot, cm (in)

PART A: Electro-hydraulic Servo-valve

1: Background

Fluid mechanics began to develop in two different directions at the end of 19th century. One was theoretical hydrodynamics, which treats fluid as frictionless and non-viscous. Although this theory of ideal streamline fluid achieved a very high level of theoretical completeness, it was of little practical importance. For this reason, practical engineers developed their own highly empirical science of hydraulics [1].

Today, hydraulic control systems have gained their position in the industry because of the feature of high torque-to-inertia ratio and big power factor. Hydraulic actuators are characterized by their ability to impart large forces at high speeds, and are used in many industrial motion systems such as aircraft surface control systems, weapon control systems and hydraulic press machines. Hydraulic systems are mechanically "stiffer," resulting in higher machine frame resonant frequencies for a given power level, higher loop gain and improved dynamic performance. They also have the feature of being self-cooled since hydraulic fluid effectively acts as a cooling medium, carrying heat away from the actuator and flow control components.

The study of electro-hydraulic servo-valve and hydraulic control systems serves as preparation for the simulation of aircraft motion and control in Part B. The overall goal of this project was to fully understand aircraft motion and control loading simulation, which were implemented in a full flight simulator such as the one in **Fig.1**.

The first "ground based" flight simulator—Link Trainer—was built in the early 1920s by Edwin A. Link [2]. It had a pneumatic motion platform driven by bellows, which provided pitch, roll, and yaw motion cues. By 1969 hydraulic actuators had begun to provide motion cues in commercial flight simulators. Shortly, the 6 degree of freedom (DOF) motion base—hydraulic driven Steward Platform—brought simulators to their next generation. About the same time hydraulic actuators also began to replace older, passive control feeling generators, such as mechanical springs, viscous dampers or electromechanical brakes. Hydraulic control actuators used in flight simulators are low friction devices, controlled by analog or digital computers to provide simulated motion and control dynamics. **Fig.2** illustrates typical components that contribute to the control feeling sensed by the pilot.

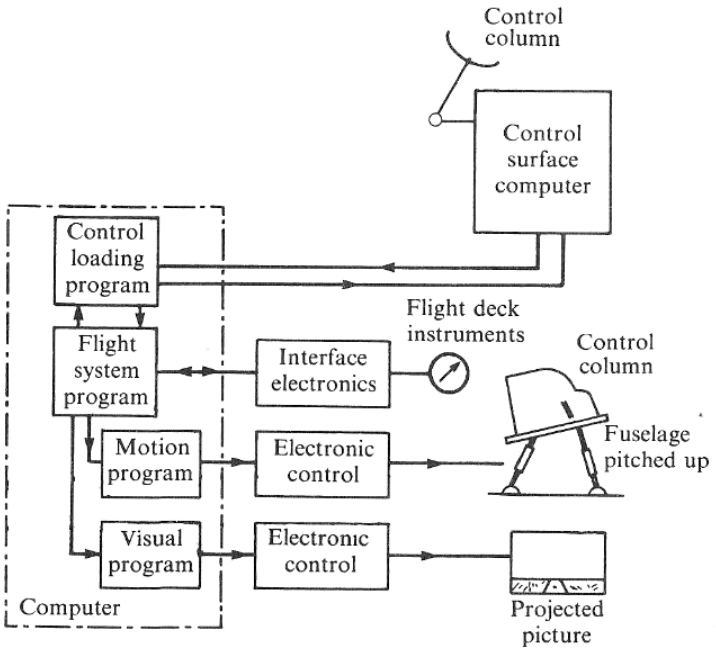

Fig.1 Block schematic of simulator interconnections [3].

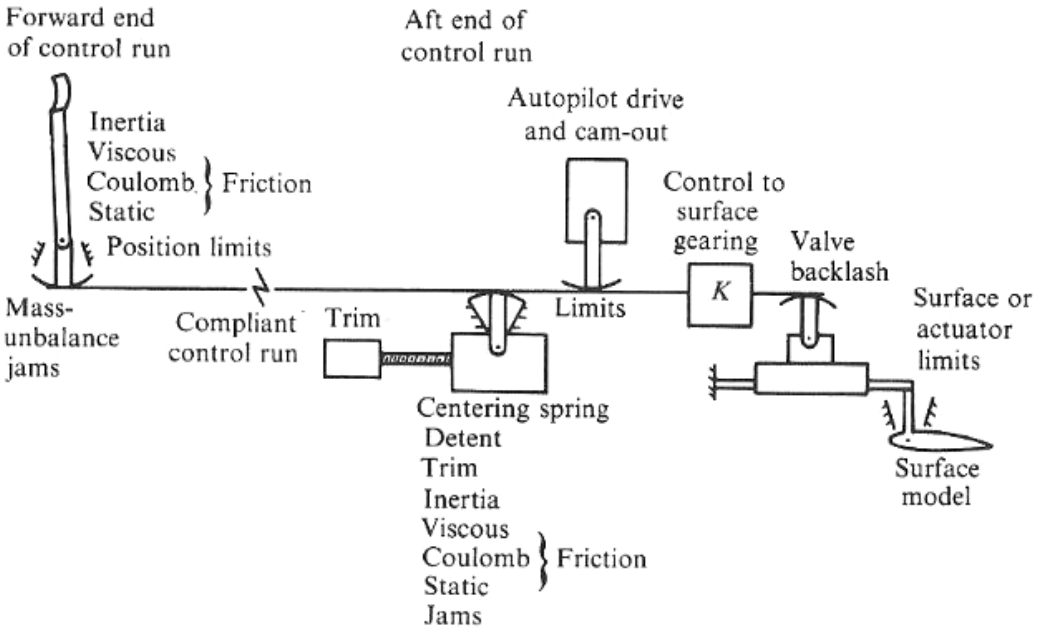

Fig.2 Potential component contributions to control loading [3].

2: Objective

In Part A, a MOOD 760 series servo valve (**Fig.3**) with a double-acting, double-rod actuator assembly (**Fig.4**) is examined, mathematically modelled, and symbolically simulated by Simulink. The particular EHV is a high performance, two-stage design with 10 gpm rated flow at 1000 psi valve pressure drop. This assembly is very similar to the ones used in flight simulator control loading systems. The resultant Simulink model was plugged into an elevator control loading channel that is also modeled by Simulink in Part B of this thesis.

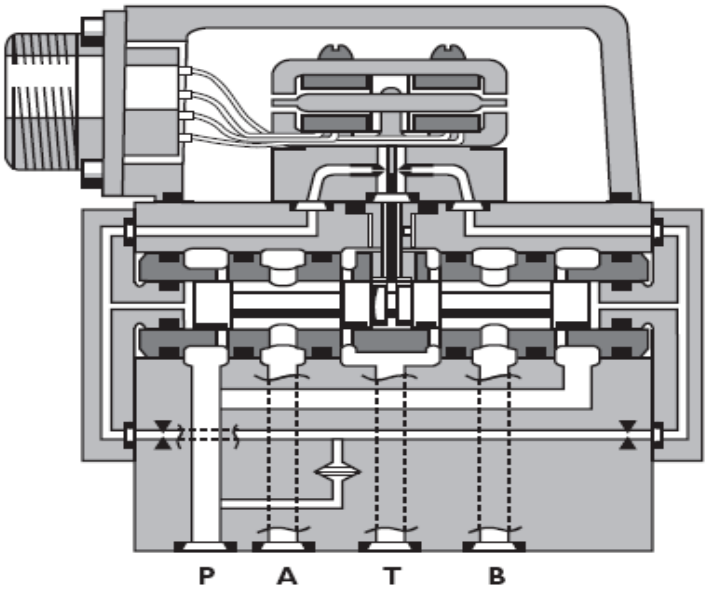

Fig.3 Cross section of nozzle-flapper type servo-valve (Illustration courtesy of Moog).

2.1 EHV

The selected EHV is a two-stage torque-motor-actuated 4-way EHV, as the one shown in **Fig.3**. With zero input current, it is symmetrical at the null position—equal left and right control pressures, equal port A and port B pressures. When an input control current is applied to the torque motor coils, it creates a magnetic force which acts on the ends of the pilot stage armature. This causes a deflection of the armature/flapper. The deflection of flapper restricts fluid flow through one nozzle, which is carried through to one spool end, resulting in different control pressures acting on the left and right spool ends. The pressure difference moves the spool. Movement of the spool opens the supply pressure port (P) to one control port while simultaneously opening the tank port (T) to the other control port. The spool will move back and stop at a position close to neutral when the resultant torque force equals the total

restoring forces due to the feedback spring and the pressure difference between port A and port B. Then the spool is held open in a state of equilibrium until the command signal changes to a new level. In summary, the spool position is proportional to the input current with constant pressure drop across the valve, and the flow to the load is proportional to the spool position [4].

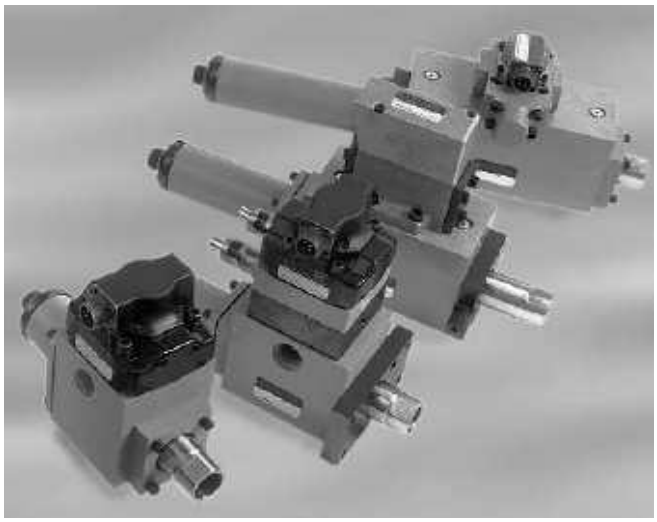

Fig.4 Linear servo-hydraulic actuator assemblies (illustration courtesy of Moog).

2.2 Linear Hydraulic Actuator

A hydraulic actuator is a device which converts hydraulic energy into mechanical force or motion. Two major actuator types are linear actuators and rotary actuators. Linear actuators are often called hydraulic cylinders, and rotary actuators are commonly called hydraulic pumps. Both hydraulic cylinders and hydraulic pumps can be found in flight simulators. The famous 6 DOF Stewart-Platform motion base utilizes 6 linear hydraulic cylinders. Linear actuators normally are used in primary control (elevator, aileron, and rudder) simulation, while both linear and rotary actuators can be used in secondary control (toe brake, nose wheel and trim wheel) simulation. In this thesis, the position control of a linear hydraulic actuator similar to the ones used in simulator primary control channels is analysed and modeled.

2.3 Hydraulic Control System

A block diagram of the position servo is indicated in **Fig.5**, and **Fig.6** illustrates its physical model. The hydraulic power supply is a separate system. For the scope of this thesis, we assume constant supply pressure Ps and zero return pressure Pt. The servo controller is usually a separate electronic circuit that implements the control law. In the following cases, the servo controller outputs electrical current. The flow control valve is EHV. The displacement transducer is a fast LVDT (Linear Variable Differential

Transformer) with a very small time constant. The dynamics of LVDT is 1 or 2 orders faster than that of the EHV and actuator, so its dynamic response can be ignored.

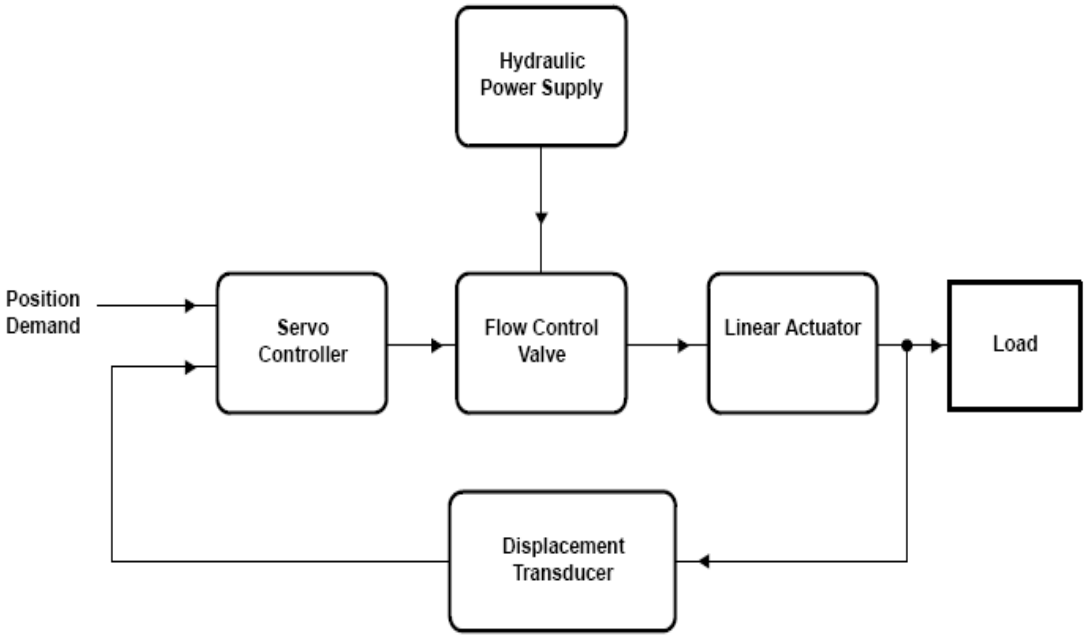

Fig.5 Block diagram of a position control hydraulic servo system.

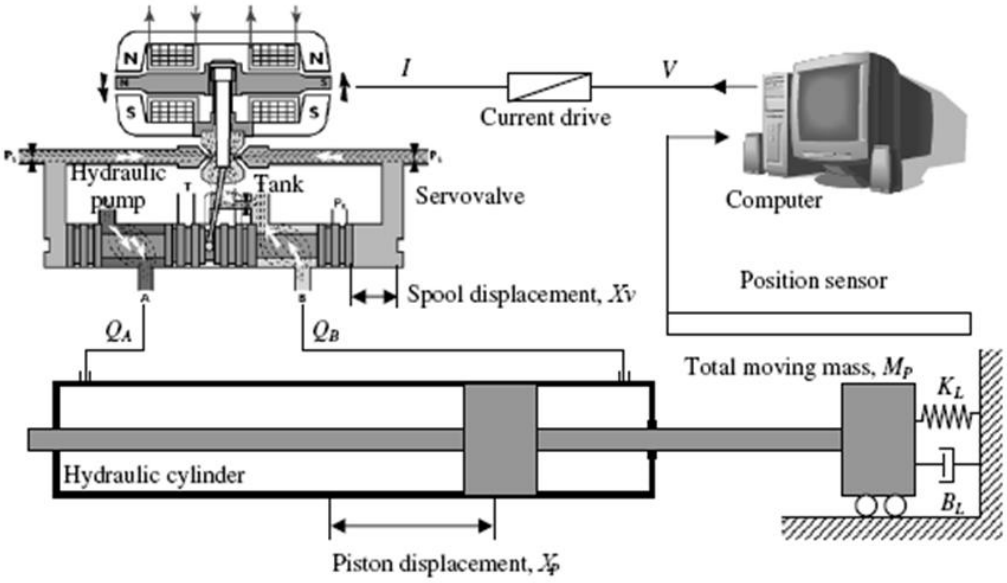

Fig.6 Physical model of electro-hydraulic servo-system [7].

3: Mathematical Modelling

Noah Manring's book—Hydraulic Control Systems [5], which is one of the most recently published text books on the subject of hydraulic control—has discussed all three typical hydraulic control systems—position control, velocity control and force control. Manring's analyses are carried out under the assumption of a slowly moving actuator piston that is connected to a working load; therefore both the servo-valve and cylinder dynamic transient contributions can be safely ignored. Under the slow moving assumption, the control plant is dominated by the dynamics of the working load. Manring has shown that position and force control can be presented by a first order system, and velocity control by a second order system. This simplification works very well when the slow moving condition is satisfied [5]. However, this is not the case in simulator applications where the slow moving condition is not always true, so the dynamics of the EHV and actuator must be taken into account, which results in a high order system and increases complexity of the system. In this section a detailed model of EHV is developed, which is suitable for motion and control loading simulation applications. The mathematical models were derived in a similar manner as reference works [6], [7] and [8].

3.1 Torque Motor

The electrical behaviour of the torque motor is normally treated as an LC circuit. Its first order differential equation is:

$$V = L_C \dot{I} + R_C I$$

Eq (1)

where L_C is valve coil inductance, R_C is coil resistance, V is control voltage, I is current. As mentioned earlier, the electrical servo is a separate circuit that outputs control current. In the following Simulink modelling, a PID controller acts as the electrical servo and outputs control electrical current.

3.2 Valve Spool

The valve spool is a complex, dedicated device which exhibits high-order non-linear characteristics. For accurate modelling, many parameters, such as muzzle and orifice sizes, spring rates, spool geometry etc., are not accessible for users. In text book [6], a detailed, accurate modelling based on manufacturing parameters was conducted, and its result are very close to a second order system. So, an alternative approach is to utilize the manufacturer's specification data sheet—the frequency response as **Fig.7**—

through which we can readily obtain the spool's natural frequency ω_n and damping ratioξ. In this case ω_n=534 rad/s, ξ=0.48.

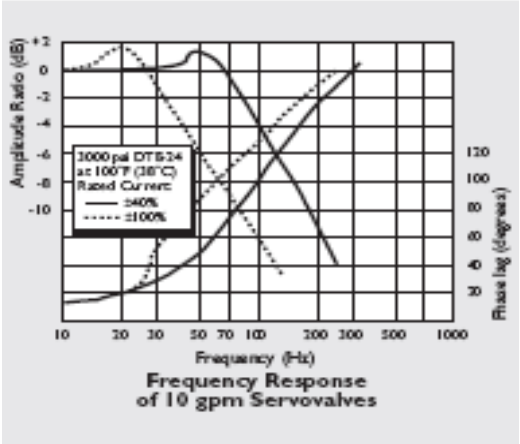

Fig.7 Servo-valve frequency response curve (illustration courtesy of Moog) [4].

The corresponding second order differential equation is:

$$\ddot{X_v} + 2\omega_n \xi \dot{X_v} + {\omega_n}^2 = I^* {\omega_n}^2$$

Eq (2)

where X_v is the servo-valve spool displacement, ω_n is the servo-valve spool natural frequency, ξ is the servo-valve spool damping ratio, $I^* = I/I_{sat}$ is the normalized input current, I is the input current, and I_{sat} is the saturation current for the torque motor.

3.3 Valve Flow-Pressure

The calculation of flow rate requires the classic orifice equation, which is developed based on the Bernoilli equation and therefore is applicable for steady, incompressible, high-Reynolds-number flow. The orifice equation is given by [10]

$$\mathrm{Q} = A_o C_d \sqrt{\frac{2}{\rho}(P_1 - P_2)}$$

Eq (3)

where A_o is the cross-sectional area of the orifice and C_d is the discharge coefficient. When the geometry is not exactly known, or when experimental results are not available, a sharp-edged orifice result of 0.62

is typically used for the discharge coefficient [10]. The significance of orifice is that it acts as the fundamental building block in hydraulic control systems, as the P-N junction does in electro control systems.

For the configuration of the spool concerned, as in **Fig.8**,

$$Q_a = A_a(X_v)C_d\sqrt{\frac{2}{\rho}(P_s - P_A)}$$

$$Q_b = A_b(X_v)C_d\sqrt{\frac{2}{\rho}(P_A - P_r)}$$

$$Q_c = A_c(X_v)C_d\sqrt{\frac{2}{\rho}(P_B - P_r)}$$

$$Q_d = A_d(X_v)C_d\sqrt{\frac{2}{\rho}(P_s - P_B)}$$

Eq (4)

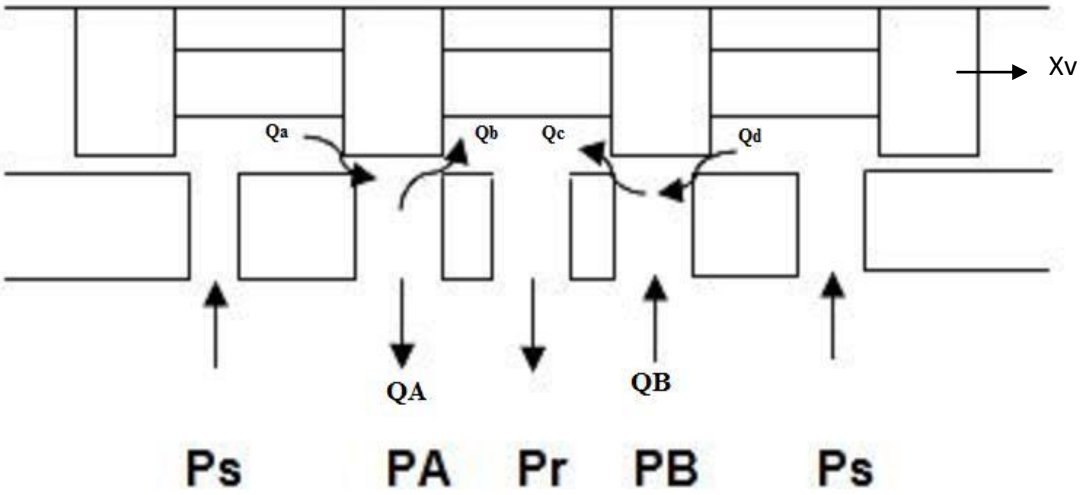

Fig.8 Servo-valve spool configuration.

Following the sign convention in **Fig.8**, it is clearly shown:

$$QA = Q_a - Q_b$$

Eq (5)

$$QB = Q_c - Q_d$$

Eq (6)

The valve restriction areas are very important control variables, and are given by

$$A_a = A_c = \omega\sqrt{X_v^2 + c^2} \quad \text{for } X_v \geq 0$$

$$A_a = A_c = \omega\, c \quad \text{for } X_v \leq 0$$

$$A_b = A_d = \omega\, c \quad \text{for } X_v \geq 0$$

$$A_b = A_d = \omega\sqrt{X_v^2 + c^2} \quad \text{for } X_v \leq 0$$

Eq (7)

where c = spool radial clearance, ω = width of ports on the valve sleeve, X_v is the spool displacement, PA and PB are hydraulic cylinder chamber pressures.

The output pressure PA and PB are calculated by applying the continuity equation to the cylinder chambers, taking into account internal and external leakage:

$$PA = \int \frac{\beta}{V_c + A_p X_p}\left(QA - A_p \dot{X}_p - QLi - QLe\right)dt$$

Eq (8)

$$PB = \int \frac{\beta}{V_c - A_p X_p}\left(-QB + A_p \dot{X}_p + QLi - QLe\right)dt$$

Eq (9)

where V_c is the cylinder chamber volume in the null condition, X_p is the piston displacement, the PA and PB initial pressure is $P_s/2$, QLi is the internal leakage, and QLe is the external leakage.

3.4 Piston Dynamics

The applied force F_p is:

$$F_p = A_p \times (PA - PB)$$

Eq (10)

where A_p is the piston area.

The piston with load dynamic equation is:

$$F_p = M_p\ddot{X}_p + B_L\dot{X}_p + K_L X_p$$

Eq (11)

where M_p is the total moving mass, B_L is the viscous damping coefficient, K_L is the load spring stiffness.

4: MATLAB Simulation

For the sake of coherence with the context, only major Simulink blocks diagrams are illustrated herein. Refer to **Appendixes A** and **B** for more detailed building block diagrams and their related MATLAB code.

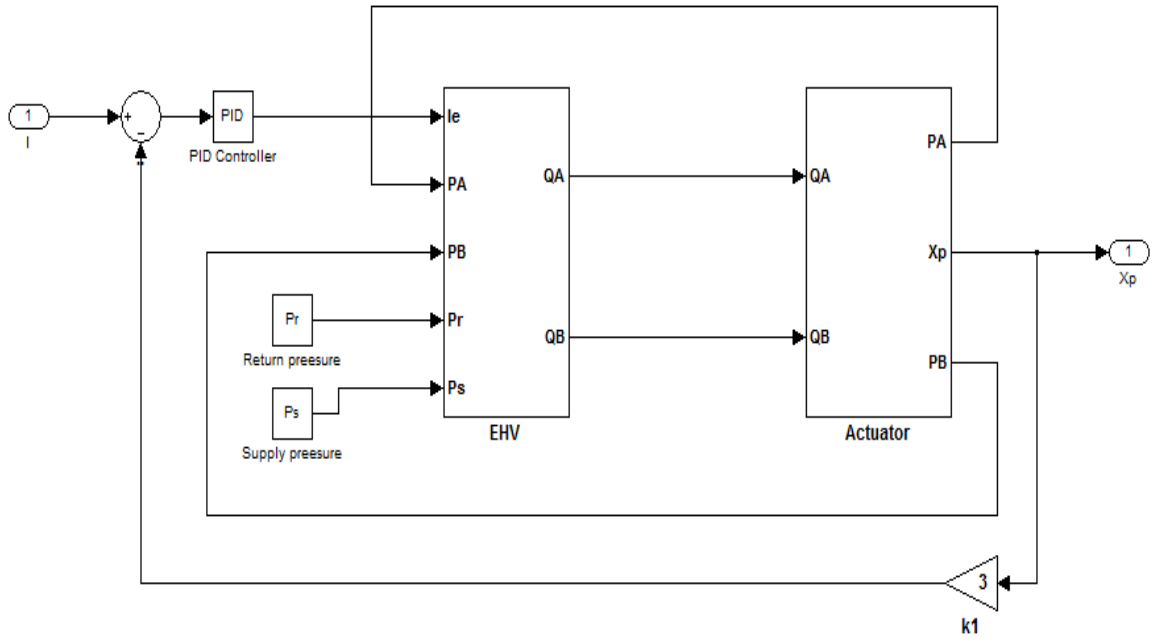

Fig.9 Top level system diagram.

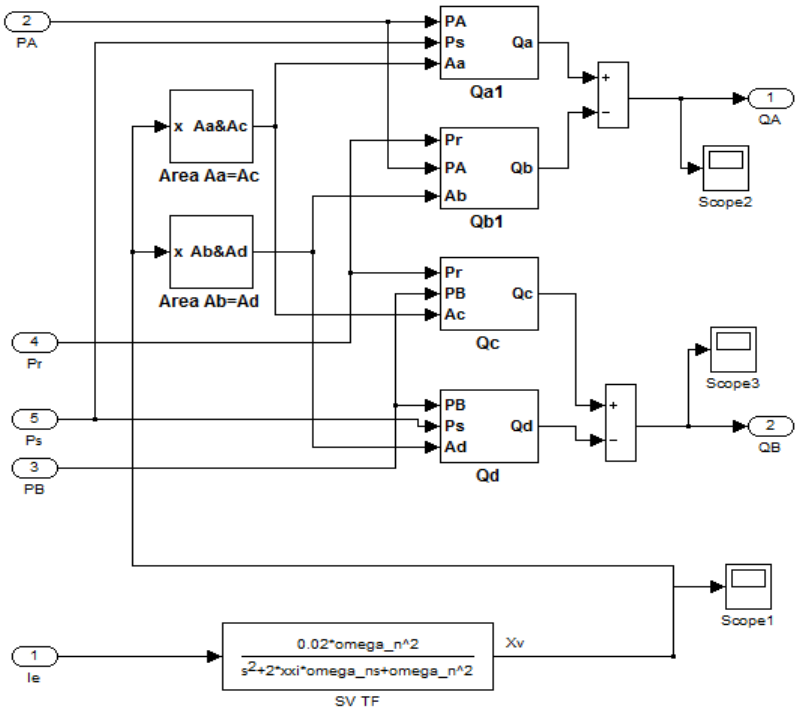

Fig.10 EHV system diagram.

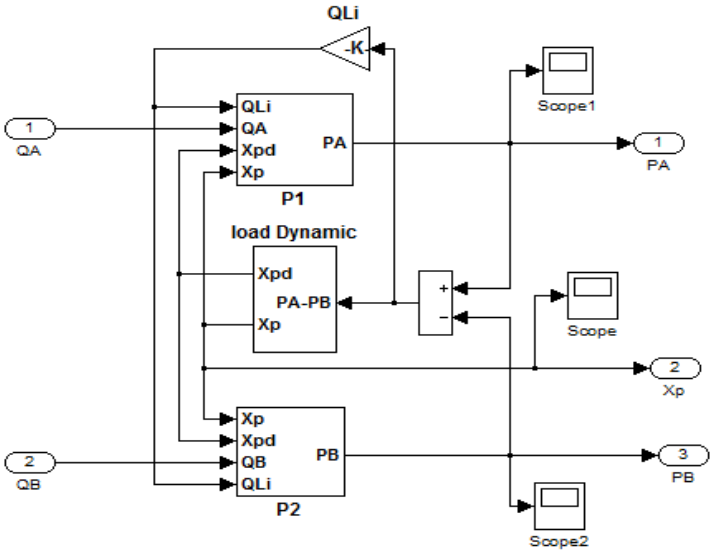

Fig.11 Actuator system diagram.

5: Parameters table

Hydraulic cylinder	M_p	Total moving mass	9 kg
	V_c	Initial chamber Volume	32.25e-6 m^3
	A_p	Piston area	645e-6 m^2
	R_i	Resistance to internal leakage	1e20 Pa s/ m^3
	R_e	Resistance to external leakage	1e20 Pa s/ m^3
Servo-valve	M_v	Ratio of peaking in servo valve	1.5 dB
	ξ	Servo-valve damping ratio	0.48
	ω_n	Servo-valve damping ratio	534 rad/s
	L_C	Coil inductance	0.59 H
	R_C	Coil resistance	100 Ω
	I_{sat}	Saturation Current	0.02 A
	c	Spool radial clearance	1e-6 m
	ω	Spool port width	0.002 m
	C_d	Discharge coefficient	0.611
System	ρ	Fluid density	867 kg/ m^3
	β	Bulk modulus	1.5e9 Pa
	P_s	Supply pressure	2e7 Pa
	P_r	Return pressure	0 Pa
	B_L	Viscous damping coefficient	2000 Ns/m
	K_L	Spring stiffness	2 N/m

6: Simulation Results and Discussion

6.1 EHV step response

Figs.12 and **13** present the dynamic responses of the spool displacement, the flow rate and the pressure of the simulated EHV responding to a step control current input. The resulting responses vividly represent the dynamic behaviour of the EHV, which is coincides with the qualitative description of EHV discussed earlier. It must be noted that a second order spool dynamics assumption was made in section 3.2, which resulted in the position feedback feature of the spool feedback spring becoming implicit. The illustrated responses refer to the EHV in a closed loop; a typical position feedback control loop.

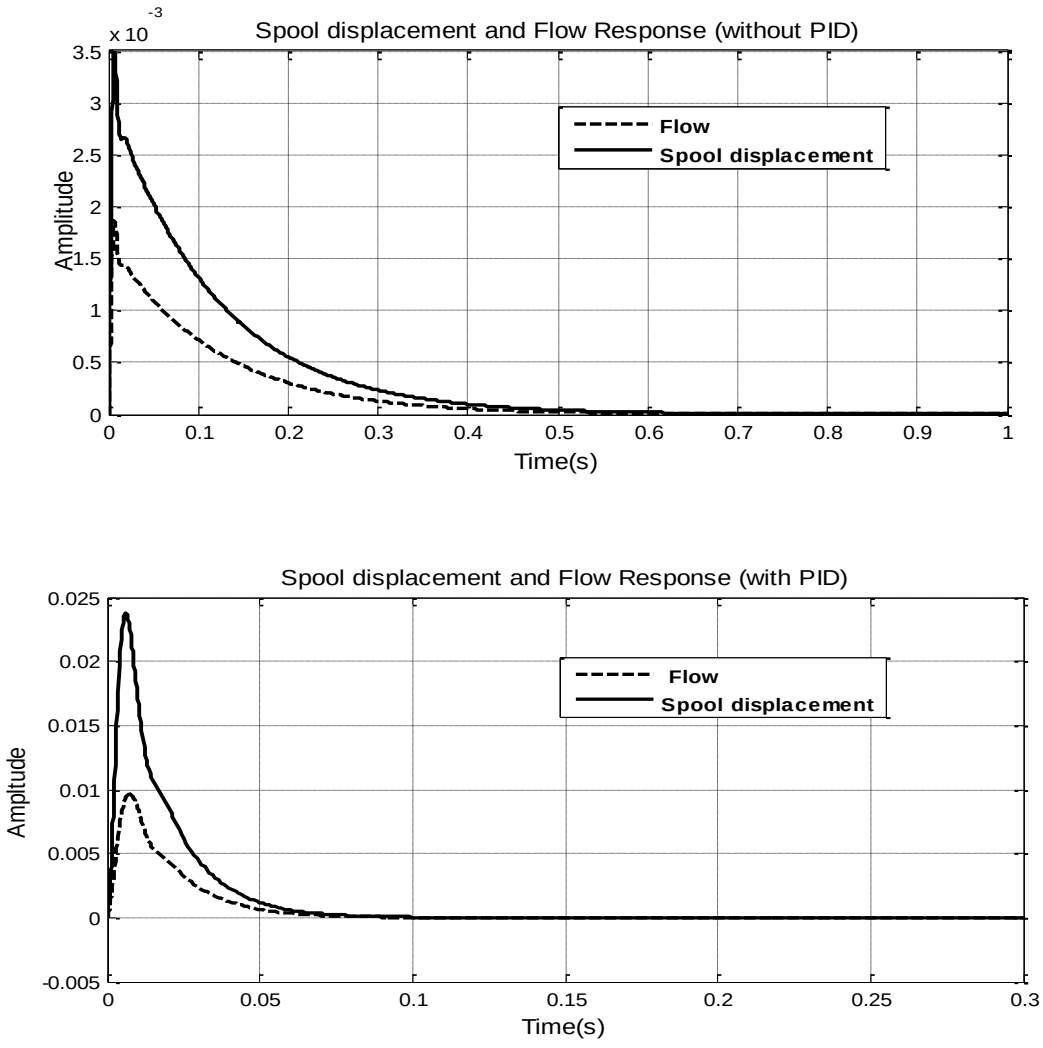

Fig.12 EHV spool displacement (m) and flow (m^3/s) step responses (initial condition: 0).

It takes about 10 milliseconds for the spool to move to its maximum offset position. Consequently, the flow (QA and QB) reach to their picks simultaneously. The resulting pressure difference (PA-PB) balances the torque (force) generated by the input current, so the spool goes back to a neutral position—a new equilibrium point, which is different than the initial null point, and the offset is determined by the amount of load.

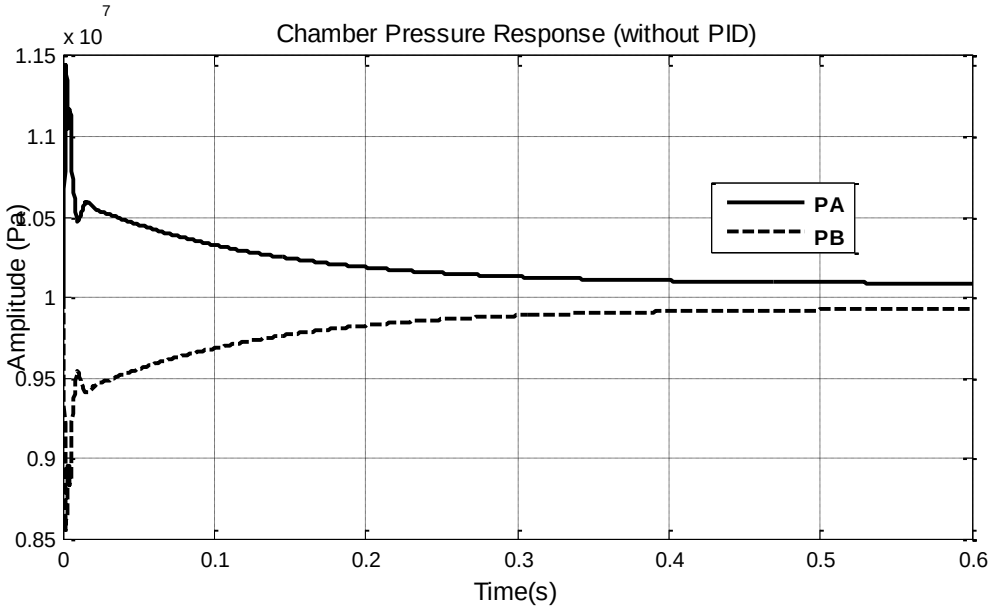

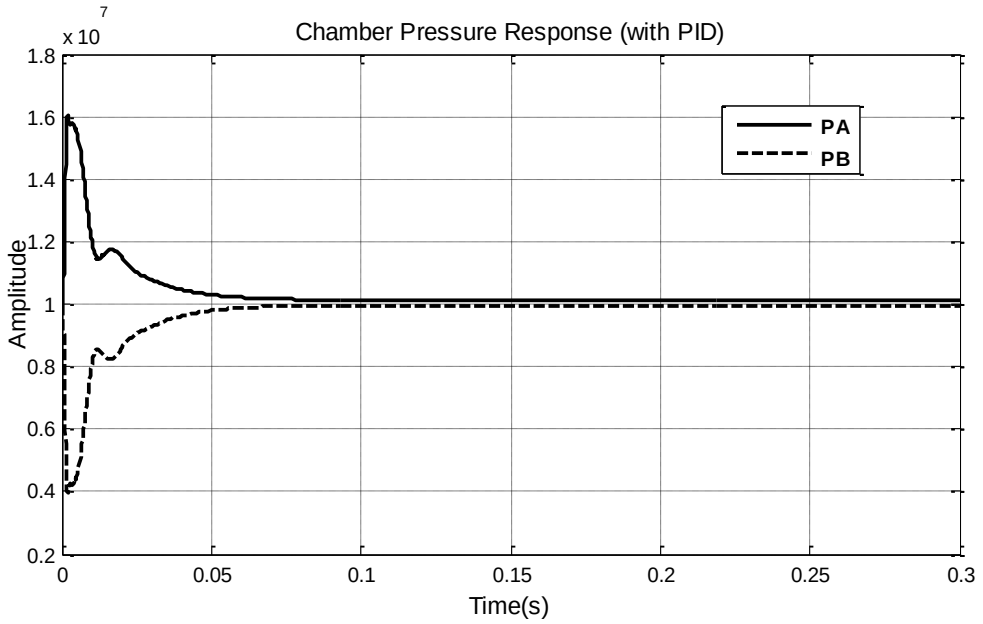

Fig.13 Cylinder chamber pressure (Pa) responses (initial pressure 1e7 Pa).

Comparing different control implementations between the simple feedback and the tuned PID controller, it can be seen that the response of the tuned PID controller is much faster than that of the unturned simple feedback control. However, a faster response requires higher mechanical capability; in this case it requires a bigger maximum allowable spool displacement and adequate availability of flow supply. This can be realized in both **Figs. 12** and **13**. In industry practice, the choosing of EHV and a control scheme is a trade-off between cost and performance.

6.2 Cylinder position response

The cylinder extend/extract position is the objective of the EHV position servo loop discussed herein. Just as in most of control systems, a step input yields important and fundamental information about the system. Tuning a controller refers to obtaining desired output dynamics by adjusting control parameters. **Fig. 14** indicates the resulting position responses between the simple feedback and the tuned PID controller.

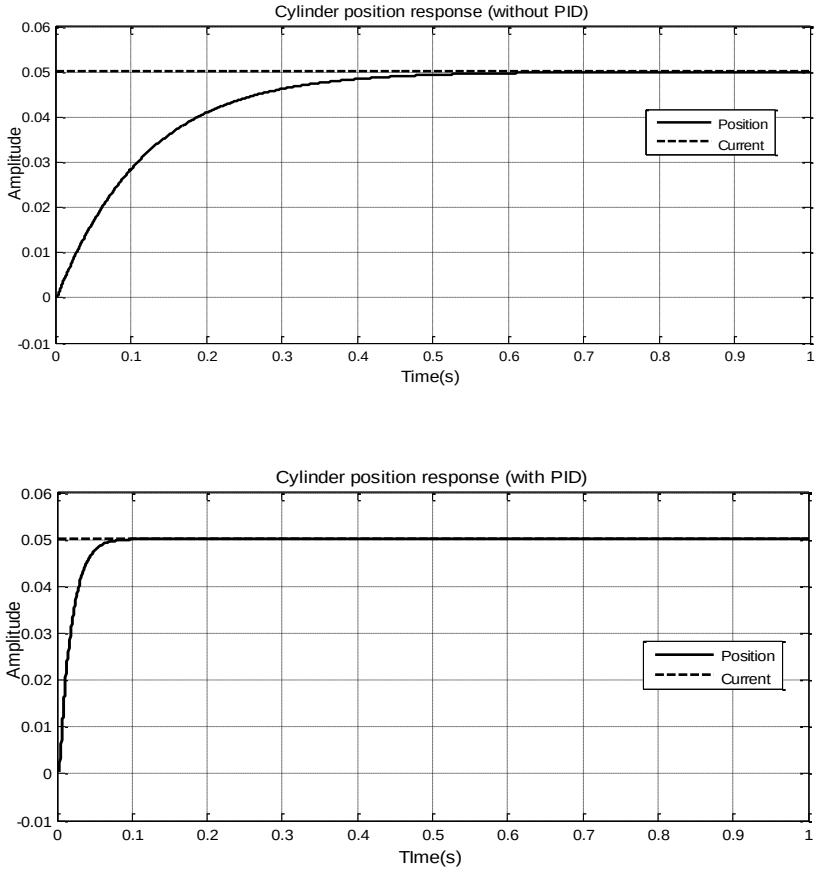

Fig.14 Cylinder position (m) step response (control electrical current (mA) step input).

The response of the simple feedback has longer T_r and T_s , obviously not the desired response. The tuned PID controller has a satisfactory response. The PDI gain terms can be tuned according to the Ziegler-Nichols rule. In the turning process, it was noticed that an adequate response could be obtained by tuning the proportional gain alone. The simple feedback controller can obtain a good shape of the position response curve by increasing the feedback gain alone. However, getting the desired output response is not the only design objective. For example, increasing feedback gain will reduce the general gain of the system for a given input current, and so the electric control current must be increased to get the required position output, which means reducing the stability margin and usable working range of the EHV. As in any product design, the controller design is an iterative process to optimize the balance between performance, cost, system robustness and maintainability. In the case of motion and control loading controller design, the ease of tuning the controller should also be taken into account.

6.3 Sinusoidal and pulse response

Simulator control loading systems can be programmed to emulate springiness, damping, end stop, backlash and dead bands. For example, the simulated mechanical end stop feels as if the control column is in contact with a mechanical end stop. This realistic and nuanced feeling comes from the EHV's excellent high frequency performance characteristic.

Figs. 15 and **16** show the resulting pulse and sinusoidal signal responses. The relationship between sinusoidal and step responses can be clearly seen: a better step response results in better pulse and sinusoidal responses. However, phase delay occurs in both cases. For the case of un-tuned control, the phase delay is more significant. A small amount of phase delay can also be found in the response of the tuned controller; this is because the zero derivative gain term was chosen in order to alleviate disturbance noise coming from signal. In practice, specific applications need to select appropriate position transducers. For example, for an accurate and precise position control that does not require fast responses, a contacting type of LVDT is most appropriate. But when a fast transient response is desired, not only the position but also its derivatives (velocity and acceleration) need to be fed back. In this case, a non-contacting position sensor (NPS) is a better choice because it has a higher signal to noise ratio. In flight motion and control simulation applications, a type of non-contacting linear position transducers is used which utilizes magnets to generate magnetic fields that very as a function of cylinder position to detect varying magnetic fields to measure the position of cylinder.

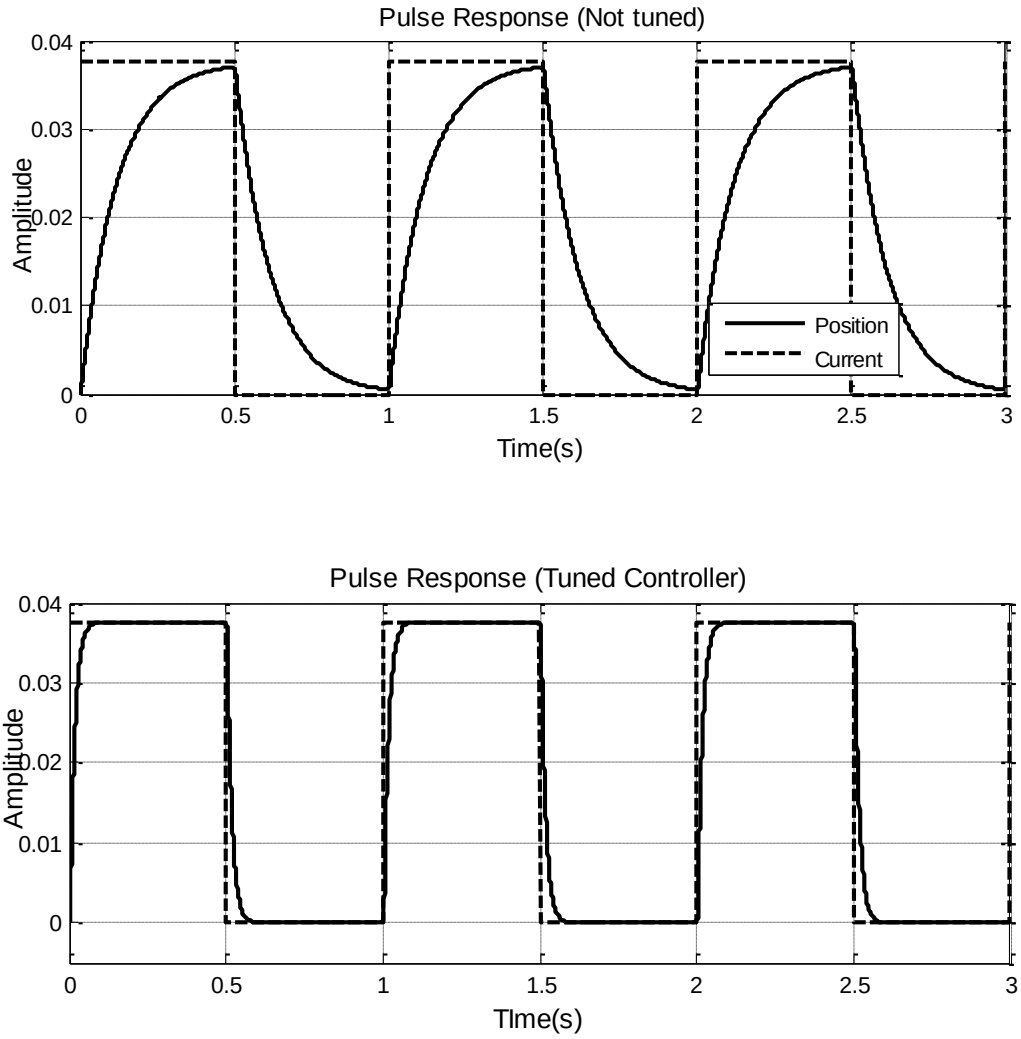

Fig.15 Pulse responses.

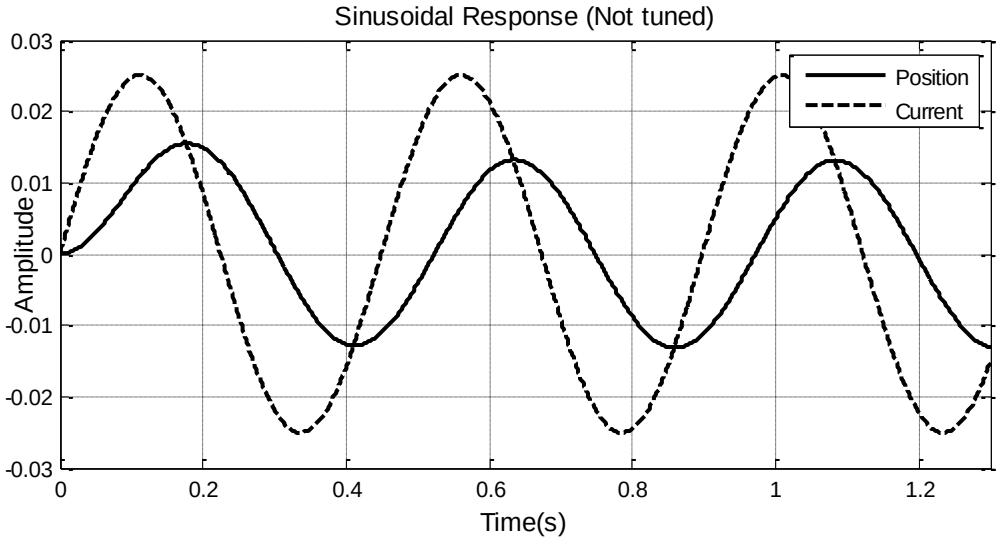

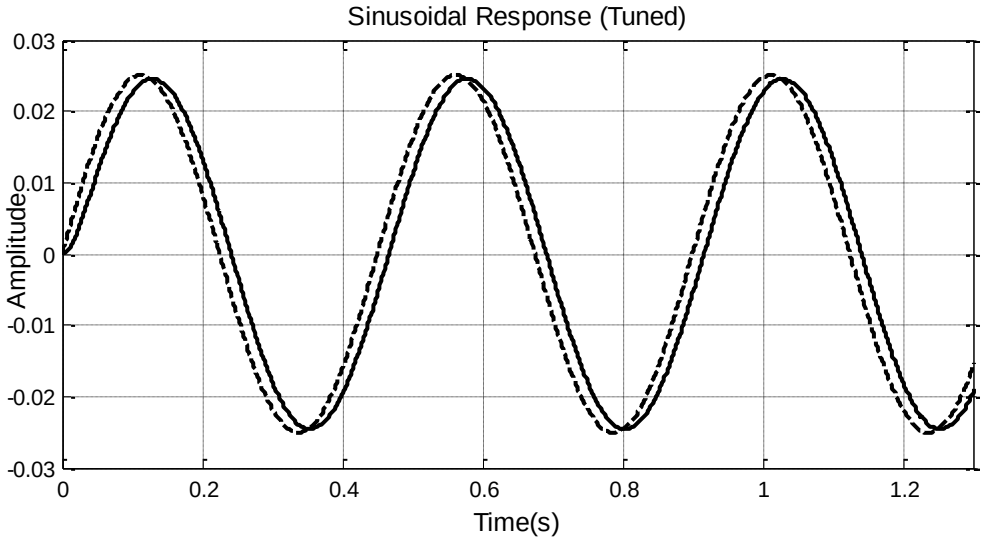

Fig.16 Sinusoidal responses.

7: Summary of Part A

An EHV Simulink model has been established based on the mechanical parameters of the EHV. This model can serve as a platform to investigate the dynamics of EHVs, which will be used for the flight simulators under study in Part B. It is noted that the presented model can be further refined in future research, for example, by taking into account for friction. Although a hydraulic linear cylinder is known as a low friction device; friction could considerably influences the high-end performance. Also as described in section 3.2, the EHV spool dynamics was derived approximately from the resulting characteristic response curves of the selected EHV. Obtaining of the actual manufacturing data of the EHV will improve the fidelity of the EHV simulation.

A position servo control has been constructed using the resultant EHV Simulink model and the linear hydraulic double-ended cylinder Simulink model. The construction of the position servo and its control parameter tuning process revealed that the choosing of an EHV that has certain specifications to match a particular control scheme is a trade-off between the cost of EHV and the servo control performance required. The design is always an iterative and optimizing process.

We now move on to Part B, in which we consider aircraft motion and control loading simulation, a practical application of electro-hydraulic servo-valve and hydraulic control servo.

Part B Simulator Motion and Control loading

8: Introduction

Part B of this thesis is about motion and control loading systems of flight simulators. Simulators have utilized electro-hydraulic servo-valves as a means of actuation of motion and control loading simulation for more than half a century. The use of EHV in simulators is an important application of EHV.

The design and development of modern aircraft makes extensive use of flight simulation. There are three major categories of simulators [3]: in-flight simulators, ground-based researching simulators and pilot training simulators. This thesis is concerned with only the third one–pilot training simulators. There is a vast range of problems open to investigation on simulators, but the essential feature of all such investigations is to introduce the pilot into a closed loop control situation. One of the most important simulation objectives is to simulate the static and dynamic behaviour of aircraft in real flight situations. It should be noted that it is impossible and not feasible to simulate the complete range of the flight dynamic profile of real aircraft. Hence we focus on certain segments of the static and dynamic profile that are needed for pilots' training. Currently, the simulation industry is able to provide pilots with simulators that can comply with all regulatory specified requirements. The scope of Part B is to examine simulator motion and control loading systems, and the goal is to fully understand the simulation of aircraft motion and control loading.

In the following sections, motion and control loading simulation will be examined in detail. First, real aircraft motion and control are introduced, followed by simulation algorithms and mathematical models. An elevator control loading channel is represented in state space and also symbolically modelled using the EHV model devolved in Part A. The focus is on control scheme implementations. Regulatory tests and evaluation are reviewed as the final objective of the simulation. Also, industry examples of digital hydraulic motion and control loading, and the latest electric motion and control loading systems are introduced.

9: Motion simulation

9.1 Aircraft motion equation

The basis for analysis, computation, or simulation of the unsteady motion of a flight vehicle is the mathematical model of the vehicle and its subsystems. Due to the complexity of airplane dynamics, the best starting point is to treat a rigid-body airplane, at a steady flight equilibrium point—steady state reference flight condition (v_0 =p_0=q_0=r_0=ϕ_0=0), selecting stability axes (w_0=0). Following the derivation as Etkin [12] (refer to **Fig.21**), and under the flowing assumptions [12]:

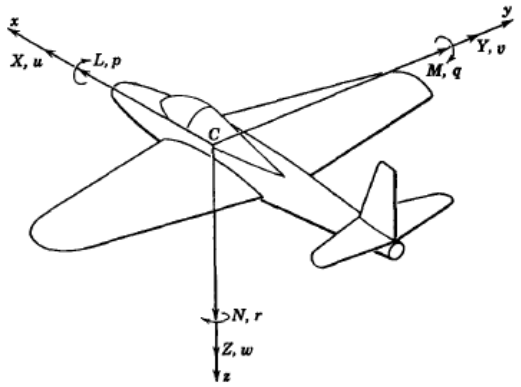

Fig.17 Notation for body axes [12].

1. The existence of a plane of symmetry.
2. The effects of spinning rotors are negligible. (The assumption has a two-fold implication, one is to drop the rotor's angular momentum contribution, and the other is to neglect rotor gyroscopic effects.)
3. The wind velocity is zero, so that $V^E = V$.
4. Neglect all the derivatives of the symmetric forces and moments with respect to asymmetric variables.
5. Neglect all derivatives with respect to rates of change of motion variables expect for $Z_{\dot{w}}$ and $M_{\dot{w}}$.
6. The derivative X_q is also negligibly small.
7. The density of the atmosphere is assumed not to vary with altitude.

The linear equations of airplane motion under small perturbations are expressed in the following longitudinal and lateral sets:

Longitudinal Equations [10]

$$\begin{bmatrix} \Delta\dot{u} \\ \dot{w} \\ \dot{q} \\ \Delta\dot{\theta} \end{bmatrix} = \begin{bmatrix} \frac{X_u}{m} & \frac{X_w}{m} & 0 & -g\cos\theta_o \\ \frac{Z_u}{m - Z_{\dot{w}}} & \frac{Z_w}{m - Z_{\dot{w}}} & \frac{Z_q + mu_o}{m - Z_{\dot{w}}} & \frac{-mg\sin\theta_o}{m - Z_{\dot{w}}} \\ \frac{1}{I_y}\left[M_u + \frac{M_{\dot{w}} Z_u}{(m - Z_{\dot{w}})}\right] & \frac{1}{I_y}\left[M_w + \frac{M_{\dot{w}} Z_w}{(m - Z_{\dot{w}})}\right] & \frac{1}{I_y}\left[M_q + \frac{M_{\dot{w}}(Z_q + mu_o)}{(m - Z_{\dot{w}})}\right] & -\frac{M_{\dot{w}} mg\sin\theta_o}{I_y(m - Z_{\dot{w}})} \\ 0 & 0 & 1 & 0 \end{bmatrix} \begin{bmatrix} \Delta u \\ w \\ q \\ \Delta\theta \end{bmatrix} + \begin{bmatrix} \frac{\Delta X_c}{m} \\ \frac{\Delta Z_c}{m - Z_{\dot{w}}} \\ \frac{\Delta M_c}{I_y} + \frac{M_{\dot{w}}}{I_y}\frac{\Delta Z_c}{(m - Z_{\dot{w}})} \\ 0 \end{bmatrix}$$

$$\Delta\dot{x_E} = \Delta u\cos\theta_o + w\sin\theta_o - u_o\Delta\theta\sin\theta_o$$

$$\Delta\dot{z_E} = -\Delta u\sin\theta_o + w\cos\theta_o - u_o\Delta\theta\cos\theta_o$$

Eq (12)

Lateral Equations [10]

$$\begin{bmatrix} \dot{v} \\ \dot{p} \\ \dot{r} \\ \dot{\varphi} \end{bmatrix} = \begin{bmatrix} \frac{Y_v}{m} & \frac{Y_p}{m} & \left(\frac{Y_r}{m} - u_o\right) & g\cos\theta_o \\ \left(\frac{L_v}{I'_x} + I'_{zx}N_v\right) & \left(\frac{L_p}{I'_x} + I'_{zx}N_p\right) & \left(\frac{L_r}{I'_x} + I'_{zx}N_r\right) & 0 \\ \left(I'_{zx}L_v + \frac{N_v}{I'_z}\right) & \left(I'_{zx}L_p + \frac{N_p}{I'_z}\right) & \left(I'_{zx}L_r + \frac{N_r}{I'_z}\right) & 0 \\ 0 & 1 & \tan\theta_o & 0 \end{bmatrix} \begin{bmatrix} v \\ p \\ r \\ \varphi \end{bmatrix} + \begin{bmatrix} \frac{\Delta Y_c}{m} \\ \frac{\Delta L_c}{I'_x} + I'_{zx}N_c \\ I'_{zx}\Delta L_c + \frac{\Delta N_c}{I'_z} \\ 0 \end{bmatrix}$$

$$\dot{\varphi} = r\sec\theta_o$$

$$\Delta\dot{y_E} = u_o\varphi\cos\theta_o + v$$

$$I'_x = (I_x I_z + I_{zx}^2)/I_z$$

$$I'_z = (I_x I_z + I_{zx}^2)/I_x$$

$$I'_{zx} = I_{zx}/(I_x I_z - I_{xz}^2)$$

Eq (13)

9.2 Control derivatives

Equations (12, 13) are both in the desired first order form, commonly referred as to as the state vector form:

$$\mathbf{x} = \mathbf{A}\dot{\mathbf{x}} + \mathbf{Bc}$$

Eq (14)

Here $\mathbf{x} = [\boldsymbol{\Delta} u \;\; w \;\; q \;\; \Delta\theta]^T$ for longitudinal, $\mathbf{x} = [v \;\; p \;\; r \;\; \phi]^T$ for lateral, **A** is the system matrix, **B** is the control matrix, and **c** is control vector,

$$\mathbf{c} = [\delta_a \;\; \delta_e \;\; \delta_r \; \delta_p]^T$$

Eq (15)

These equations of motion clearly show that the matrix **A** is made up of airplane parameters and aerodynamic derivatives. To understand the control matrix **B**, the incremental aerodynamic forces and moments that result from the actuation of the control vector are given by a set of control derivatives for longitudinal and lateral modes:

$$\begin{bmatrix} \Delta \mathrm{X_c} \\ \Delta \mathrm{Z_c} \\ \Delta M_c \end{bmatrix} = \begin{bmatrix} X_{\delta_e} & X_{\delta_p} \\ Z_{\delta_e} & Z_{\delta_p} \\ M_{\delta_e} & M_{\delta_p} \end{bmatrix} \begin{bmatrix} \Delta\delta_e \\ \Delta\delta_p \end{bmatrix}$$

Eq (16)

$$\begin{bmatrix} \Delta Y_c \\ \Delta L_c \\ \Delta N_c \end{bmatrix} = \begin{bmatrix} Y_{\delta_r} & 0 \\ L_{\delta_r} & L_{\delta_a} \\ N_{\delta_r} & N_{\delta_a} \end{bmatrix} \begin{bmatrix} \Delta\delta_r \\ \Delta\delta_a \end{bmatrix}$$

Eq (17)

With accurate aircraft perimeters and stability and control derivatives, simulators can be designed to reproduce simulated airplane flight static and dynamic behaviours. Normally, aircraft manufacturers or flight test agencies provide airplane data packages. The accuracy of the data package directly affects the fidelity of flight dynamics simulation. A major fraction of the aerodynamic research up to this point has been devoted to the determination, by theoretical and experimental means, of the aerodynamic derivatives needed for application to flight mechanics.

Simulators can be made before and/or after airplanes have been manufactured. Practically, at an airplane's detailed design stage, the simulated airplane simulator can be a test tool for airframe and control system design, providing a means to evaluate alternative design strategies [3]; this application of simulator in turn demands more thorough and accurate aircraft simulation of the simulator.

Strictly speaking, aerodynamic forces and moments are functions of state variables. Forces and moments may need to be expressed as functions of one or more of the following: [3]

- Angle of attack
- Control deflections
- Speed/Mach number
- Rotation rate
- Height
- Centre gravity position
- Ground proximity
- Geometry (e.g., flap setting, wing sweep, leading gear)

Consequently, the aerodynamic and control derivatives are not constants, and not even linear functions of those factors. For dealing with nonlinearity, curve fitting techniques such as polynomial curve fitting and table look-up techniques are used.

$$C_L = a_0 + a_1 \alpha$$

Eq (18)

$$C_m = a_0 + a_1 \alpha + a_2 \alpha^2$$

Eq (19)

The choosing of 1st order or second2nd order depends on the nature of the derivative. For example, the pitching moment coefficient C_m as a function of angle of attack α, the derivative C_{m_a} plays a major role on an airplane's longitudinal stability. So, the second order polynomial Eq (19) brings more fidelity in this case.

In cases where C_L and C_m, are functions of the angle of attack, they are also functions of flap angle and Mach number, so that a_0 , a_1 , a_2 are expressed as $f(\delta)$, where δ may be flap angle or Mach number. Normally the data of C_L and C_m at specific flap angles are given, for instance. For flap angles between the defined values, a technique is required to interpolate the appropriate valves of the dependent

coefficients a_0 , a_1 and a_2 . This often refers to 'table look-up.' Table look-up basically refers to linear interpolation between adjacent coordinate pairs. A significant amount of aero data look-up tables are used in simulation software models, and especially in aerodynamic flight modules. In some special cases, high order interpolation techniques, such as cubic spines, are used to maintain continuity of the data slope [3].

9.3 History of simulator motion

For ground-based pilot training simulators, in addition to replicating the functionality of instrumentation and navigation aids at the pilots' point of view, all the cues that pilots perceive in a real aircraft, such as visual, sound, control feeling and motion sense, are simulated with considerable fidelity. Of these, motion cue simulation is the most difficult because of the physical restrictions of the simulator's ground-based structure.

Since the inception of ground-based training simulators, motion cue simulation has intuitively been treated as an important ingredient of flight simulation. **Fig.18** shows the first generation of motion cue simulation using "man power." Note that the wheels are used by the pilot for control and the two men pitch and roll the device in accordance with the pilot's use of the wheels.

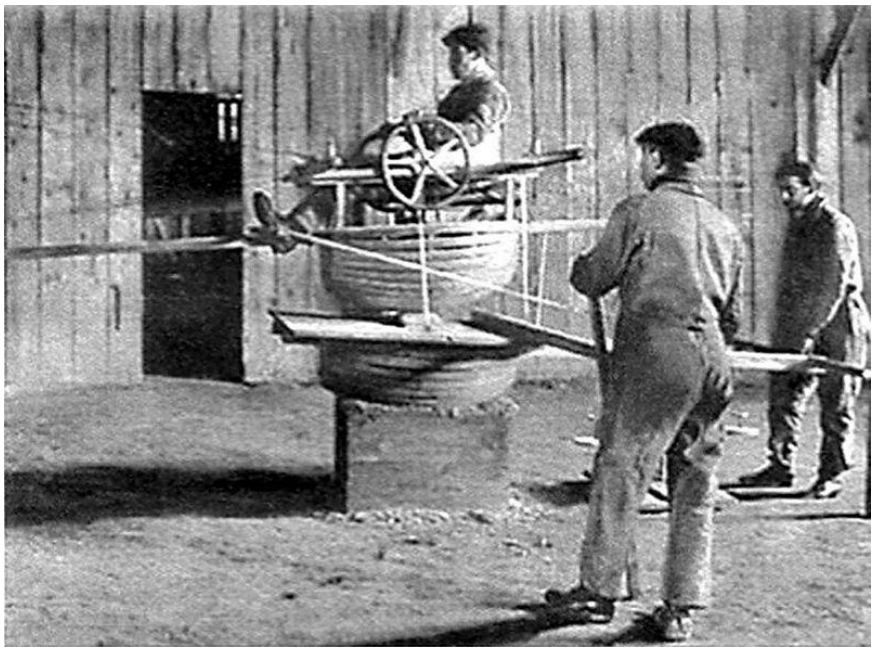

Fig.18 1909 training rig for the Antoinette aircraft with pilot seated in a half-barrel [13].

The best-known early flight simulation device is the Link Trainer **Fig.19**, which Edwin Link developed from 1927–1929. The first generation of the Link Trainer had a pneumatic motion platform driven by inflatable bellows which provided pitch and roll cues. An electric motor rotated the platform, providing yaw cues. However the "motion cue" produced by Link Trainers made no reference to their instruments, so they did not represent the interactions present in a real airplane. Also, because of the direct link between control and motion actuation, no couple cross effect was represented. Strictly speaking, this form of motion simulation is not actual flight motion simulation [2], [3].

Fig.19 Link Trainer [13].

The first simulator design documented that followed the systematic approach outline is that of Roeder (Roeder 1929) **Fig.20**. Roeder's patent describes in detail a simulator for the height control system of an airship. The computer is part hydraulic and part mechanical, with cams for generating non-linear functions [3]. However, Roeder also gives his opinion that a movable cabin would not be as useful for an airplane simulator as it would be for an airship or submarine simulator because of the complexity of airplane motion. The next generation of the Link trainer came about in the mid of 1930s, in which pilot control inputs change instrument readings and move the cabin in roll and pitch with a limited range.

Further refinements in the simulated motion cues awaited the development of electronic computers following World War II. Since then, intensive research about simulated vehicle characteristics has been done in rocket flight tests, aeronautical laboratories and space programmes. It was in the mid-1950s that

flight simulation began to catch up with the complexities of actual flight [15]. Such examples are the X-15 flight simulator, the NASA Langley Aeronautical Laboratory's "elevator seat," the F-100 simulator, which was used successfully to help resolve the inertial coupling problem of the previous F-100, and the centrifuge moving base flight simulator of the NASA Mercury project. Their complex motion systems were designed to be capable of producing accelerations in up to six degrees of freedom.

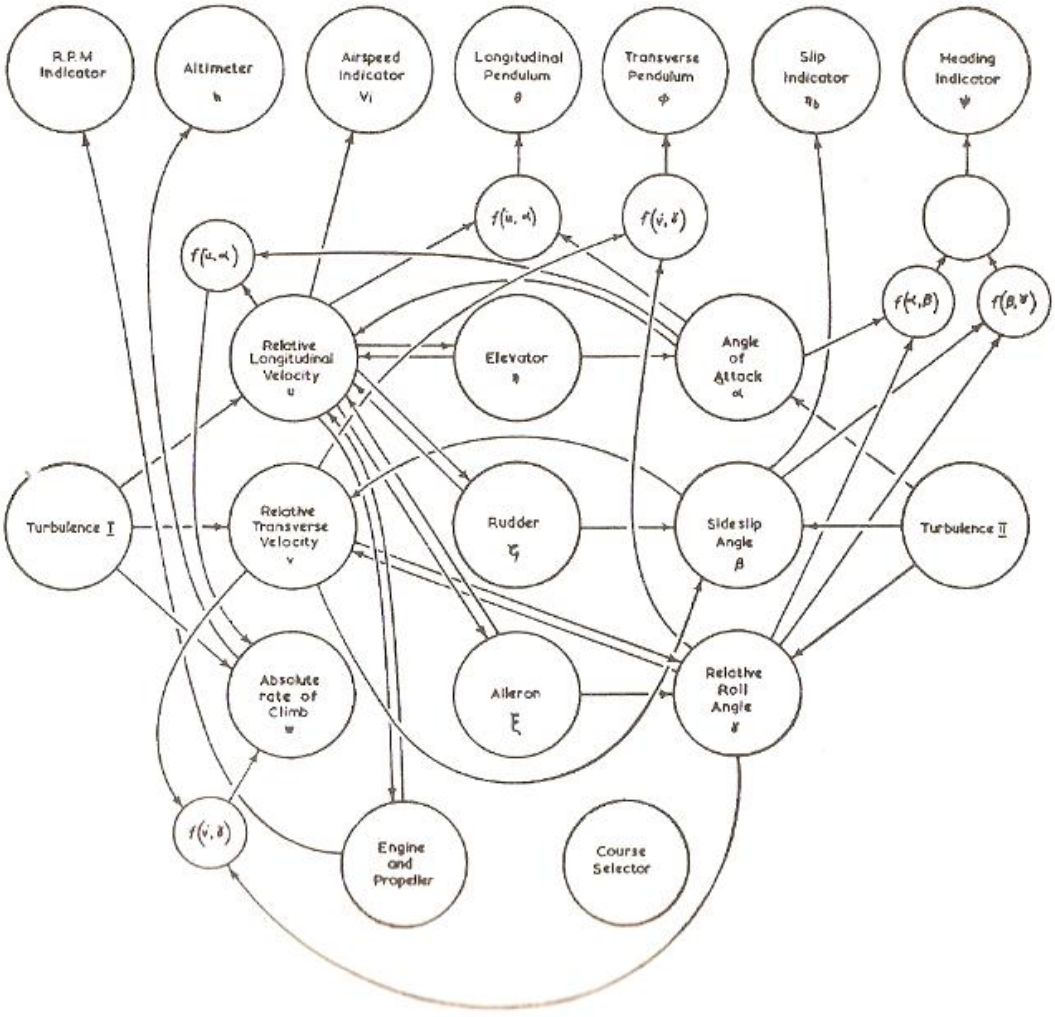

Fig.20 Roeder's aeroplane model [3].

Beginning in 1977, all aircraft simulators made for Commercial Air Transport (CAT) pilot training have had a motion base. A series of tests was conducted by the Engineering department at the University of Victoria to quantify the perceptions of airline pilots in flight simulation and the impact of motion on the simulation environment. The results show that the majority of pilots gained positive enhancement from

motion cues [16]. The strong anecdotal evidence and pilot acceptance of good motion cues in training have led some regulatory authorities to require platform motion (FAA 1980); a six DOF motion platform is a mandatory requirement for Level D flight simulators (**Fig.21**) by both FAA in the USA and EASA in Europe, while the use of motion cues for pilot training continues to be a debated and researched topic.

Fig.21 Thales flight simulator at a pitch angle (illustration courtesy of Thales) [13].

In the flight simulator industry, the motion base of simulators has evolved from 3, 4 DOF motion base to full 6 DOF motion, from analog model/control to digital model/control, and from hydraulic actuators to electrical actuators. In the following sections 9.4 and 9.5, aircraft motion simulation algorithms and a real example of motion system are presented.

9.4 Motion simulation algorithm

Systematic investigation and modelling of how the human body processes and responds to motion have resulted in methods of choosing an appropriate motion cue producing algorithm for simulators. Due to the scope of this thesis, some important results are listed without in depth investigation. Laboratory experiments [17] [18] and human vestibular model [19] show human detective acceleration thresholds are 0.1 degrees/s^2 and 0.02m/ s^2; velocity thresholds are about 2.5 degrees/s and 0.02 m/s. Static body tilt

is sensed as a change in the direction of the specific force vector, indistinguishable from a change caused by linear acceleration. Since ground-based motion platforms have a limited traveling displacement, a principle called “acceleration onset cueing” (**Fig.22**) is used. Simulators simulate the initial acceleration of the simulated aircraft with a “jerking,” and then return to the neutral position at a rate below the pilot’s sensory threshold in order to prevent the motion system from reaching its limits of travel.

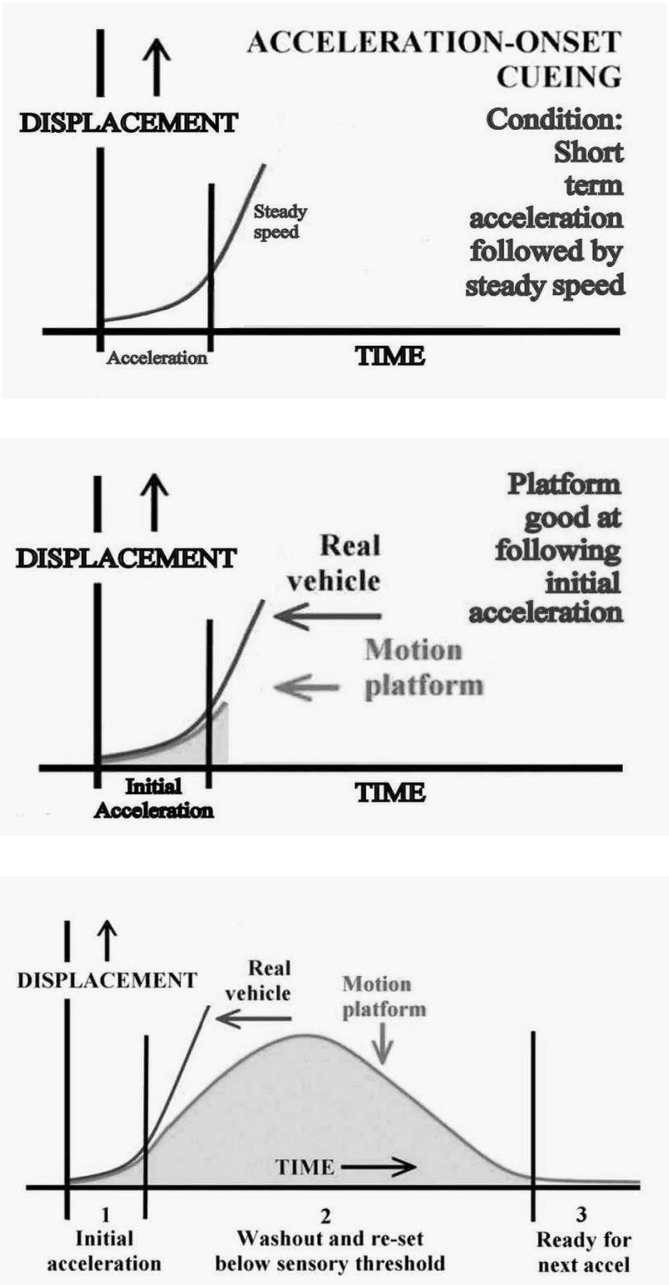

Fig.22 Acceleration onset cueing [14].

The motion platform in a level D full flight simulator uses the Stewart structure [20] shown in **Fig.23**, which is a parallel mechanical structure consisting of six independently operated hydraulic jacks, and can provide 6 DOF linear and angular motion cues. A pilot in an aircraft experiences linear motion along the three body axes of the aircraft and angular motion about these axes [16]. A synergistic motion platform provides three onset linear accelerations: heave (vertically), sway (laterally) and surge (longitudinally) and three angular components of pitch, roll and yaw. As mentioned previously, static body tilt is sensed as a change in the direction of the specific force vector, indistinguishable from a change caused by linear acceleration, and continuous acceleration is simulated by tilting the platform, again at a rate below the pilot's sensory threshold **Fig.24**.

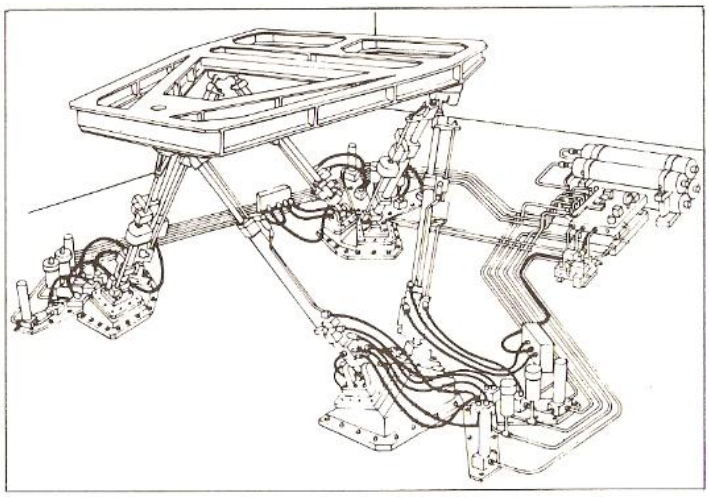

Fig.23 Six-post synergistic motion system [3].

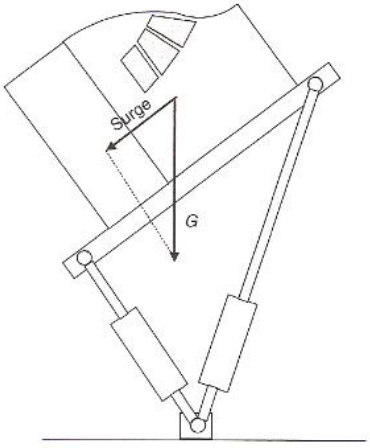

Fig.24 Tilting the platform to provide surge acceleration [9].

Several different manufacturers have designed and manufactured their own kinds of motion systems based on the Steward platform, with different cylinder diameters and lengths and different servo control implementations. The first generation was an analog control 6-DOF motion base. A digital motion system is functionally identical to the analog motion system but is realized in a digital format. The benefit of digital over analog is commonly realized as that of any other production. Improvements of the digital motion system over analog motion base are its user-friendly interface, the ease of motion cue tuning and maintainability.

Fig.25 shows a typical flight simulator installation [21] with the classical motion algorithm that is most widely used in commercial simulators [22]. The classical washout algorithm (**Fig.26**) is characterized by the empirically determined combination of linear high-pass and low-pass filters whose break frequencies and damping ratios can be adjusted off-line by trial and error—to tune the motion cue according to test pilots' subjective comments.

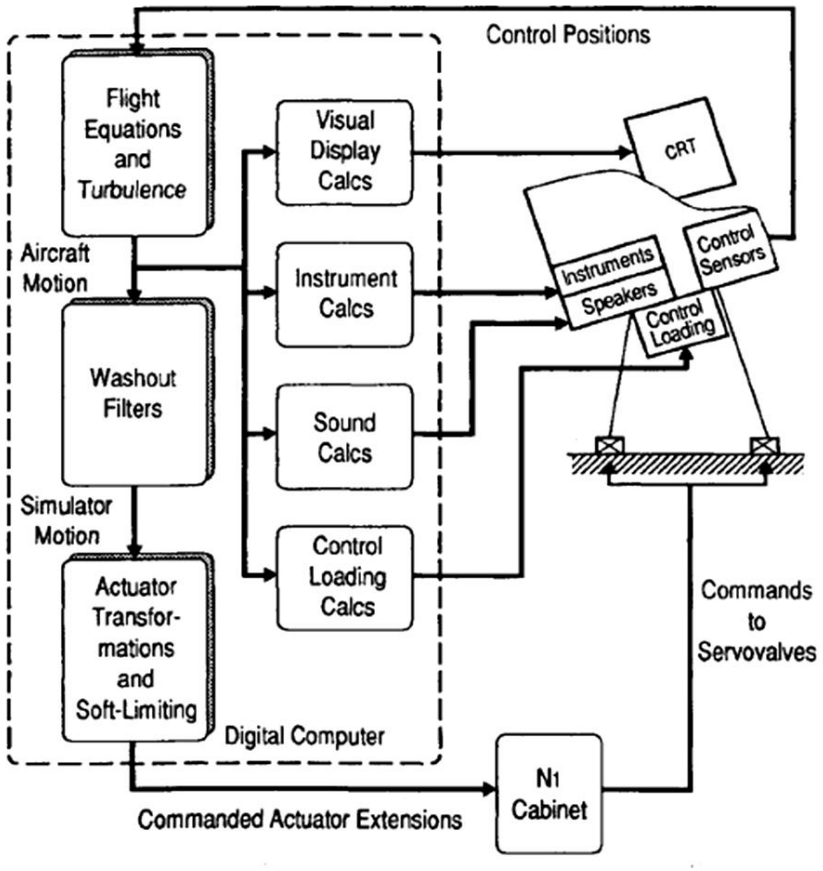

Fig.25 Typical flight simulator installation [21].

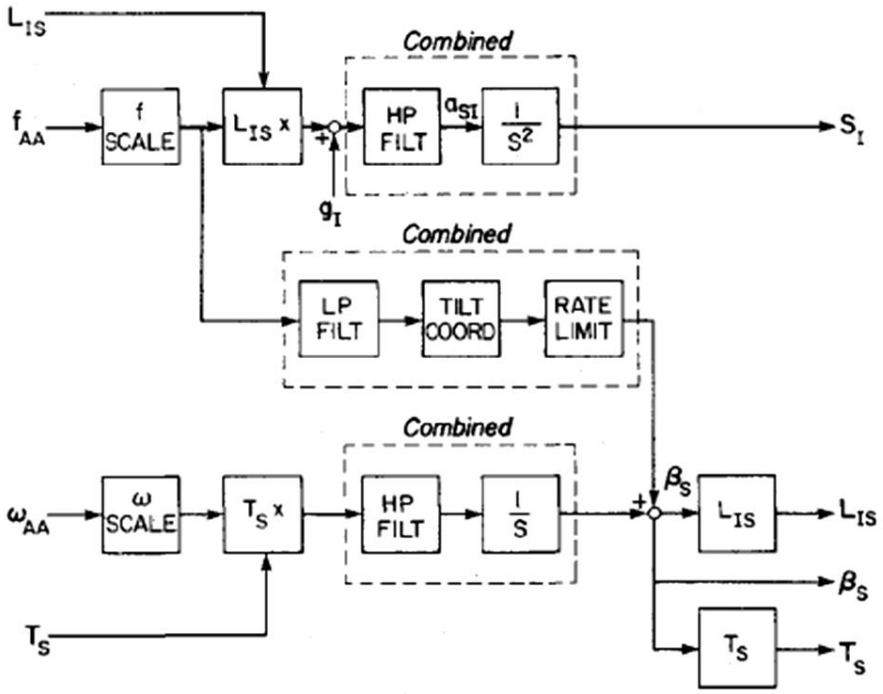

Fig.26 Classical motion algorithm [22].

In **Fig.26**, the inputs are aircraft cockpit specific forces in body axes $f_{AA} = a_{AA} - g_A$, and aircraft angular rates ω_{AA}. L_{IS} is rotation matrix that transforms from simulator reference frame to inertial frame. T_S is the transformation matrix from angular velocity to Euler angle rates. β_s is the simulator Euler angles. a_{SI} and S_I are inertial components of the simulator reference-point acceleration and position.

1) The high pass filtering yields the onset acceleration cueing and ignores the low frequency specific forces that would otherwise drive the motion cylinders to their limits. By the cross-feed channel, the low pass filtering results in low frequency forces, scaled and rate-limited to produce tilt angles resulting in sustained aircraft acceleration cues. Also, the angular high pass filtering patch yields the onset angular motion cue.
2) The cross-feed channels remain inactive during aircraft yaw and coordinated rotation motions (such as a coordinated turn).
3) Practically, since transport aircraft motions are rarely severe, 2nd order filters are usually sufficient.

Numerous schemes have been proposed for motion control in simulator, trying to enhance the classical algorithm, such as the optimal control approach [23], the robust control approach [24], the adaptive algorithm [21] and the iterative learning control algorithm [25]. However, the classical algorithm still

dominates simulator manufacturing in the industry because 1) it is mathematically and computationally simple, and hence computationally cheap, and 2) it is relatively transparent to the designer, and therefore pilots' complaints can often be easily rectified [22].

9.5 Digital simulator motion systems

A published real digital motion simulation example is cited from Hagen's "Digital control loading and motion for flight simulation" [29]. **Fig.27** indicates a simplified Motion System block diagram and its hardware diagram.

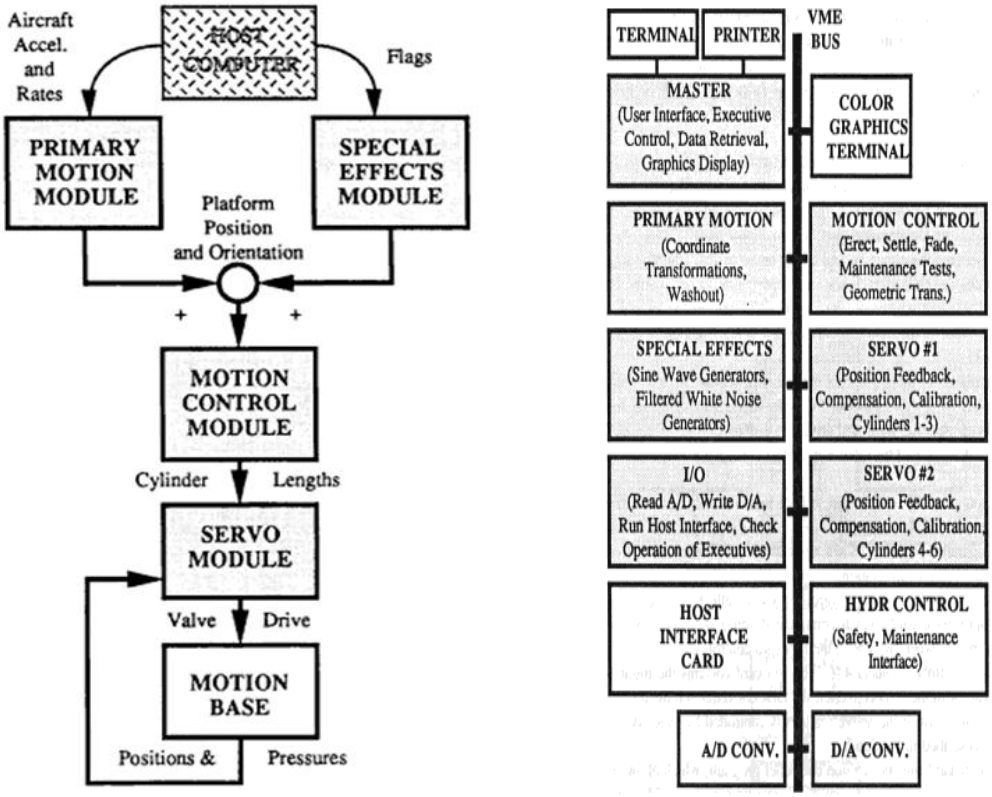

Fig.27 Simplified motion system block diagram and Hardware diagram [29].

The flight module running in the host computer passes accelerations and rates (in the aircraft body frame) to the primary motion module in the motion system. The primary motion module converts these signals into the appropriate position and orientation of the platform (at the centroid of the motion base). A special motion effects module turns individual special effects on, such as bumps, turbulence and vibrations, by sending flag signals to the special effects module in the motion system.

The hardware diagram demonstrates the computer structure of the motion system that uses a number of processors running in parallel based on the VME bus. The iteration rate reaches up to the order of KHz; control loops can be run smoothly in real time. There are six separated executives running on six cards: primary motion, special effects, motion control, servo #1, servo #2 and I/O. The master card acts as master executive of the system. It also runs the analysis and design programs—DIGITAL, which is used for designing and turning the motion system servo.

The primary motion module (**Fig.28)** implements the classical washout algorithm. The signals passed from the host go through a lower pass filter at first. This is because the flight module is running at a lower iteration rate of about the order of Hz, which is much lower than that of the primary motion; low pass filtering can eliminate system noise and the abrupt stepping caused by the different iteration rates. The centroid transformation block converts translational accelerations (at the CG of the simulated aircraft) into equivalent translational accelerations (at the centroid of the simulator). Here the equivalence refers to the fact that the pilot's seat in the simulator and the pilot's seat in the aircraft would be subject to the same accelerations. The rotational rates and accelerations are used in the transformations to produce translational accelerations. The transformed translational accelerations, along with the rotational rates (not transformed), pass to the adaptive scaling and imitating block.

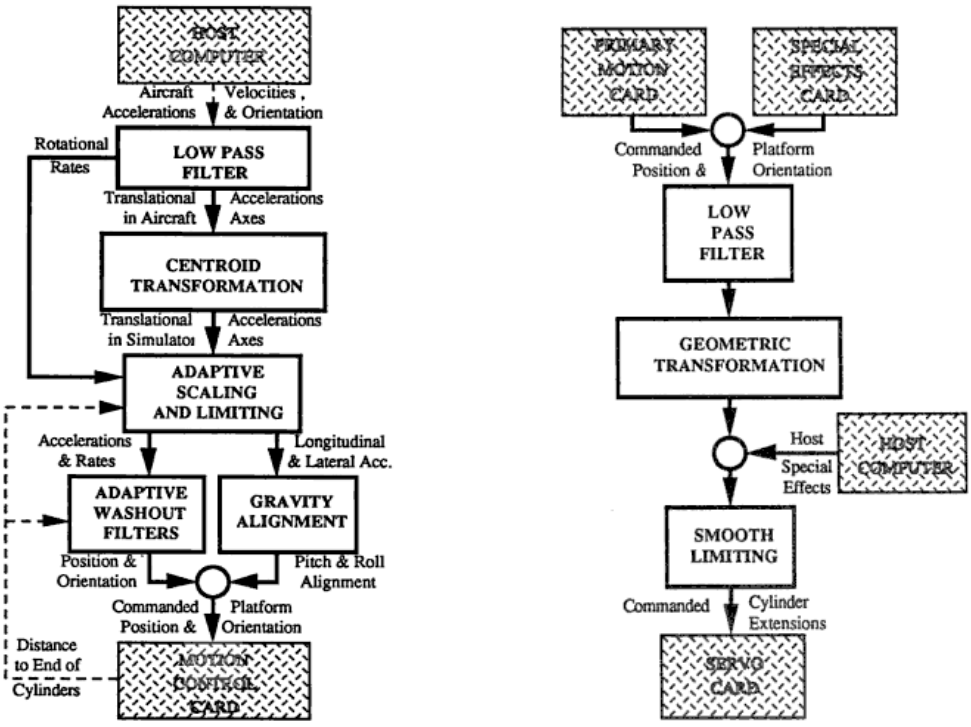

Fig.28 Motion simulation algorithm (Primary motion module block and Motion control module) [29].

This block uses the cylinders' position feedback to adjust the scale factors. When the cylinders are closing the mechanical stop, the scale factors are reduced. The feedback position signals also go to the washout filters to adjust the filters' natural frequencies adaptively—increasing the nature frequencies when the cylinders are closing the end to restrict the simulator movement with minimum introduction of false cues. The washout filters return the simulator to its neutral position at a rate under the pilot's sensory threshold. This tendency to return to neutral maximizes the allowable movement for subsequent cues. The gravity alignment block generates the sustained translation acceleration cues.

The motion control module controls the flow of signals to the servo, turns on and off the motion base, fades the source inputs in and out, calibrates separated components in position control loops, limits the motion base rates and position and also generates signals for maintenance tests. The low pass filter eliminates any stepping due to a mismatch in the iteration rate. The geometric transformation converts the platform position and orientation into six cylinders' extensions.

Fig.29, the servo module, drives the electro hydraulic valves so that the cylinder positions will track the commanded cylinder positions. The servos for each cylinder are identical, which is similar to the electro hydraulic servo system that was discussed in depth in Part A of this thesis.

There are four basic sections of the servo routine: scaling, calibration, position feedback and compensation. The scaling factors (starting with SC) are chosen to match with interfaced D/A or A/D converters. The calibration offsets (pressure, position and valve offset) are added to the loop to eliminate the hardware drifting effect to the position control loop. The most important part of the servo is the position feedback. **KP#** and **KPM#** are normally equal in magnitude and of opposite sign. The compensation network is used to damp out the oscillations introduced by mechanical resonances in the motion base when the position feedback gain is made large (to improve the tracking capabilities).

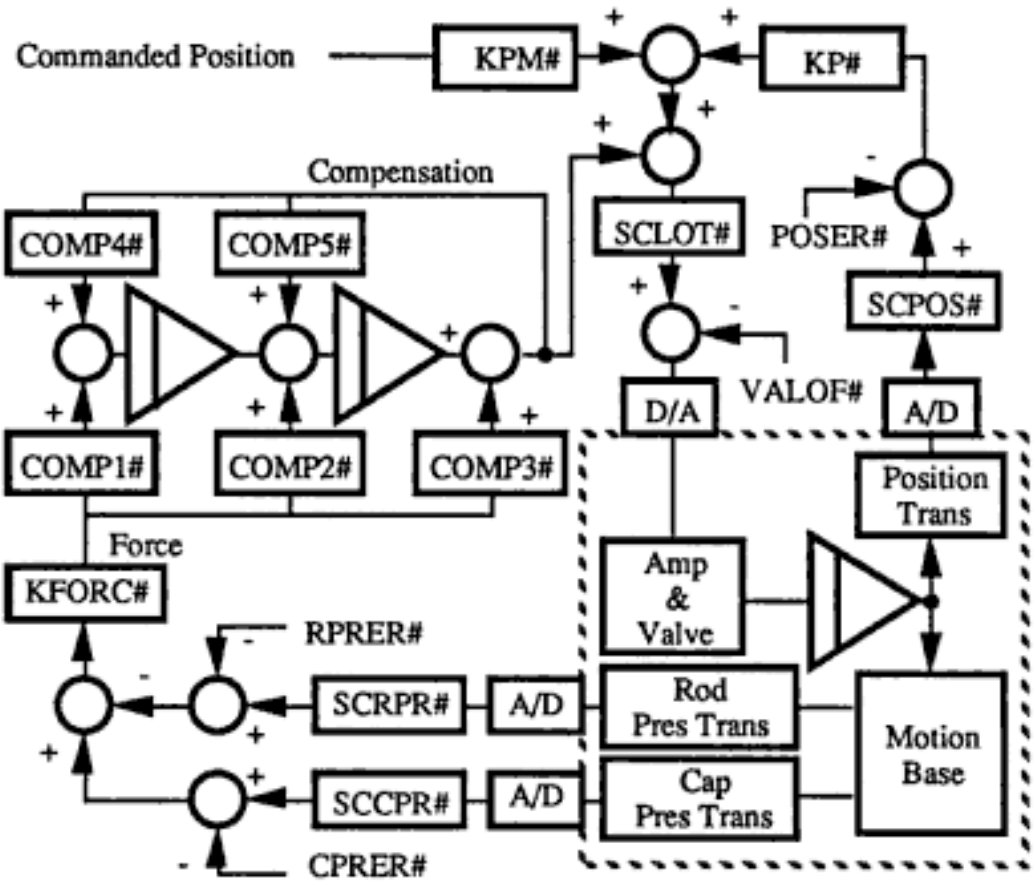

Fig.29 Motion servo block diagram [29].

10: Control loading simulation

10.1 Aircraft control system

From the pilots' perspective, simulator control loading system should be a replica of the control system of the simulated aircraft in terms of controlling and feeling. Here controlling means the pilot operates/controls the flying of simulator as if using aircraft controls to fly the aircraft. Loading refers to the pilot's perception of the same dynamic feeling in the simulator as in the simulated aircraft when moving controls. Before discussing simulator control loading systems in detail, it will help to review real aircraft control systems to realize the objective of simulator control loading simulation.

There are three main classes of aircraft control systems when it comes to the control feeling—reversible, classical irreversible and flight by wire control systems.

- Reversible flight control systems: cockpit controls are directly mechanically linked with aircraft control surfaces. Consequently, movement of the aerodynamic surface controls results in movement of the cockpit controls **Fig.30**, and the aerodynamic forces feedback to the hands of pilots directly.

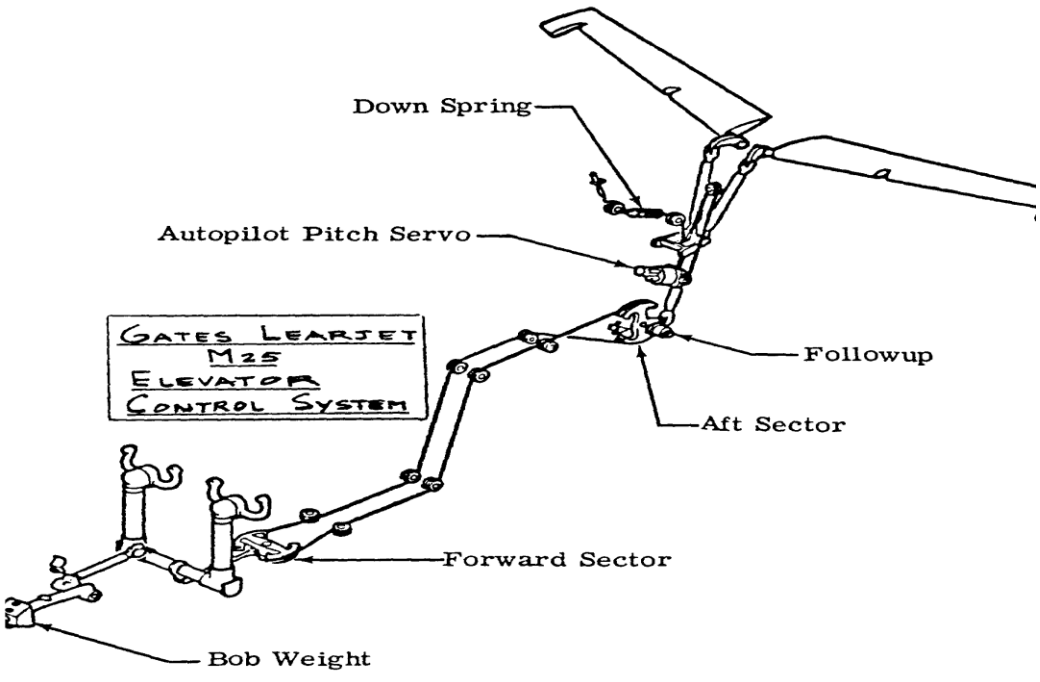

Fig.30 Example of a typical reversible flight control system [26].

- Conventional irreversible flight control systems: movement of the cockpit controls results in movement of the aerodynamic surface controls either partially or completely with the help of electro-hydraulic and/or electro-mechanical actuation devices. Movement of the aerodynamic surface controls without moving the cockpit controls is usually not possible **Fig.31**. Consequently, no direct aerodynamic feedback is provided to the pilot. In order to provide feedback forces to pilots, various "artificial feel" devices were added to generate force feedback mechanically, such as Bob weight (to generate the feel force of velocity and acceleration), springs (feel forces are functions of displacement of control sticks/control surface, effective at lower airspeed), dampers (feel forces are functions of rate of control sticks or control surfaces), and bellows (Q-feel system **Fig.32**. The feedback feel is a function of dynamic pressure on the surfaces, effective at high airspeed). Ref [26] gives a more detail description of those devices.

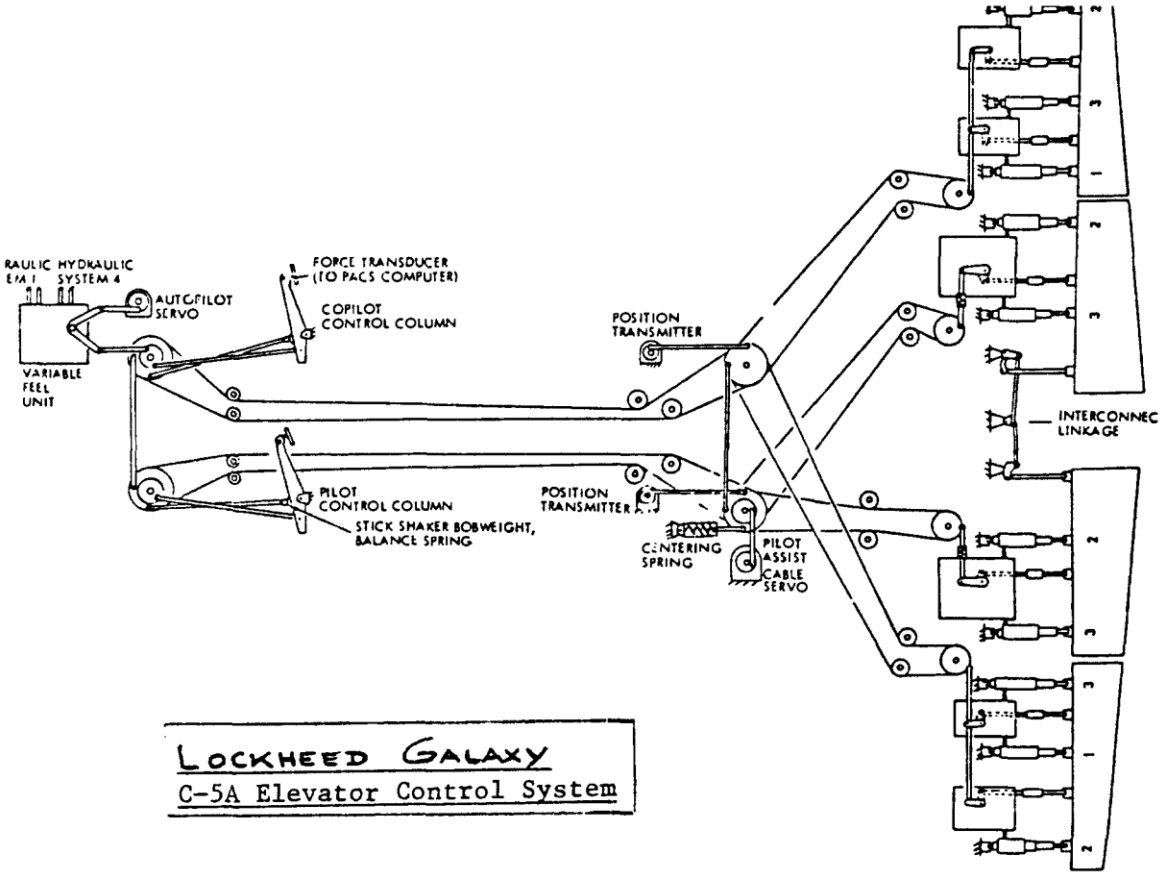

Fig.31 Example of a typical irreversible flight control system [26].

- Fly-by-wire control systems are modern flight control systems. They are irreversible systems where: the movement of flight controls are converted to electronic/light signals transmitted by wires, and flight control computers determine how to move the actuators at each control surface to provide the expected response. However, there are two different "philosophies" regarding provision of control feedback forces in modern aircraft designs. One is Boeing's approach (777/787), the movement of cockpit controls are proportional to the movement of surfaces, and the associated feedback forces are generated by paralleled feeling actuations controlled by computers. There are no major control "feeling" differences between fly-by-wire Boeing airplanes (777/787) and the earlier conventional Boeing airplanes from the pilots' perspective. However, newer Airbus airplanes (since A320) use side sticks that do not provide pilots with the conventional feedback feeling. Airbus engineers believe pilots already have enough feedback information from instrumentation, even from their own bodies, so that the traditional feedback force from controls is redundant.

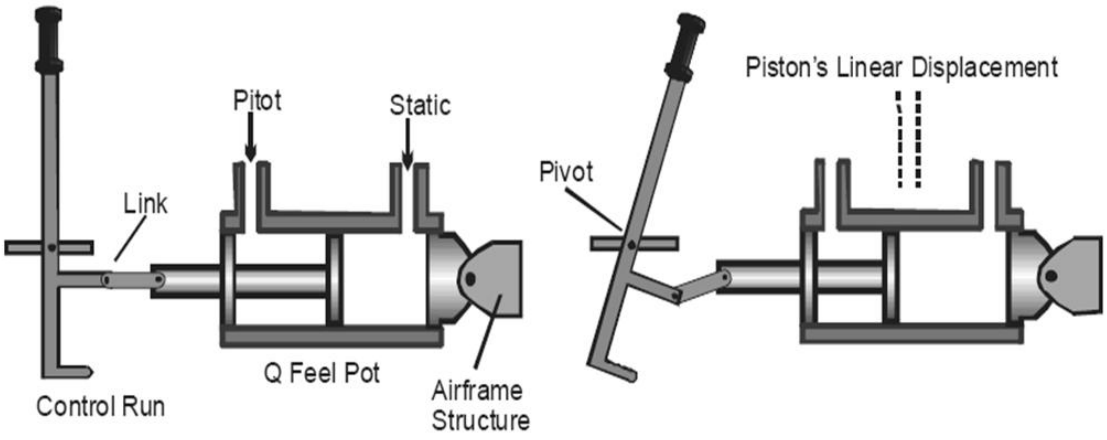

Fig.32 Q-feel system [27].

10.2 Control Surface Dynamics

An important concept of control surface dynamics is control hinge moment, which refers to the moment to turn the control surface. When the control hinge moment (from pilots or autopilot) equals aerodynamic hinge moment, the control surface is in equilibrium, resulting in a certain surface angle, and consequent airplane dynamic force. An engineering linear approximation of the aero hinge moment coefficient of elevator (**Fig. 33**) is given as follows:

$$C_{he} = C_{he0} + C_{he_\alpha}\alpha + C_{he_{\delta_e}}\delta_e + C_{he_{\dot{\delta}_e}}\dot{\delta}_e + C_{he_{\delta_t}}\delta_t + C_{he_{\dot{\delta}_t}}\dot{\delta}_t$$

Eq(20)

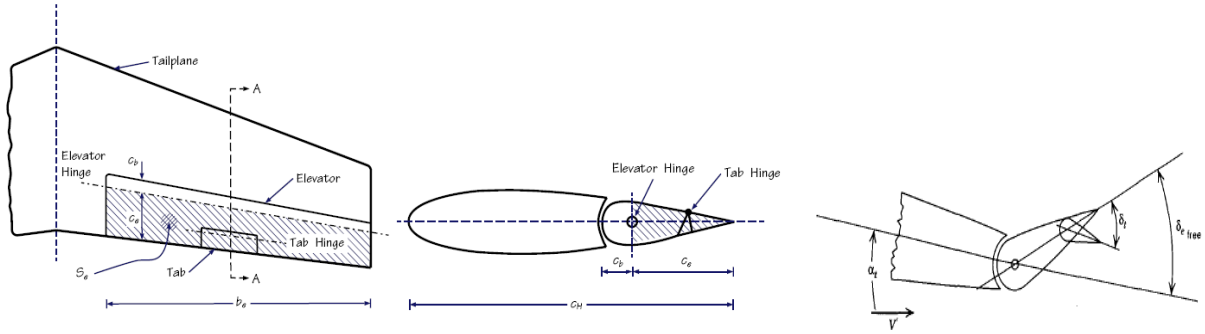

Fig.33 Elevator and tab geometry [28].

The coefficient of elevator hinge moment is defined by:

$$C_{he} = \frac{H_e}{\frac{1}{2}\rho V^2 S_e \bar{c}_e}$$

Eq(21)

Here H_e is the aero hinge moment, $\frac{1}{2}\rho V^2 S_e$ is dynamic pressure Q, and $\bar{c}_e = S_e / 2S_e$.

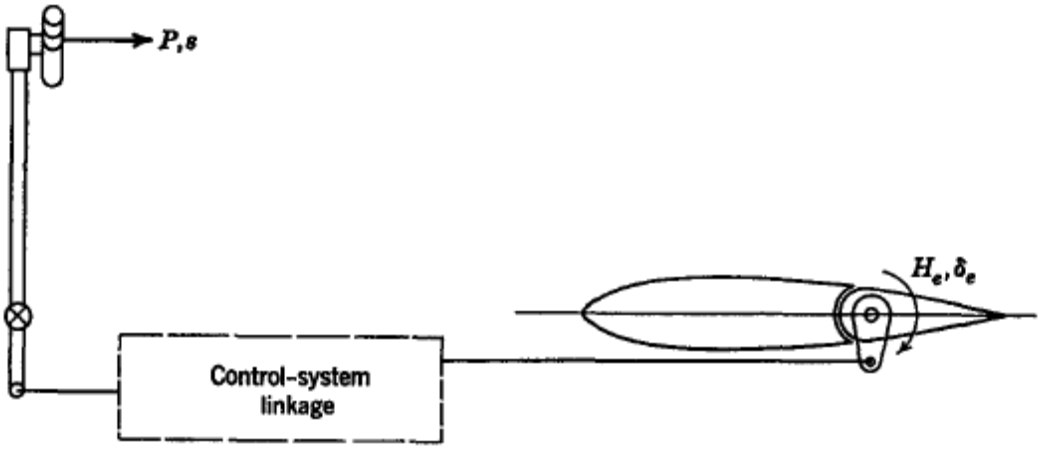

Fig.34 Schematic diagram of an elevator control system [12].

In **Fig.34**, P is the force applied by the pilot. The control-system linkage can be a pure mechanical linkage with a certain gear ratio or in power boost system with boost gearing ratio.

$$P = GH_e$$

Eq(22)

Following Etkin book [12], neglecting inertial coupling terms, the equation of motion of elevator control surface is written as:

$$I_e \ddot{\delta}_e = H_{e,\ A} + H_{e,\ C}$$

Eq(23)

The right side of the above equation has two moment terms, the one with A is the aerodynamic term and the one with C refers to the pilot control term. δ_e is elevator surface angle and I_e is the momentum of inertia of the elevator. Simulator control loading modeling is based on this equation, which will be discussed in next section. In practise, simulators are modeled according to real fight test data, or projected control dynamic data, which would include nonlinearities due to inertial coupling, and therefore the inertial coupling terms can be neglected. With accurate data and table look-up techniques, the liberalized equation (23) can be used to model control dynamic motion at the high fidelity level as required. Reference [28] introduces a different approach of control surface modeling, in where a surface model is built on a surface dynamic motion equation that includes all the inertial coupling terms.

10.3 Simulator Aero Surface Dynamic Model

Combining equations (20–23), a second-order system with variable natural frequency and damping ratio is reached as follows:

$$I\ddot{\delta} + B\dot{\delta} + G\delta = T$$

Eq(24)

Here *δ is* surface angle, *I* is surface momentum of inertia and *T* is the actual control torque applied by the pilot. *B* and *G* are combinations of hinge moment derivatives of equation (20). *B* and *G* are normally functions of airspeed, aircraft configuration and angle of attack α, etc., which are calculated by software models running at the host computer and passed to the control loading model computer. The initial condition of the above equation (24) is the equilibrium state with zero trim angle and trim speed δ_t, $\dot{\delta}_t$ = 0.

Without losing physical generality, a transitional single mass control surface model (**Fig.35**) can be used as below:

$$M_a\ddot{Z}_a + B\dot{Z}_a + KZ_a = B\dot{Z}_t + KZ_t + F_p$$

Eq(25)

The aero surface control model can be implemented in an analog computer, or a digital computer. The task that remains is to design a simulator actuation system to follow the simulated aero surface model, which can provide realistic movement and dynamic feel of the cockpit controls.

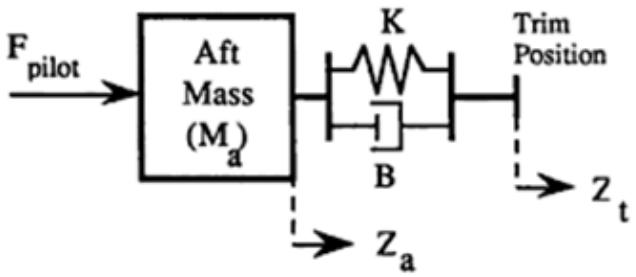

Fig.35 Single mass aircraft control surface model [29].

10.4 Analog electro-hydraulic control loading system

In this section, a conventional hydraulic control loading system with dimensional parameters the same as in reference [30] is illustrated. Control stability and control linkage compliance are reviewed. The analysis is conducted in the same manner as the cited reference but utilizing the modern tool MATLAB. It should be noted that although the cited classical research was done in the 1970s, today's control loading system found in modern simulators still follows the fundamental concept indicated in **Fig.36**.

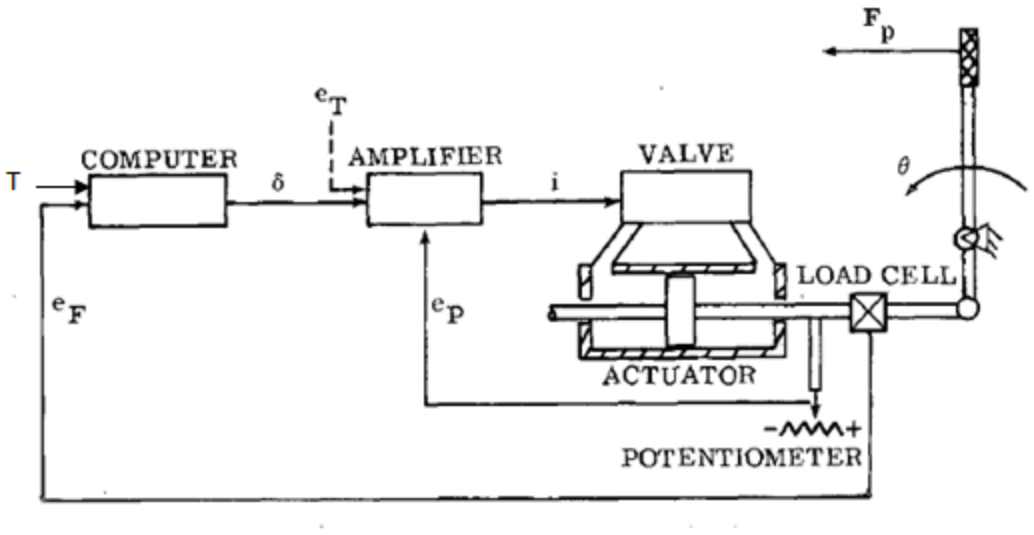

Fig.36 Electro-hydraulic control loading system [30].

As **Fig.36** indicates, this control loading system includes two closed-loops. The inner loop is an electro-hydraulic position control servo as described in part A of this thesis. The analog computer runs the aero surface model defined by Eq (24). The analog model can be programmed to provide a wide range of dynamic characteristics of control loads that occur in real aircraft. When the outer loop is closed, the actuator follows the analog computer model. Basically the control law is reference model following. The complexity of this system is that the output— θ (and also $\dot{\theta}$ $\ddot{\theta}$), and input—F_p are exerted in the same place—the column. The pilot input force is sensed by a load cell; the same load cell that also senses output acceleration.

Like any mechanical structure, the inherited natural frequency will cause resonance phenomena when the appropriate conditions are satisfied, which could cause undesired low frequency oscillation and loading effects in the output. One of important tasks is to eliminate these oscillations. Traditionally, compliant factors are taken into consideration in designing control loading systems such as shown in **Fig.37**. The hypothesis of mechanical compliance in the control linkage was substantiated by comparing the behaviour of a mathematical model of the system with experimental data. The compliant linkage spring rate k and damping coefficient c are chosen to fit the experimental result. Both the model of rigid and compliant linkage will be compared in the following section.

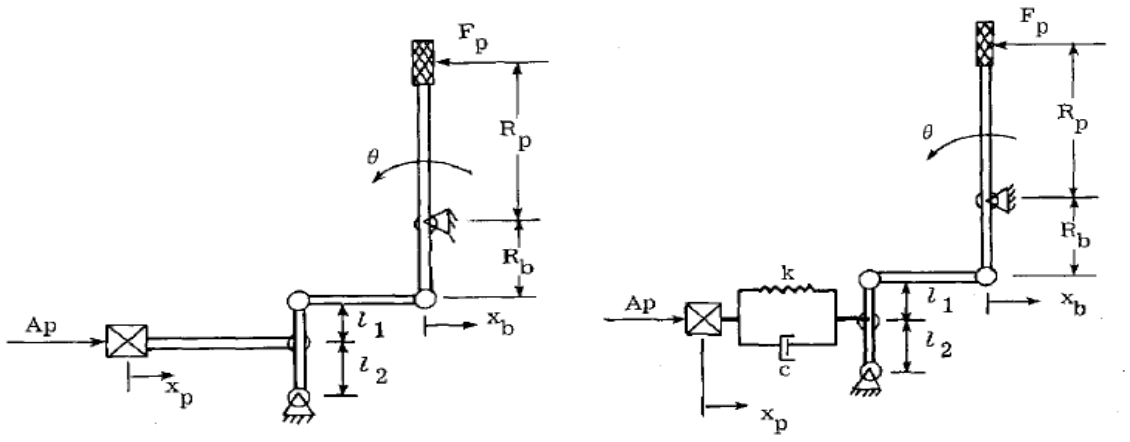

Fig.37 Rigid and compliant linkage models [30].

10.5 State space representation

Different from Part A, where a detailed EHV/cylinder model was established, an analytical model of EHV/cylinder is derived here for the purpose of state space representation. The overall dynamic behaviour of the servo-valve is presented as a second-order system:

$$\ddot{q}_\iota + 2\xi\omega_n\dot{q}_\iota + {\omega_n}^2 q_i = C_i\,{\omega_n}^2\, i$$

Eq(26)

Here i is input control current, q_i is output flow rate. C_i is valve current gain at nominal operating point.

Actuator flow rate:

$$q = q_i - C_p p$$

Eq(27)

Here p is the pressure difference of two chambers of the actuator—the load pressure. Valve pressure gain $C_p = -\frac{\partial q}{\partial p}$.

From flow continuity equation also gets

$$q = A\dot{x_p} + (\frac{V_E}{4\beta})\dot{p}$$

Eq(28)

Here A is the actuator piston area, x_p is the displacement of actuator piston, V_E is the effective volume of compressed fluid, and β is the bulk modulus.

The control column dynamic

$$R_p F_p + \alpha R_b A p = J\ddot{\theta}$$

Eq(29)

Expressed in terms of the displacement of the base of the column x_b

$$\ddot{x_b} = \left(\frac{\alpha {R_b}^2 A}{J}\right) p + \left(\frac{R_b R_p}{J}\right) F_p$$

Eq(30)

Here R_p is the lever arm of pilot force, R_b is the lever arm of pilot force, α is the linkage ratio, and J is the moment of inertia of column.

For rigid linkage model, the above equation can be expressed in terms of actuator displacement x_p

$$\ddot{x_p} = \left(\frac{\alpha^2 {R_b}^2 A}{J}\right) p + \left(\frac{\alpha\, R_b R_p}{J}\right) F_p$$

Eq(31)

For complaint linkage, spring rate *k* and damping coefficient c have to be included in the equation

$$Ap = k\left(x_p - \alpha x_b\right) + c(\dot{x_p} - \alpha \dot{x_b})$$

Eq(32)

Rearranged in the following manner

$$\dot{x_p} = -\left(\frac{k}{c}\right) x_p + \left(\frac{A}{c}\right) p + \left(\frac{\alpha k}{c}\right) x_b + \alpha \dot{x_b}$$

Eq(33)

Take a close look at the output of the linkage load cell, which inputs to the computer model. The model equation is rewritten here

$$I\ddot{\delta} + B\dot{\delta} + G\delta = T + loadcell$$

Eq(34)

At the free control condition where pilot force input $Fp = 0$, the model now is driven by the host computer force T only if load cell output $loadcell = 0$. However $loadcell \neq 0$ when cylinder accelerates, and load cell would pick up the inertial force due to acceleration above the measurement device $m_{loadcell}$ [32]. To clarify, this output is due to movement of the reference frame (control column here), and it takes the reverse direction of the acceleration. Here $m_{loadcell}$ is not the actual mass of the load cell, but the effective mass that can be derived precisely by measuring the amplitude of oscillation rings of the output of load cell. When $Fp \neq 0$, pushing or pulling elevator control, load cell output equals pilot-applied force subtracted from the inertial force term mentioned above. Taking account of gearing ratio, the semi-empirical output equation of load cell becomes

$$loadcell = (\frac{R_p}{\alpha\, R_b})Fp - \alpha\, \ddot{x_b} m_{loadcell}$$

Eq(35)

Acceleration is proportional to total resulting force summation. When $Fp = 0$, the second term of Eq(35) can be written as $-KAp$, K is an undetermined constant as $m_{loadcell}$, which also can be derived from actual measurement. When $Fp \neq 0$, the second term is $-K(\left(\frac{R_p}{\alpha\, R_b}\right) Fp + Ap)$.

Steady space equations for different input cases (free control case and pilot control case) and of both rigid and compliant linkage systems are given below.

Free control state space equation for control loading system with assumed rigid linkage:

$$\frac{d}{dt}\begin{bmatrix} x_p \\ \dot{x_p} \\ p \\ q_i \\ \dot{q_i} \\ \delta \\ \dot{\delta} \end{bmatrix} = \begin{bmatrix} 0 & 1 & 0 & 0 & 0 & 0 & 0 \\ 0 & 0 & \alpha^2 {R_b}^2 A/J & 0 & 0 & 0 & 0 \\ 0 & -4A\beta/V_E & -4\beta C_p/V_E & 4\beta/V_E & 0 & 0 & 0 \\ 0 & 0 & 0 & 0 & 1 & 0 & 0 \\ -C_i {\omega_n}^2 K_2 K_3 & 0 & 0 & -{\omega_n}^2 & -2\xi\omega_n & C_i {\omega_n}^2 K_2 & 0 \\ 0 & 0 & 0 & 0 & 0 & 0 & 1 \\ 0 & 0 & -K_1 KGA/I & 0 & 0 & -G/I & -B/I \end{bmatrix} \begin{bmatrix} x_p \\ \dot{x_p} \\ p \\ q_i \\ \dot{q_i} \\ \delta \\ \dot{\delta} \end{bmatrix} + \begin{bmatrix} 0 \\ 0 \\ 0 \\ 0 \\ 0 \\ 0 \\ G/I \end{bmatrix} T$$

Eq(36)

Free control state space equation for control loading system with assumed complaint linkage:

$$\frac{d}{dt}\begin{bmatrix} x_p \\ p \\ q_i \\ \dot{q}_\iota \\ \delta \\ \dot{\delta} \\ x_p \\ \dot{x_b} \end{bmatrix} = \begin{bmatrix} -k/c & A/c & 0 & 0 & 0 & 0 & \alpha k/c & \alpha \\ 4A\beta k/V_E c & -4\beta(A^2 + C_p c)/V_E c & 4\beta/V_E & 0 & 0 & 0 & -4A\beta\alpha k/V_E c & -4A\beta\alpha/V_E \\ 0 & 0 & 0 & 1 & 0 & 0 & 0 & 0 \\ -C_i {\omega_n}^2 K_2 K_3 & 0 & -{\omega_n}^2 & -2\xi\omega_n & C_i {\omega_n}^2 K_2 & 0 & 0 & 0 \\ 0 & 0 & 0 & 0 & 0 & 1 & 0 & 0 \\ 0 & -K_1 KGA/I & 0 & 0 & -G/I & -B/I & 0 & 0 \\ 0 & 0 & 0 & 0 & 0 & 0 & 0 & 1 \\ 0 & \alpha {R_b}^2 A/J & 0 & 0 & 0 & 0 & 0 & 0 \end{bmatrix} \begin{bmatrix} x_p \\ p \\ q_i \\ \dot{q}_\iota \\ \delta \\ \dot{\delta} \\ x_p \\ \dot{x_b} \end{bmatrix}$$

$$+ \begin{bmatrix} 0 \\ 0 \\ 0 \\ 0 \\ 0 \\ G/I \\ 0 \\ 0 \end{bmatrix} T$$

Eq(37)

Pilot control state space equation for control loading system with assumed rigid linkage:

$$\frac{d}{dt}\begin{bmatrix} x_p \\ \dot{x_p} \\ p \\ q_i \\ \dot{q}_\iota \\ \delta \\ \dot{\delta} \end{bmatrix} = \begin{bmatrix} 0 & 1 & 0 & 0 & 0 & 0 & 0 \\ 0 & 0 & \alpha^2 {R_b}^2 A/J & 0 & 0 & 0 & 0 \\ 0 & -4A\beta/V_E & -4\beta C_p/V_E & 4\beta/V_E & 0 & 0 & 0 \\ 0 & 0 & 0 & 0 & 1 & 0 & 0 \\ -C_i {\omega_n}^2 K_2 K_3 & 0 & 0 & -{\omega_n}^2 & -2\xi\omega_n & C_i {\omega_n}^2 K_2 & 0 \\ 0 & 0 & 0 & 0 & 0 & 0 & 1 \\ 0 & 0 & -K_1 KGA/I & 0 & 0 & -G/I & -B/I \end{bmatrix} \begin{bmatrix} x_p \\ \dot{x_p} \\ p \\ q_i \\ \dot{q}_\iota \\ \delta \\ \dot{\delta} \end{bmatrix}$$

$$+ \begin{bmatrix} 0 \\ \alpha R_b R_p/J \\ 0 \\ 0 \\ 0 \\ 0 \\ \left(\frac{K_1 G}{I}\right)\left(\frac{R_p}{R_b \alpha}\right)(1-K) \end{bmatrix} F_p$$

Eq(38)

Pilot control state space equation for control loading system with assumed complaint linkage:

$$\frac{d}{dt}\begin{bmatrix} x_p \\ p \\ q_i \\ \dot{q}_\iota \\ \delta \\ \dot{\delta} \\ x_p \\ \dot{x_b} \end{bmatrix} = \begin{bmatrix} -k/c & A/c & 0 & 0 & 0 & 0 & \alpha k/c & \alpha \\ 4A\beta k/V_E c & -4\beta(A^2 + C_p c)/V_E c & 4\beta/V_E & 0 & 0 & 0 & -4A\beta\alpha k/V_E c & -4A\beta\alpha/V_E \\ 0 & 0 & 0 & 1 & 0 & 0 & 0 & 0 \\ -C_i{\omega_n}^2 K_2 K_3 & 0 & -{\omega_n}^2 & -2\xi\omega_n & C_i{\omega_n}^2 K_2 & 0 & 0 & 0 \\ 0 & 0 & 0 & 0 & 0 & 1 & 0 & 0 \\ 0 & -K_1 KGA/I & 0 & 0 & -G/I & -B/I & 0 & 0 \\ 0 & 0 & 0 & 0 & 0 & 0 & 0 & 1 \\ 0 & \alpha{R_b}^2 A/J & 0 & 0 & 0 & 0 & 0 & 0 \end{bmatrix} \begin{bmatrix} x_p \\ p \\ q_i \\ \dot{q}_\iota \\ \delta \\ \dot{\delta} \\ x_p \\ \dot{x_b} \end{bmatrix}$$

$$+ \begin{bmatrix} 0 \\ 0 \\ 0 \\ 0 \\ 0 \\ \left(\frac{K_1 G}{I}\right)\left(\frac{R_p}{R_b \alpha}\right)(1-K) \\ 0 \\ R_b R_p/J \end{bmatrix} F_p$$

Eq(39)

10.6 Stability analysis

The stability analysis is conducted in a same manner as in reference [30], which utilizes a classical method to determine the open loop stability margin using Bode diagram. Opening the model output to the inner loop, and inputting e_T to servo at free control $F_p = 0$, servo control current i becomes:

$$i = K_2(e_T - K_3 x_p)$$

Eq(40)

Open loop rigid linkage system state space equation:

$$\frac{d}{dt}\begin{bmatrix} x_p \\ \dot{x_p} \\ p \\ q_i \\ \dot{q}_\iota \\ \delta \\ \dot{\delta} \end{bmatrix} = \begin{bmatrix} 0 & 1 & 0 & 0 & 0 & 0 & 0 \\ 0 & 0 & \alpha^2{R_b}^2 A/J & 0 & 0 & 0 & 0 \\ 0 & -4A\beta/V_E & -4\beta C_p/V_E & 4\beta/V_E & 0 & 0 & 0 \\ 0 & 0 & 0 & 0 & 1 & 0 & 0 \\ -C_i{\omega_n}^2 K_2 K_3 & 0 & 0 & -{\omega_n}^2 & -2\xi\omega_n & 0 & 0 \\ 0 & 0 & 0 & 0 & 0 & 0 & 1 \\ 0 & 0 & K_1 GmaxA/I & 0 & 0 & -G/I & -B/I \end{bmatrix} \begin{bmatrix} x_p \\ \dot{x_p} \\ p \\ q_i \\ \dot{q}_\iota \\ \delta \\ \dot{\delta} \end{bmatrix} + \begin{bmatrix} 0 \\ 0 \\ 0 \\ 0 \\ C_i{\omega_n}^2 K_2 \\ 0 \\ 0 \end{bmatrix} e_T$$

Eq(41)

Open loop compliant linkage system state space equation:

$$\frac{d}{dt}\begin{bmatrix} x_p \\ p \\ q_i \\ \dot{q}_i \\ \delta \\ \dot{\delta} \\ x_p \\ \dot{x}_b \end{bmatrix} = \begin{bmatrix} -k/c & A/c & 0 & 0 & 0 & 0 & \alpha k/c & \alpha \\ 4A\beta k/V_E c & -4\beta(A^2 + C_p c)/V_E c & 4\beta/V_E & 0 & 0 & 0 & -4A\beta\alpha k/V_E c & -4A\beta\alpha/V_E \\ 0 & 0 & 0 & 1 & 0 & 0 & 0 & 0 \\ -C_i{\omega_n}^2 K_2 K_3 & 0 & -{\omega_n}^2 & -2\xi\omega_n & 0 & 0 & 0 & 0 \\ 0 & 0 & 0 & 0 & 0 & 1 & 0 & 0 \\ 0 & K_1 GmaxA/I & 0 & 0 & -G/I & -B/I & 0 & 0 \\ 0 & 0 & 0 & 0 & 0 & 0 & 0 & 1 \\ 0 & \alpha {R_b}^2 A/J & 0 & 0 & 0 & 0 & 0 & 0 \end{bmatrix} \begin{bmatrix} x_p \\ p \\ q_i \\ \dot{q}_i \\ \delta \\ \dot{\delta} \\ x_p \\ \dot{x}_b \end{bmatrix} + \begin{bmatrix} 0 \\ 0 \\ 0 \\ C_i{\omega_n}^2 K_2 \\ 0 \\ 0 \\ 0 \\ 0 \end{bmatrix} e_T$$

Eq(42)

The resulting Bode diagram (**Fig.45**) depicts both rigid and compliant systems' frequency responses for easy comparison. The particular simulated mode with parameters $I = 67.79\ Ncms^2$, $B = 343.37\ Ncms$, $G = 10847\ Ncm/rad$. It clearly indicates that the compliance of linkage results in insatiability at a frequency of about 12 Hz. In simulators, periodically pushing/pulling at certain frequencies could excite control oscillation, and eventually triggers a safety protection circuit that is designed to power off the control loading when the oscillation exceeds its limits. A qualitative explanation is that the natural frequency of the mechanical system is excited, causing resonance.

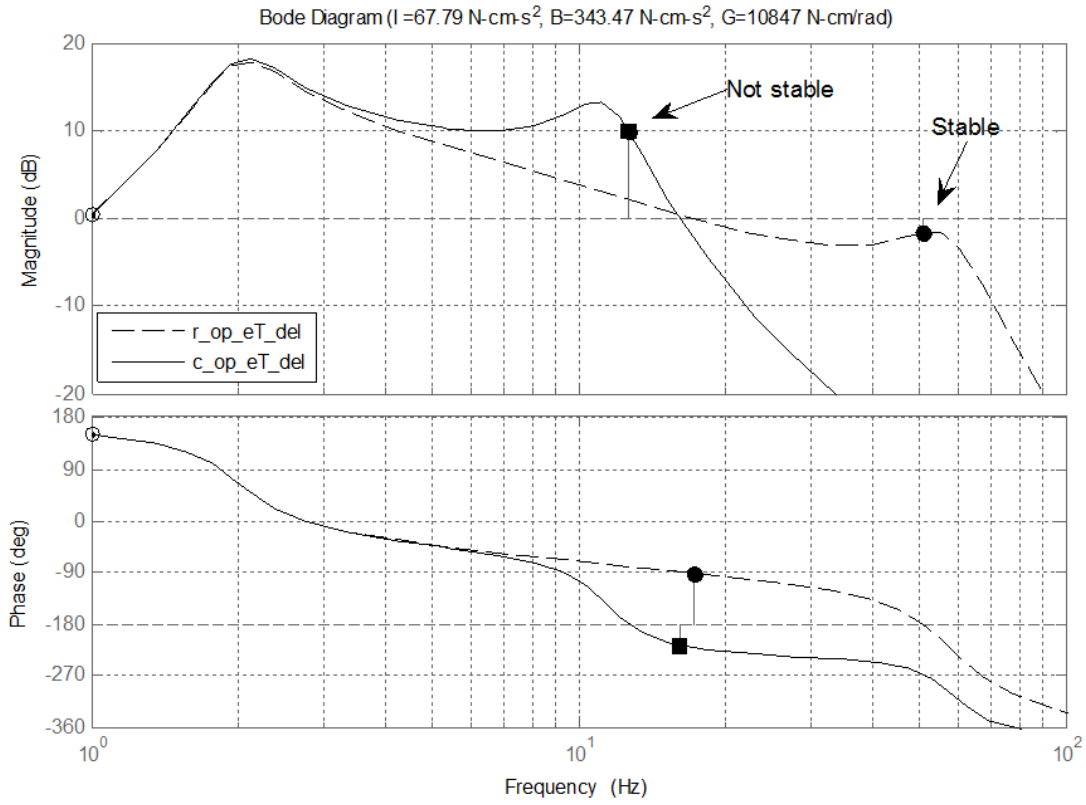

Fig.38 δ/e_T Bode diagram (open outer loop).

Due to the inevitable existence of mechanical compliance, in the early development stages of the above control loading system architecture, many analytic and practical efforts were devoted to keeping the electro-hydraulic system stable as the profile range of the simulated model changes. As examined in part A of this thesis, ideally the inner loop should be designed to respond rapidly, be critically damped, and have a wide bandwidth. However, in practice the inner loop (hydraulic servo) had been designed to be somewhat over damped in order to maintain critically damped overall system behaviour. The compliance of linkage was considered to be a cause of the insatiability of the system at certain frequencies [30]. This realization had important influence on later studies of control loading systems and had an impact on earlier industry products. For example, the over damping design of analog hydraulic servos can be found in control loading servos in vintage simulators. Furthermore, the digital control loading that will be discussed later also has been used in an attempt to eliminate the collisions by compensation of the filtering network.

10.7 Regulatory Requirement

Before examining the performance of the above control loading system, let's review the regulatory requirement of simulator control loading, which acts as the design objective of any control loading system of simulators used for civilian pilot training.

FAR Part 60 states:

"Simulator control feel dynamics must replicate the airplane. This must be determined by comparing a recording of the control feel dynamics of the simulator to airplane measurements. For initial and upgrade qualification evaluations, the control dynamic characteristics must be measured and recorded directly from the flight deck controls, and must be accomplished in takeoff, cruise, and landing flight conditions and configurations." [33]

"Compliance with this requirement is determined by comparing a recording of the control feel dynamics of the FFS to actual airplane measurements in the takeoff, cruise and landing configurations." [33]

"Recordings such as free response to an impulse or step function are classically used to estimate the dynamic properties of electromechanical systems. In any case, it is only possible to estimate the dynamic properties as a result of being able to estimate true inputs and responses." [33]

As mentioned before, there are two different ways to apply force to the controls column. One is the pilot force, which is forward; another is the reversing forces that come from the surface model. Because of the difficulty of measuring of the pilot input force precisely, FAA suggests using the free response test shown in **Figs.39** and **40** as a means to validate simulated control dynamics. In a real aircraft, for example, for a reversible elevator control channel, the kinematic of control column is a function of,

indistinguishably, two force variables: surface force and pilot force. However, the structure of control loading discussed above has fundamental flaw due to the utilization of load cell, in which not only the surface force (e.g. Trim force T) and pilot input force but also the load cell inertial force part are fed to the dynamic model computer. It will be seen later that the load cell inertial force part generates oscillating noises with a frequency similar to the natural frequency of mechanical linkage, which is unwanted signal. Perfect simulation of flight control is very difficult to attain, if not impossible, due to this difference between real aircraft control and control loading simulation structures.

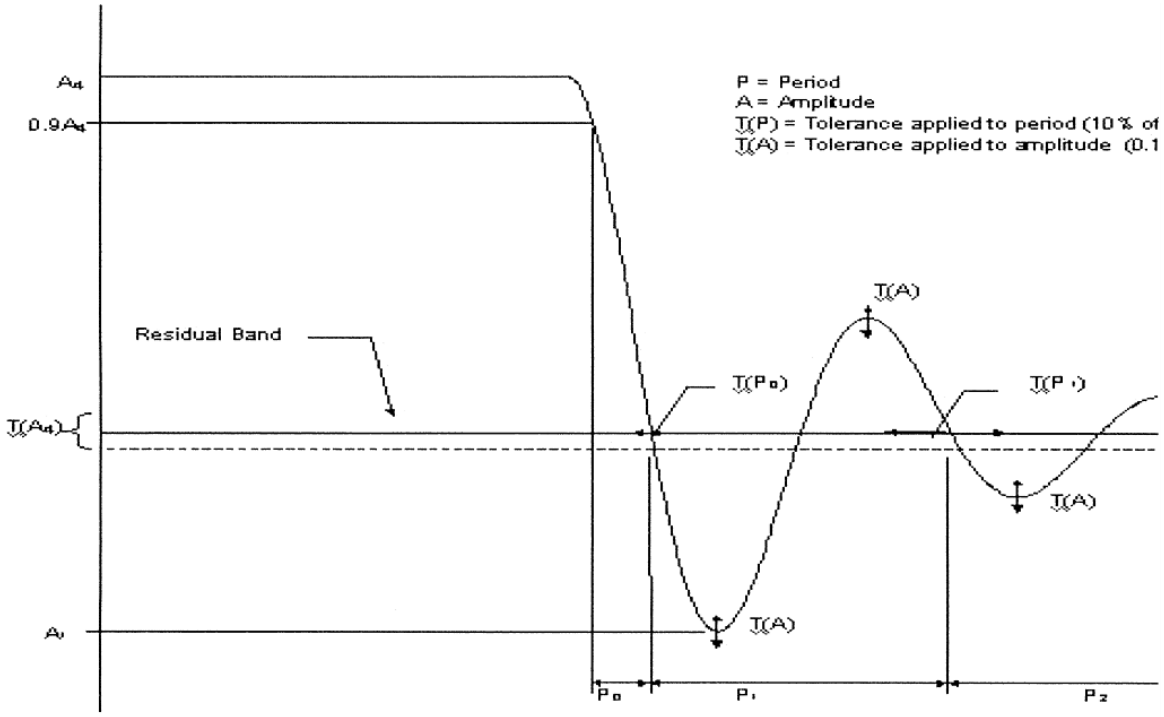

Fig.39 Under-damped step response [33].

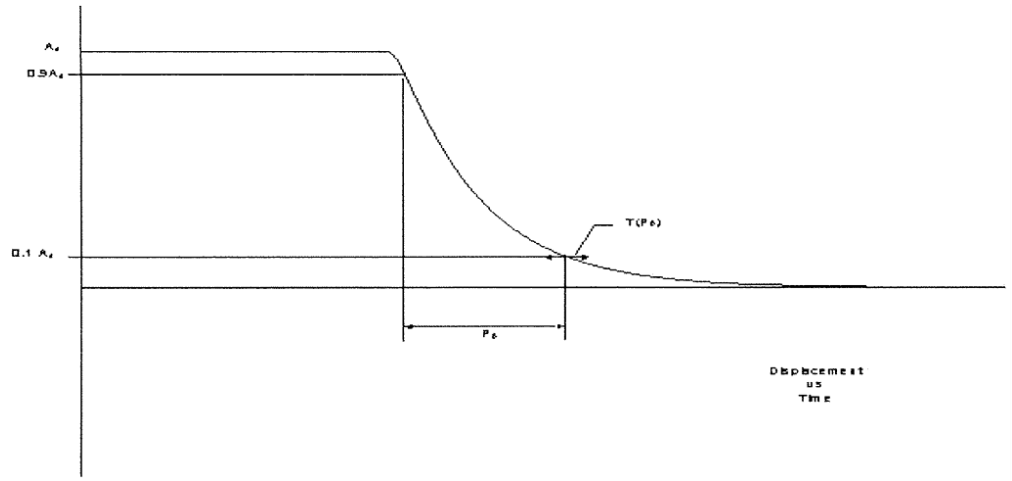

Figure A2B
Critically and Overdamped Step Response

Fig.40 Critically and over-damped step response [33].

10.8 State space model result and discussion

In the following step response tests, for comparison purposes, the model part is taken out of the loop and fed with the same input to generate the characteristic response of simulated aircraft control dynamics. This response is labelled as "model." Besides the output control column position *xb*, the cylinder force *Ap* and load cell output *loadcell* are illustrated as well. Results are compared between the free response and pilot control response; low damped model and high damped model; rigid linkage and compliant linkage.

1. In free response (**Figs.41** and **42**): *xb* basically follows *model* but has phase lag compared to the *model*. There are no noticeable difference between rigid and compliant linkage model responses. Load cell output is simply a portion (1/10, dependent on the actual measurement of *m_loadcell* or *K*) of cylinder force *Ap*. Minor differences in *Ap* can be noticed between rigid and compliant linkage in the initial period, which is the result of the *Ap* fluctuating due to compliant collisions.
2. Pilot applied force response (**Figs.43** and **44**)**:** *xb* follows *model* for both lower and high damping cases, but also has a phase lag. However, for compliant linkage, there is a noticeable unevenness in the response. Higher frequency oscillations are noticed at the *Ap* and *loadcell* for the complaint linkage. The frequency can be roughly calculated to be 12 Hz, which coincides with

the resonant frequency observed in the Bode diagram. Due to the load cell's high frequency output rings, there are noticeable distortion in the xb.

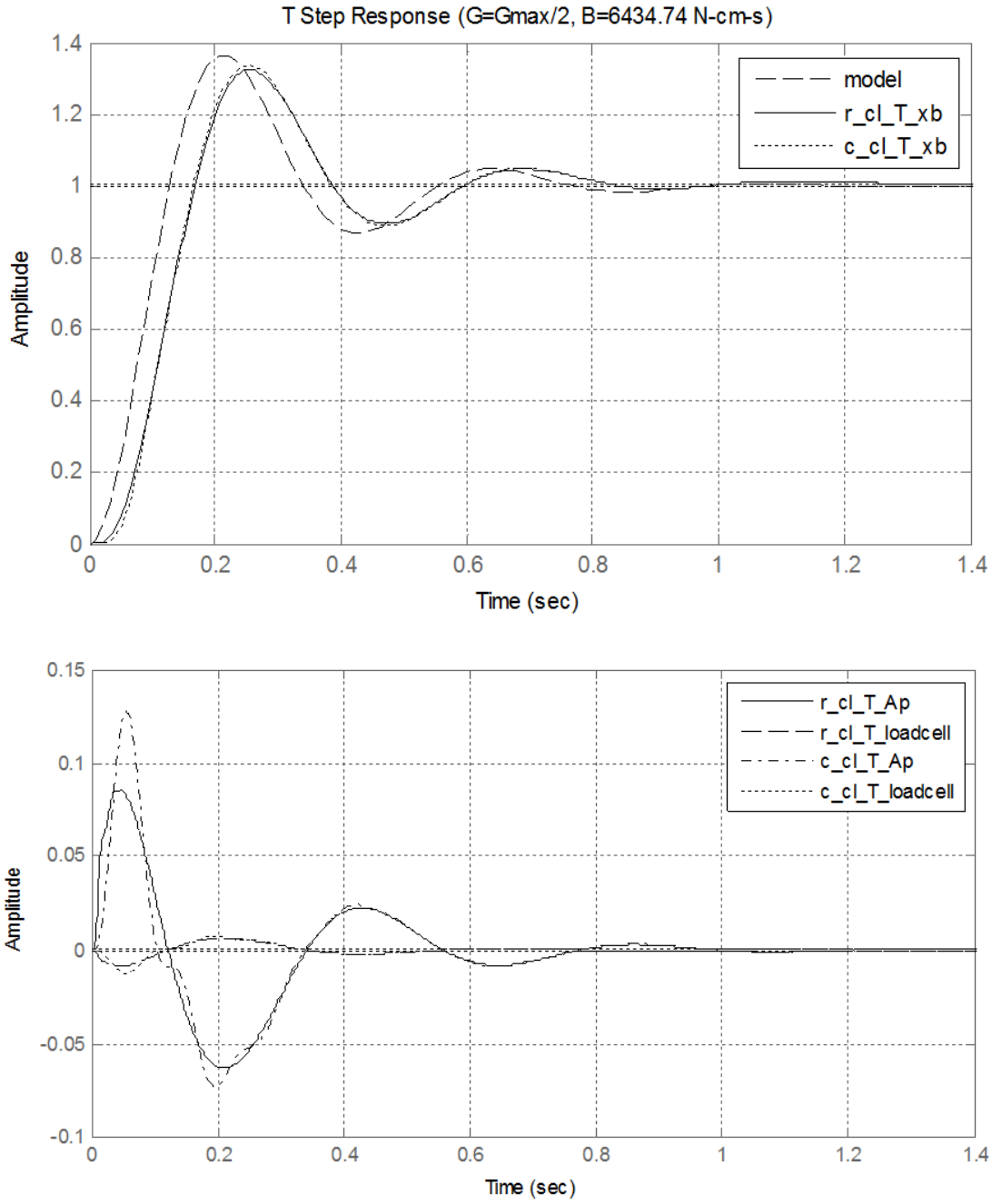

Fig.41 Trim force T step response (lower damp case).

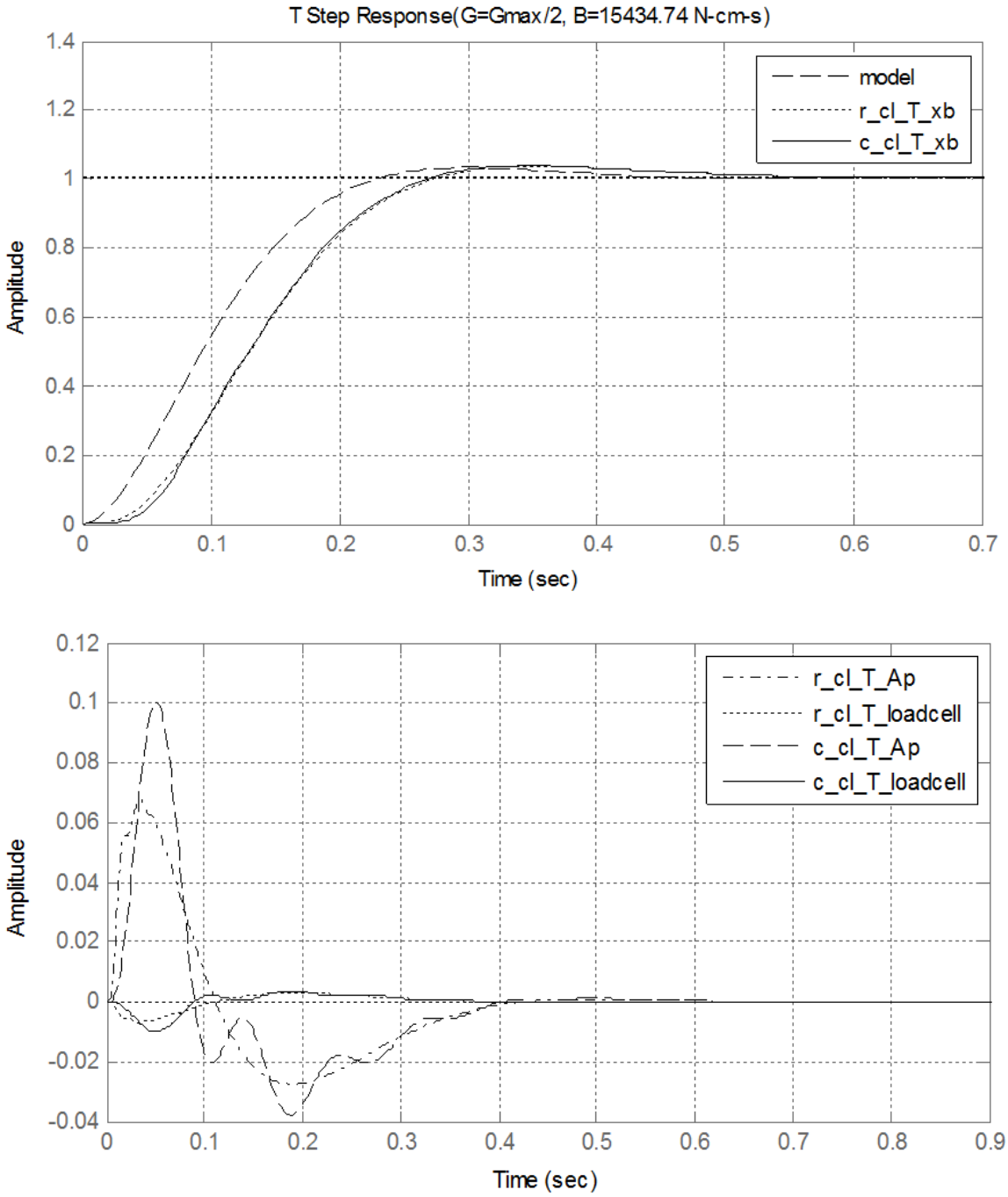

Fig.42 Trim Force T Step Response (high damp case).

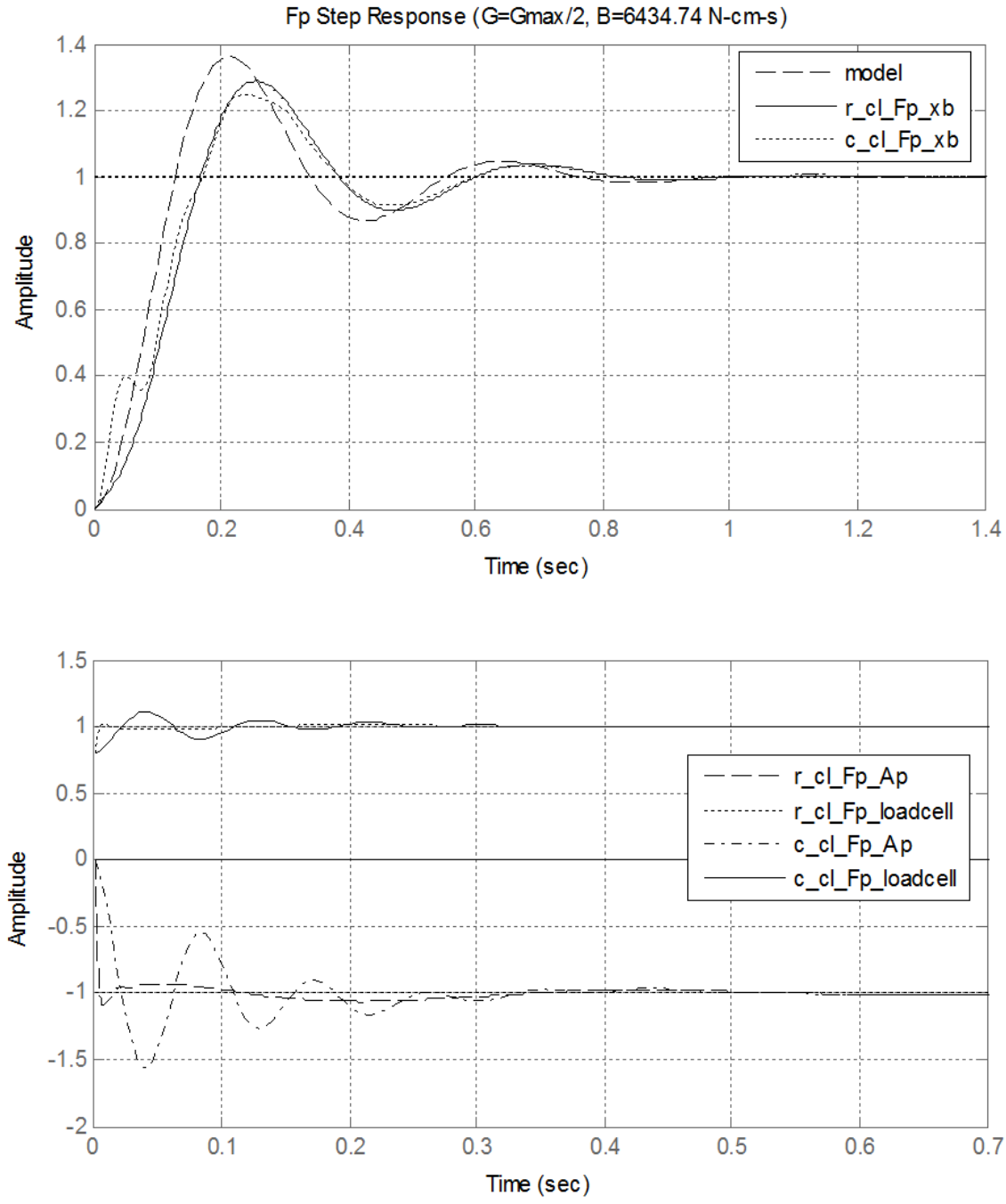

Fig.43 Pilot force Fp step responses (lower damp case).

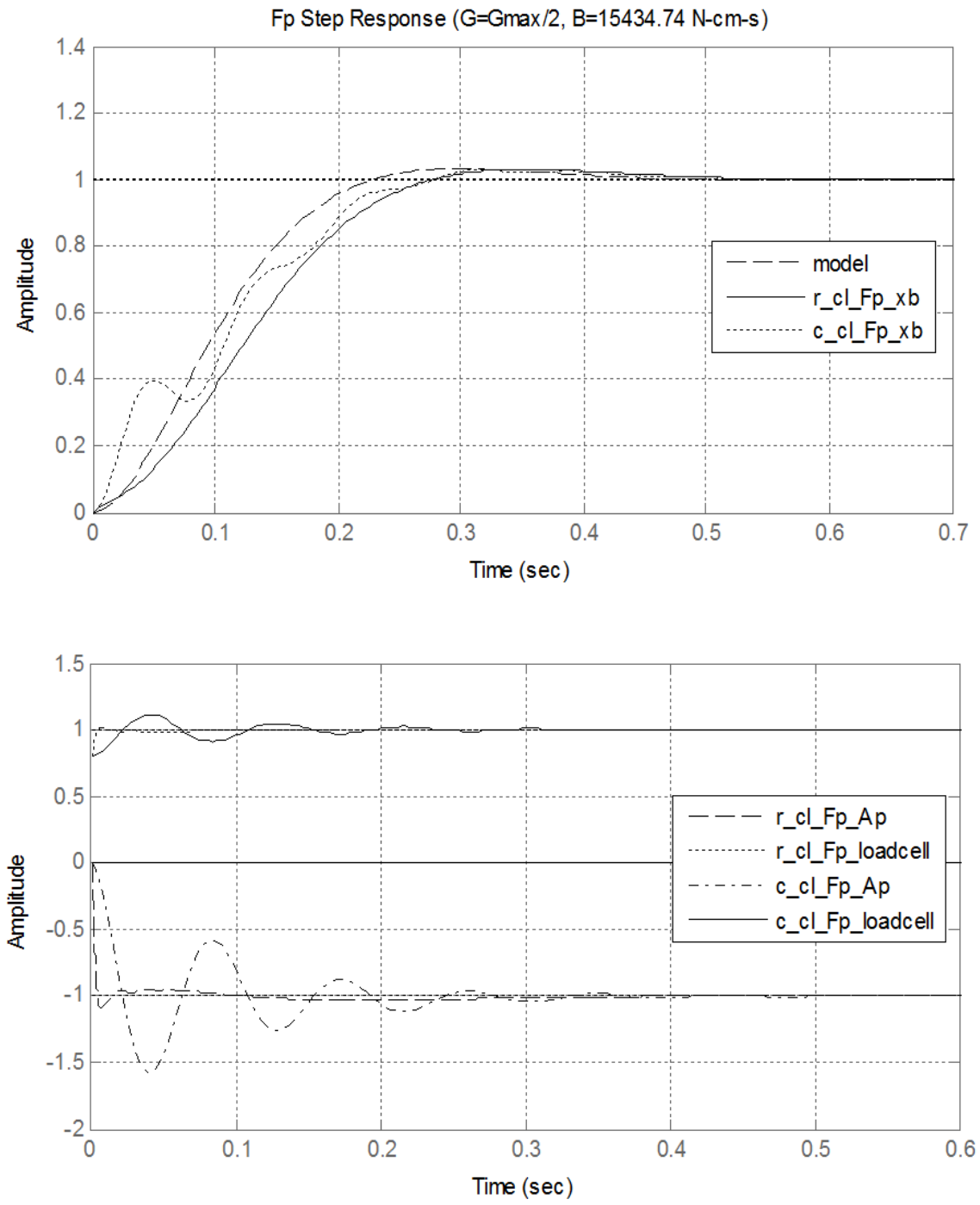

Fig.44 Pilot Force Fp Step Response (High damp case).

From the resulting responses, it can be seen that the linkage compliance assumption is correct. The position following control implementation is able to accomplish the simulation task. However, concerns about stability and unevenness of controls still exist. Research was done to reduce the distortion caused by the compliant resonance, because pilots could feel the annoying oscillating. One proposed solution

was to use state feedback networked with a gain matrix optimized by quadratic optimal method [30]. The optimization computing was resorted to as a discrete dynamic programming algorithm, which can reach a result similar to that of using the MATLAB command **lpr**, but is much more tedious. This proposed new structure has influenced the next generation of digital control loading systems.

10.9 Control loading Simulink Model

Simulink modeling of control loading utilizes the resultant EHV/cylinder model that was developed in Part A. The EHV/cylinder Simulink model that was developed is plugged into the same control loading channel discussed in previous sections. The compliance of linkage is also taken into account. A symbolical model with the same control implementation—model position following—is constructed first, then followed by a different control scheme implementation—model velocity following.

The linkage model is demonstrated in **Fig.45**. It includes the model of compliance of linkage with a natural frequency of 12 Hz. It has also incorporated the semi-empirical load cell model. The assumption is that the linkage is frictionless in both static and Coulomb. It must be noted that frictions that exist in real aircraft control channels could be simulated by particular software algorithms and sent to the control loading by the host computer, which is different from that of the control loading linkage. Certainly the load cell will affected by the friction force. However, in normal working conditions, the friction concerned is very small, and can be safety ignored. When the friction of the linkage becomes abnormal, in some cases, pilot can “feel” it, which indicates that control loading system maintenance is required.

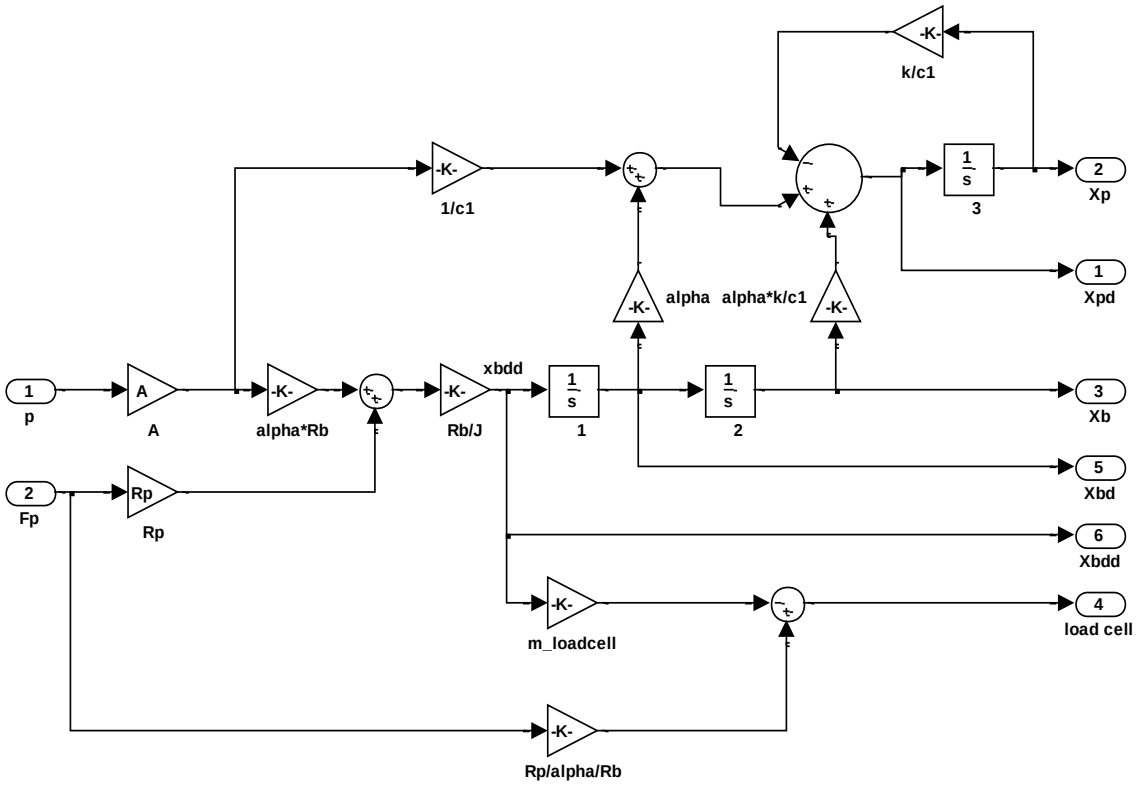

Fig.45 Linkage and Load cell.

10.9.1 Position follower

In the block structure of **Fig.46**, the EHV block is exactly same as in Part A. The actuator and linkage block of **Fig.47** includes the linkage model shown in **Fig.45**. The off-line model provides the baseline of the objective response curve; it stands for the aircraft response characteristic.

Figs. 48 and **49** illustrate the results of the position follower. The *xb* responses still have phase lags the same as those noticed at the state space mode. This is due to the inherited limitation of the position following—slower speed and negative feedback control law. But the responses here are smoother, even though all control parameters are adjusted to match those of the state space model. The smoother results come from the correct modelling of EHV. In order to construct the state space model in the previous section, the EHV is represented as a second order system, and some important nonlinear characteristics of EHV have been dropped.

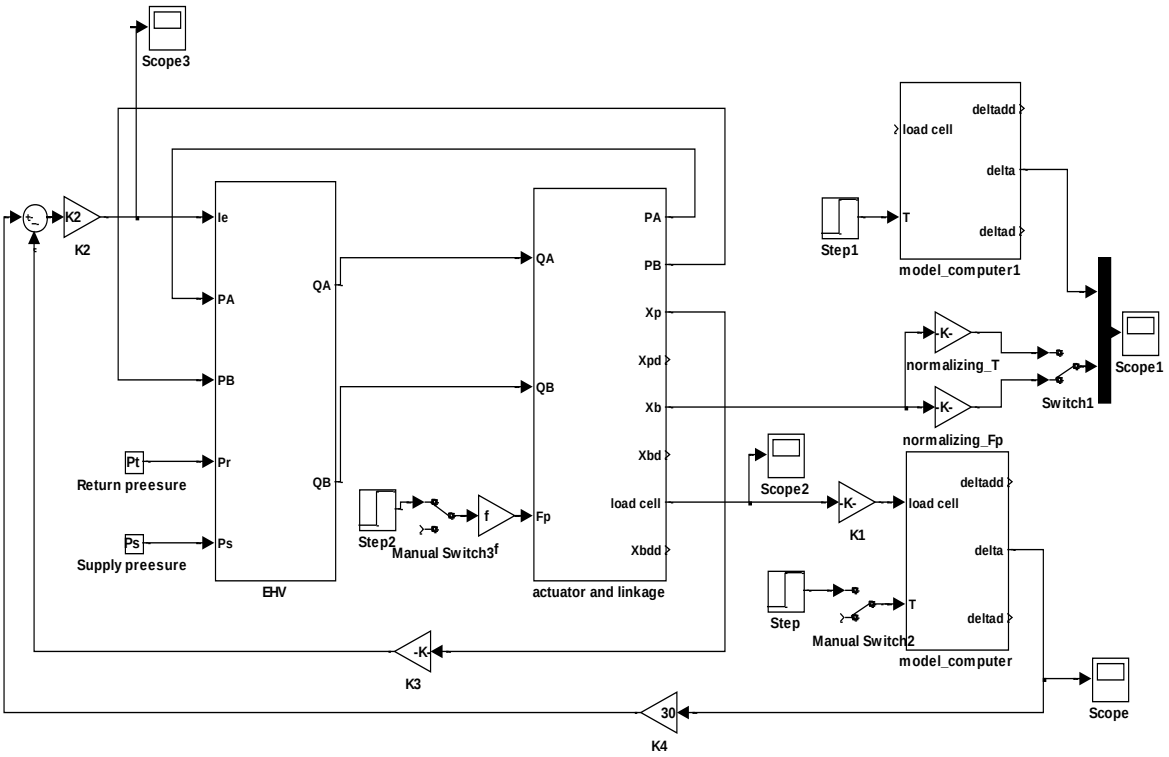

Fig.46 Position inner loop control loading structure.

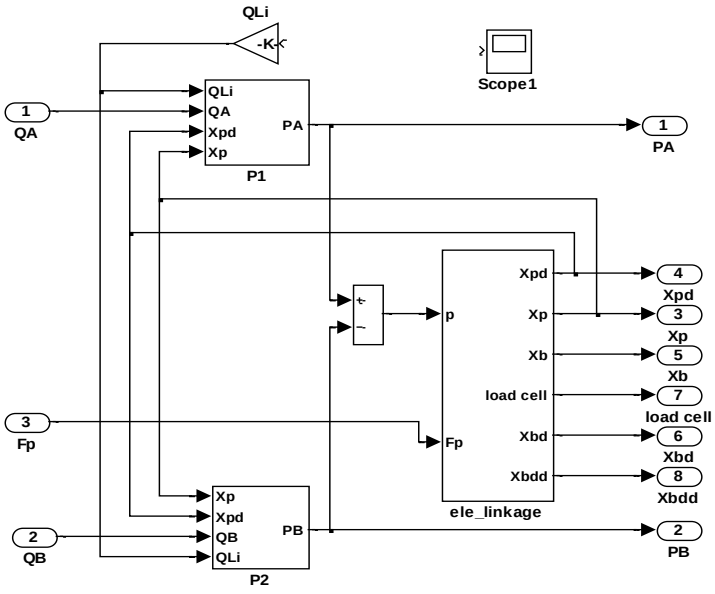

Fig.47 Actuator and linkage.

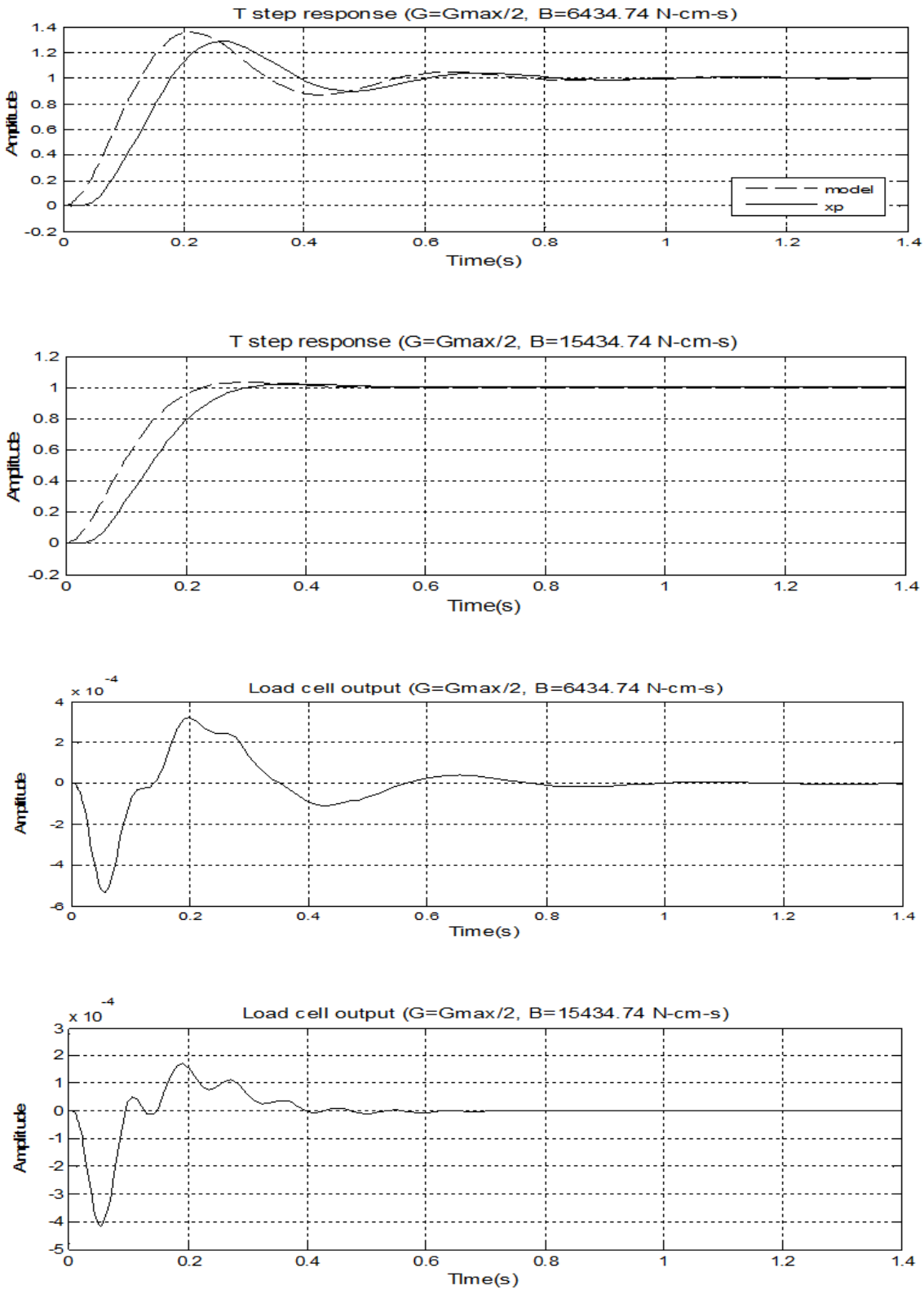

Fig.48 Position follower trim force step responses.

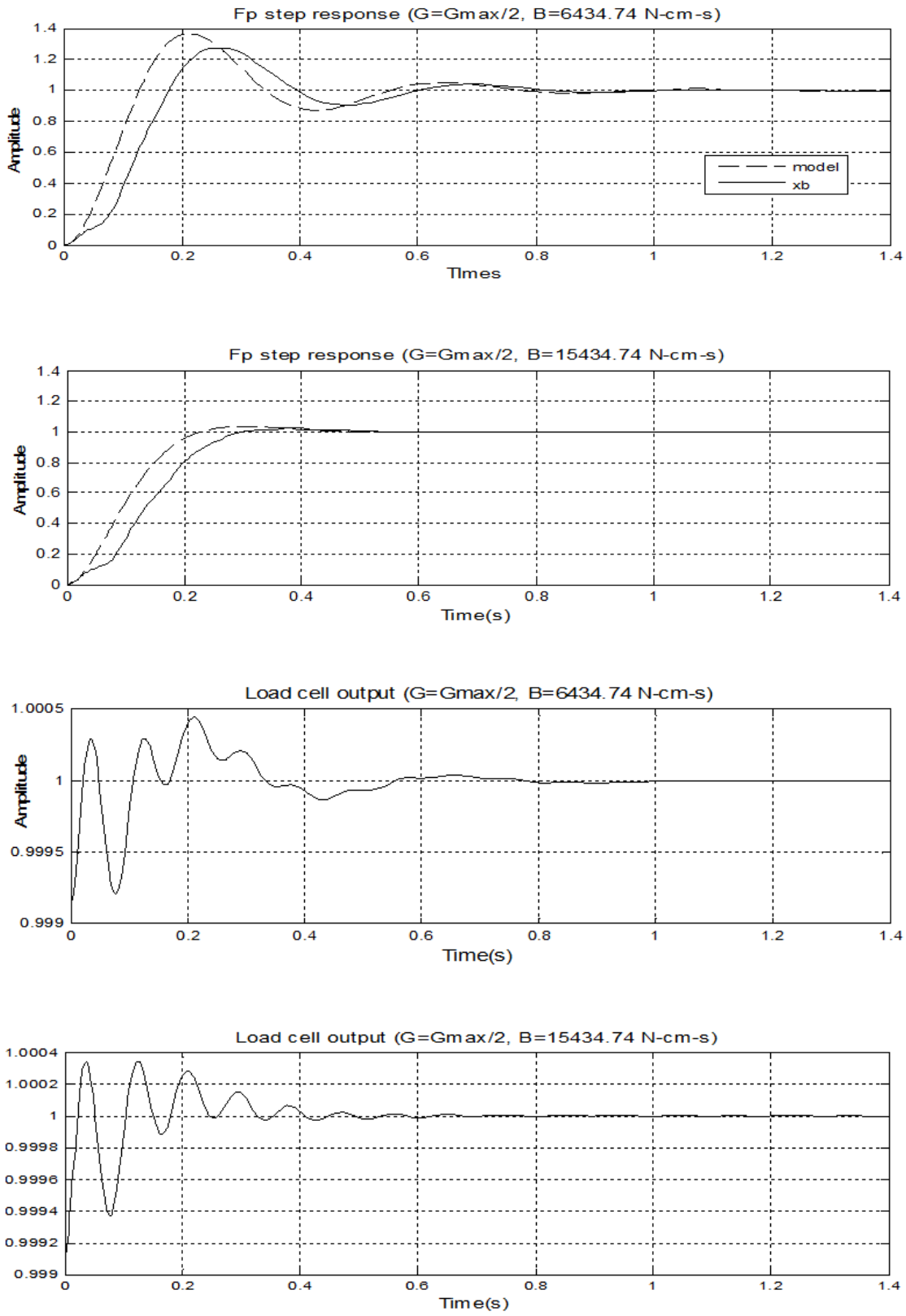

Fig.49 Position follower pilot force step responses.

10.9.2 Velocity follower

For getting FAA level D approval, control loading requires higher precision of replica of aircraft dynamics. The time tolerance at the zero cross point must be under 0.1 seconds to fulfill the requirement. A better model following control scheme is thus needed. Velocity control originates from the fact that the actuation of EHV and the cylinder is to transfer velocity (flow rate) to position (cylinder extension). Intuitively, following speed is faster than flowing position. In the following velocity control structure **Fig.50**, the EHV is driven by the model speed $\dot{\delta}$, which is also combined with the position deference ($\delta - x_p$) and velocity deference ($\dot{\delta} - \dot{x_p}$).

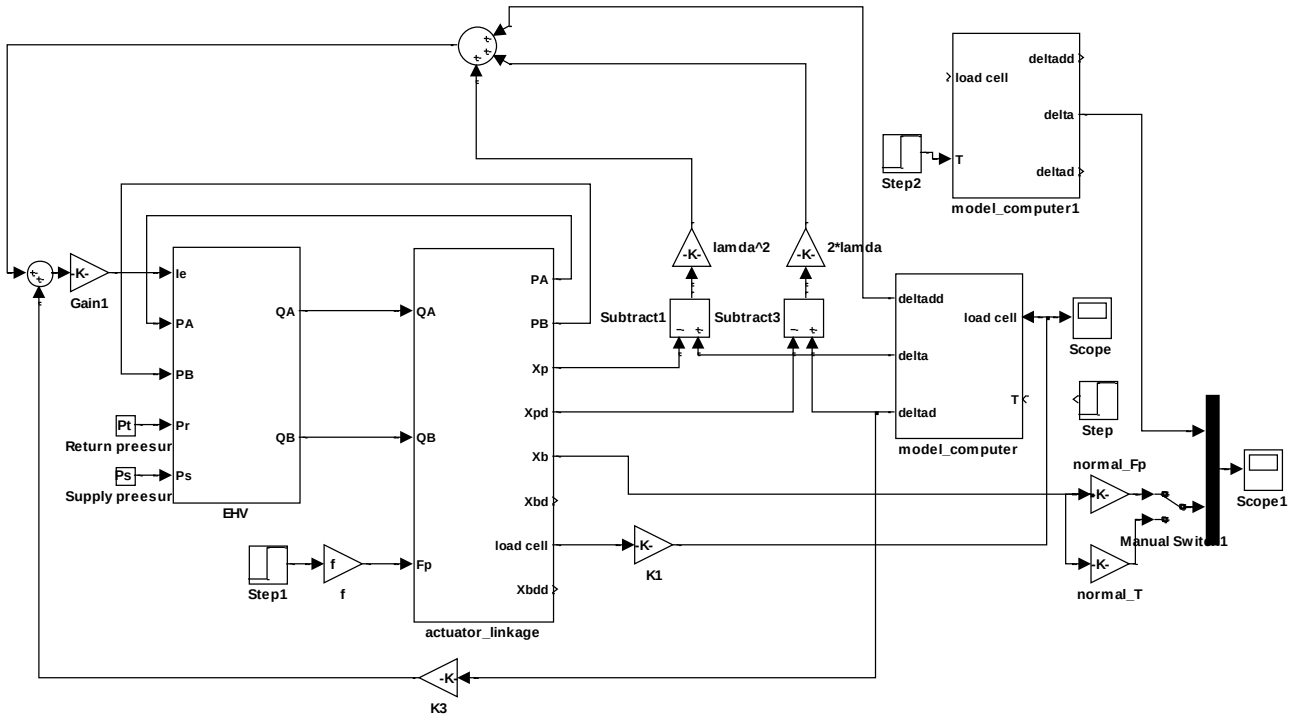

Fig.50 Velocity inner loop control loading structure.

Figs.51 and **52** illustrate the results of the velocity follower. It can be clearly seen that the phase delay problem has been solved, and the model following result is close to perfect. However, tuning of the controller is more time consuming than tuning the position follower, but still under an accepted level. For both the position follower and the velocity follower, the typical outputs of the load cell have same characteristic patterns corresponding to free response and pilot control response. The patterns are very similar with the ones observed in the simulator, which proves that the modelling of the load cell is correct.

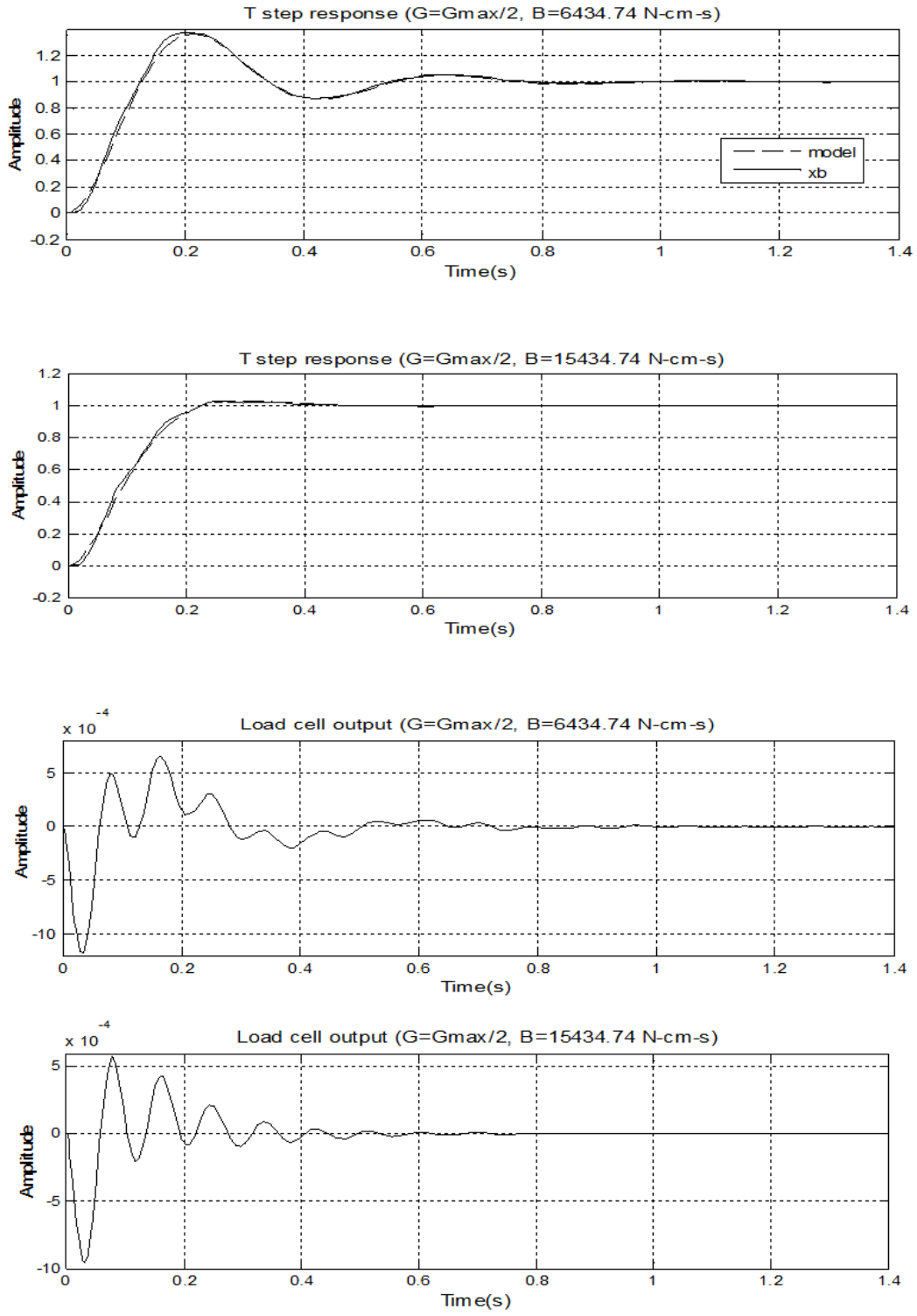

Fig.51 Velocity follower trim force step responses.

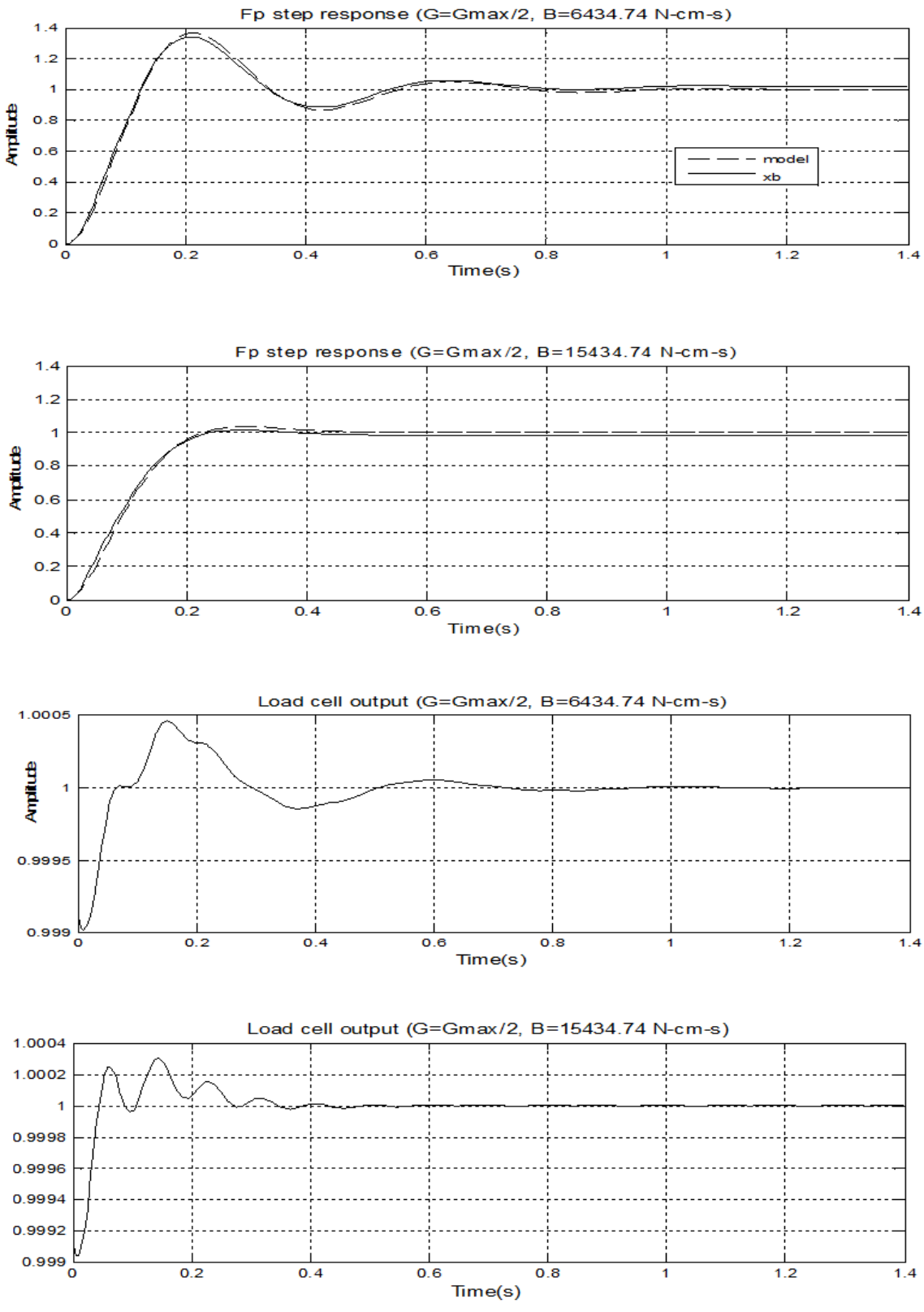

Fig.52 Velocity follower pilot force step responses.

10.10 Digital control loading system

Digital control loading systems merged in the middle of 1980s. It is superior to the old version of analog control loading systems in terms of re-configurability, maintainability and long-term stability. Because more non-linear characteristics can be reproduced cost-effectively within digital control loading systems, the fidelity is improved dramatically. A more detailed discussion about advantages of digital over analog systems can be found in reference [34]. A published example of digital C/L follows here.

Digital control loading systems still use the fundamental structure introduced in the previous sections. However a separation of forward and after mass can be found in the schematic in **Fig.53**.

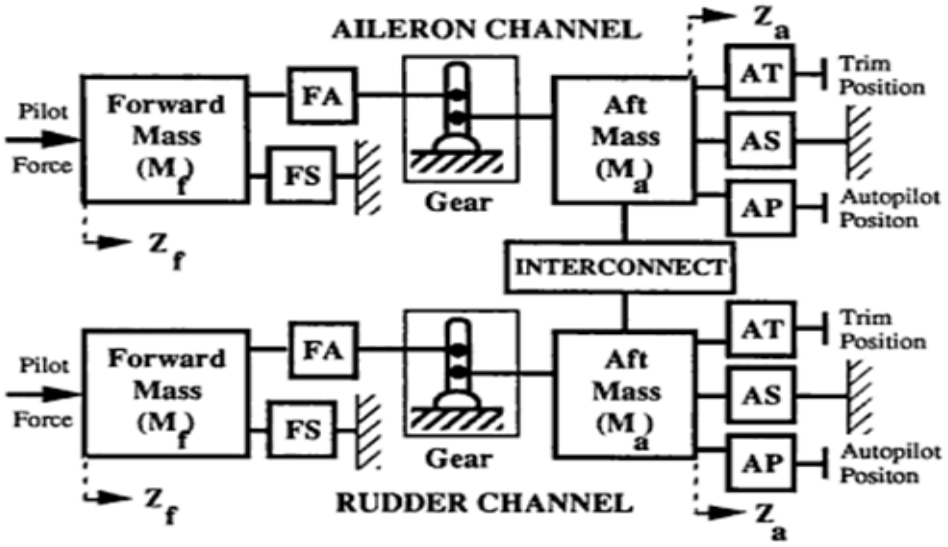

Fig.53 Model schematic [29].

The forward mass represents control (wheel, pedal) and the aft mass represents the surface (aileron, rudder). Non-linear forces (**Fig.54**) can be attached to these two masses at six different places, represented by the blocks FA, FS, AT, AS, AP and INTERCONNECT. The separation of forward mass and after mass is necessary because these two parts run at different iteration rates. The forward mass model runs at a real time iteration rate up to 2 KHz that is required to reproduce a real time control handling feeling. The after mass model runs a lower iteration rate that is close to the host software module iteration rate.

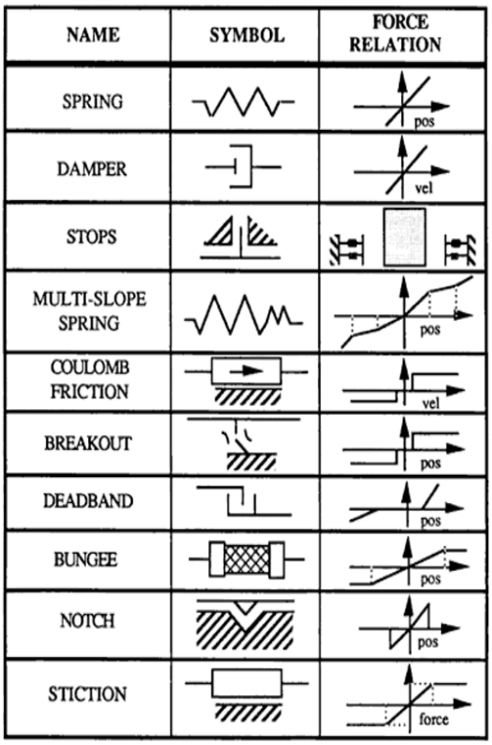

Fig.54 Topical force components [29].

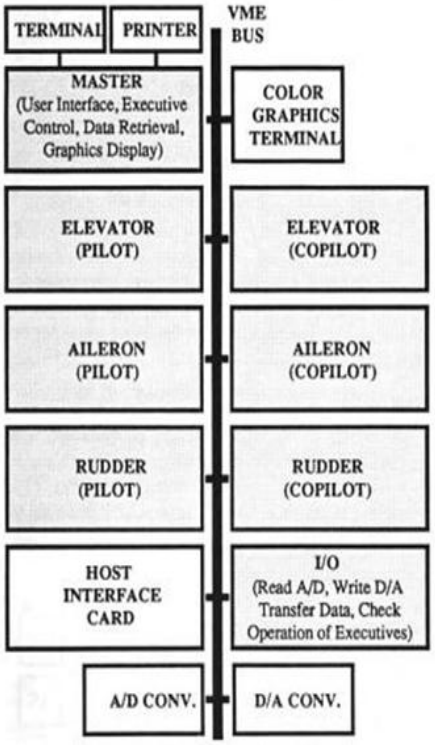

Fig.55 Hardware block diagram [29].

Fig.55 is a block diagram of the hardware of the digital control loading work station that is presented as an example [29]. As can be seen from this figure, there is one slave processor card for each channel. Each slave processor card is running a control loading executive, with associated model and servo routine. The executive is a computer program which controls the orderly operation of different routines running at respective iteration rates.

The workstation has control analysis and design routines. DIGITAL is an interactive design package for linear systems; and NSP is for nonlinear systems.

The session controller runs the workstation [29]:

1. Create model structure/Enter servo parameters
2. Read in parameters from disk file/Save parameters to disk file
3. Load programs/Start or stop executives
4. Display variable time histories
5. Change or display parameters in real time
6. Spectrum analysis

Servo (**Fig.56**) is the core part of a control loading channel. As indicated in the diagram, it is a model following control system: the mechanical actuation follows the forward model of a control channel, exactly tracking the position, velocity, acceleration, and force of the model.

Note that there is only one integrator inside the dash line block; this is because velocity, instead of position, is used to drive the valve. The velocity control loop can be presented as a first order system [5]. This simplification is valid as the electric hydraulic valve has a wide bandwidth. Notice that acceleration (force) is also fed to drive the valve to simulate a crisp feeling of mechanical stop. In this case, one more integrator needs to be added in the cylinder loop, due to the fact that the force loop is a second order loop.

A compensation block filters the oscillation signal of the load cell; as discussed in the previous session, the oscillation comes from the compliance of mechanical linkage. Ideally, if all the COMPs are set correctly, the oscillation can be cancelled out.

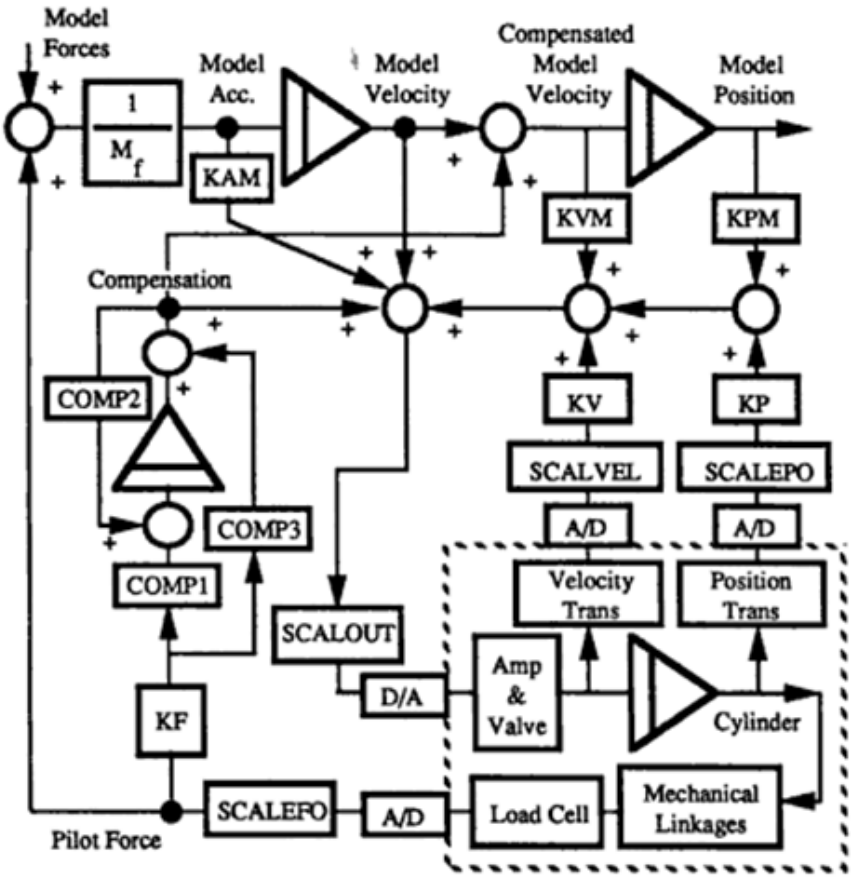

Fig.56 Servo [29].

The overall design and tuning process of the cited digital control loading system is given below [29]

1. Use aircraft data and flight test data (on ground statics and control fell dynamic curves) to determine approximate model parameters.
2. Use the spectrum analysis module of the session controller program to obtain a model for the simulator linkages.
3. Use the DIGITAL program to obtain root locus plots for each model and servo parameter to be adjusted.
4. Attempt to position model poles so as to obtain the correct control dynamic response.
5. Attempt to position mechanical linkage poles so that the response damps out quickly.
6. When the model and servo parameters have been chosen to meet points 4 and 5 above, use the DIGITAL program to simulate the system response. If the response is not satisfactory, go back to the root locus diagrams and adjust the parameters to improve the response.

11: Electrical control loading and motion

There is always room for improvement. In 2006, the world's first electrical motion and control loading full-flight simulator was honoured with a Level D certificate by FAA. While it fully met the performance specifications, the advantages that electrical motion and control loading bring to the pilot training industry are [35]

- Higher energy efficiency of up to 80% over the hydraulic counterpart. This is because electrical systems do not need to maintain a high hydraulic pressure source.
- Higher uptime from maintenance. Maintenance of hydraulic system is tedious and both labour and materials are costly compared to that of electric systems.
- Less-costly infrastructure, because there is no need to build a hydraulic pressure supply room and hydraulic hoses ditches.
- More environmentally friendly, due to the lack of hydraulic fluid leak, and the lack of noise generated from hydraulic pressure pump.

Just like any technical innovation, the development of electrical motion and control loading faced challenges. For motion systems, the plant (simulator platform) has a very high payload, which was never a problem for hydraulic cylinders due to their big power factor; and there is a safety issue when electricity power is interrupted, which wasn't a problem for hydraulic system because the pressure reserved in hydraulic accumulators could bring the simulator back to its 'parking' position. For control loading, there were concerns about the residual torques of the motor, which might be felt around the control center position.

Inspired by industry demand initiative, engineers have resolved those challenges. With the help of advances in processing technology and high-power devices techniques, high-power servo-drives have been developed; high-energy magnets have boosted power density in brushless motors; ball-screw technology devices have been used to translate rotation into linear movement; and a special cushion has been designed to prevent the actuators from damaging the end stop [35]. All the efforts make up the most important component—electric actuators. For control loading, model-follower force-loop technology has been implemented. Linear electric actuators that are used for primary control are equipped with position feedback encoders [36].

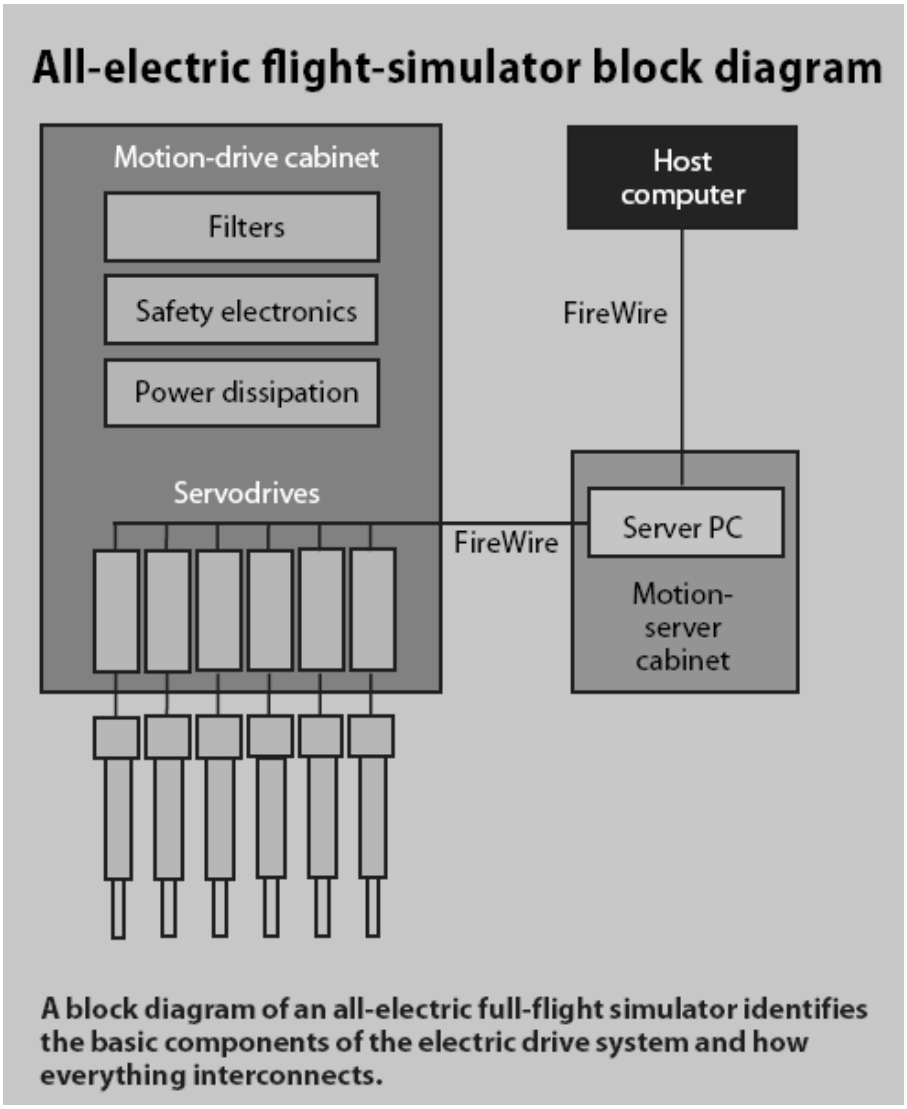

Fig.57 All-electric flight simulator block diagram [35].

12: Conclusion

A generic approach is proposed to study the aircraft motion and control loading simulation with a particular focus on simulation algorithms and control scheme implementations. This approach has greatly improved the understanding of this subject.

As the core part of this project, the symbolic modelling of control loading channels by Simulink is effective and validated. In industry practice, control loading model tuning and control parameter tuning are tedious and time-consuming tasks. One reason for this is the uncertainty of output of the load cell. Ideally, the output of the load cell is the pilot input force. But in reality, as can be observed in flight simulators, there are unwanted rings or oscillating "noise" existing with pilot force output. The load cell outputs modelling simulation results (**Figs.51** and **52**) are similar to the ones observed in simulators. The analytical correctness comes from the detailed model of EHV/actuator, the consideration of linkage compliance, and the correct mathematical modelling of the load cell. To the author's knowledge, this particular mathematical modelling had never been presented in any of the referenced works of this thesis. The significance of the model is that a filtering method can be developed based on the analytical result of load cell; eventually a perfect matching between model and actuation can be achieved cost-effectively by filtering unwanted signals.

Reviewing the history of aircraft motion and control simulation: from simplest man-power to hydraulic power and on to electrical power; from analog model/servo to digital model/servo; from position-loop to velocity loop and to force-loop, the fulfilling of industry demands with available resources takes priority than the pursuing of technical performance. The construction and control parameter tuning of the different model followers during this research revealed the design of control simulation is an iterative and optimizing process, and is a trade-off between the control performance, cost, maintainability, and the ease of tuning. The researches of this thesis provide an effective means and platform for further design optimization, system reliability, and prognostic analyses.

The accuracy of the motion simulation algorithm is dependent on the accuracy of the theory of motion cue perception mechanisms of human beings. It can be speculated that the next generation of motion simulation will benefit from the latest psychophysical research results of human sensory mechanisms about visual, motion and tactile cues. For control dynamic simulation, the MRAC (model-reference adaptive control) technique theoretically can reach perfect model following. However the bottle-neck is to sense all the required feedback signals accurately, especially force or acceleration, using cost-efficient methods. The motion and control loading models presented in this thesis also can be utilized for the

research of next generation motion simulation, for designing control observers, and for testing different position transducers.

References

[1] H. Schlichting, *Boundary-Layer Theory, 7th Ed.* Mcgraw-Hill, 1979, p. 1.

[2] R. C. A'Harrah, *Flight Simulation, Past, Present, and Future,* AIAA Paper No. 65-480, AIAA Second Annual Meeting, San Francisco, CA, 1965, pp. 371-386.

[3] J. M. Rolfe, K. J. Staples, *Flight Simulation,* Cambridge, London, 1986, pp.79, 86, 111-122.

[4]Moog Inc., *Moog 760 Series Servovalves*, Moog Inc., 2007, pp. 2-4.

[5] N. D. Manring, *Hydraulic Control Systems,* John Wiley & Sons, Inc., 2005, Chapter 7.

[6] M. G. Rabie, *Fluid Power Engineering*, Mcgraw-Hill, 2009, Chapter 10.

[7] M. Kalyoncu, M. Haydim, "Mathematical Modelling and fuzzy logic based position control of an electrohydraulic servosystem with internal leakage," *Mechatronics,* 19, 2009, pp. 847-858.

[8] R. Poley, *DSP Control of Electro-Hydraulic Servo Actuators,* Texas Instruments Application Report, 2005.

[9] D. Allerton, *Principles of Flight Simulation,* John Wiley & Sons, Inc. 2009, p. 429.

[10] H. E. Merritt, *Hydraulic Control Systems,* Wiley, 1967, pp. 39-43.

[11] Moog Inc.. *Electrohydraulic Valve, A Technical Look*. Retrieved March 8, 2010, from http://www.moog.com/literature/ICD/Valves-Introduction.pdf

[12] B. Etkin, *Dynamics of Flight, Stability and Control*, John Wiley & Sons, 1996, Chapter 4, 7.

[13] Wikipedia, *Pictures*, Retrieved March 8, 2010, from http://en.wikipedia.org/wiki/Flight_simulator

[14] Wikipedia, *Acceleration onset cueing*, Retrieved July 8, 2010, from http://en.wikipedia.org/wiki/Acceleration_onset_cueing

[15] C. C. Clark, *Human control performance and tolerance under severe complex wave form vibration and review of flight simulation, with a preliminary historic review of flight simulation,* Accession No. 62N14482, NASA 1962, pp. 176-194.

[16] L. D. Reid, M. A. Nahon, "Response of airline pilots to variations in flight simulator motion algorithms,"*Journal of Aircraft,* 25 (7), 1988, pp. 639–646.

[17] R. J. A. W. Hosman, J. C. van der Vaart, *Thresholds of Motion Perception and Parameters of Vestibular Models Obtained from Test in a Motion simulator, Effects of Vestibular and Motion Perception on Task Performance,* Memorandum M-372. Delft, Technische Hogeschool Delft, 1980.

[18] J. L. Meiry, *The Vestibular System and Human Dynamic Space Orientation,* Report No. NASA-CR-122692,T-65-1, NASA, 1966.

[19] C. C. Ormsby, *Model of Human Dynamic Orientation,* Report No. NASA-CR-132537, NASA, 1974.

[20] D. Stewart, "A platform with six-degree-of-freedom," *Proceedings in the Institution of mechanical Engineers,* 180, 1(5), 1965, pp.371-386.

[21] M. A. Nahon, L. D. Reid, "Adaptive Simulator Motion Software with Supervisory Control," *Journal of Guidance, Control, and Dynamics,* 15(2), 1992, pp. 376-383.

[22] M. A. Nahon, L. *D. Reid, "*Simulator Motion-drive Algorithms: A designer's Perspective*," Journal of Guidance, Control, and Dynamics,* 13(2), 1990, pp. 356-362.

[23] S. K. Advani, M. A. Nahon, N. Haeck, J. Albronda, "Optimization of Six-Degrees-of-Freedom Motion Systems for Flight Simulators," *Journal of Aircraft*, 36(5), 1997, pp. 819-826.

[24] M. Idan, D. Sahar, *Robust controller for a dynamic six degree of freedom flight simulator,* AIAA Flight Simulation Technologies Conference, San Diego, CA, July 1996.

[25] P. R. Grant, S. K. Advani, An *Iterative Learning Control Algorithm for Simulator Motion System Control,* AIAA Modeling and Simulation Technologies Conference and Exhibit, Hilton Head, SC, August 2007.

[26] J. Roskam, *Airplane Flight Dynamics and Automatic Flight Controls*, Roskam Aviation and Engineering Corporation, 1979, pp. 300-305.

[27] Jeppesen Sanderson, Inc., *Airframes and Systems,* Jeppesen, Sanderson, Inc., 2005, p. (5)33.

[28] D. P. Coiro, A. De Marco, F. Nicolosi, *A 6DOF Flight Simulation Environment for General Aviation Aircraft with Control Loading Reproduction,* AIAA Modeling and Simulation Technologies Conference and Exhibit, Hilton Head, SC, August 2007.

[29] M. T. Hagan, J. O. Hamalainen, N. M. Sammur, G. Guimaraes, C. D. Latino, "Digital control loading and motion for flight simulation," *Progress in simulation,* Volume 2, edited by G. W. Zobrist, J. V. Leonard, 1994, pp. 52-87.

[30] P. R. Johansen, R. E. Bardusc, *Analysis and compensation of an aircraft simulator control loading system with compliant linkage,* NASA TN D-7747, 1974.

[31] R. V. P., Billy R. Asbworth, *The effect odd digital computing on the performance of a closed-loop control-loading system,* NASA TN D-8371, 1976.

[32] A. Gerretsen, M. Mulder, M.M. van Paassen, *Comparison of position-loop, velocity-loop and force-loop based control loading architectures,* AIAA Modeling and Simulation Technologies Conference and Exhibit, San Francisco, CA, August 2005.

[33] National Simulator Program, *14 CFR Part 60 NSP Consolidated Version,* Retrieved March8, 2010, from http://www.faa.gov/about/initiatives/nsp/media/consolidated_version.pdf

[34] J. Cooper, M. Rutherford, and M. McKinnon, "Digital control loading and motion—the final word?" *ICAO Bulletin,* May 1986, pp. 30-33.

[35] S. Murthy, *Electrifying the feel of flight,* Penton Media, Inc., 2009.

[36] Moog Inc., *Control loading solution,* Moog Inc., 2009.

Appendix A, Simulink blocks

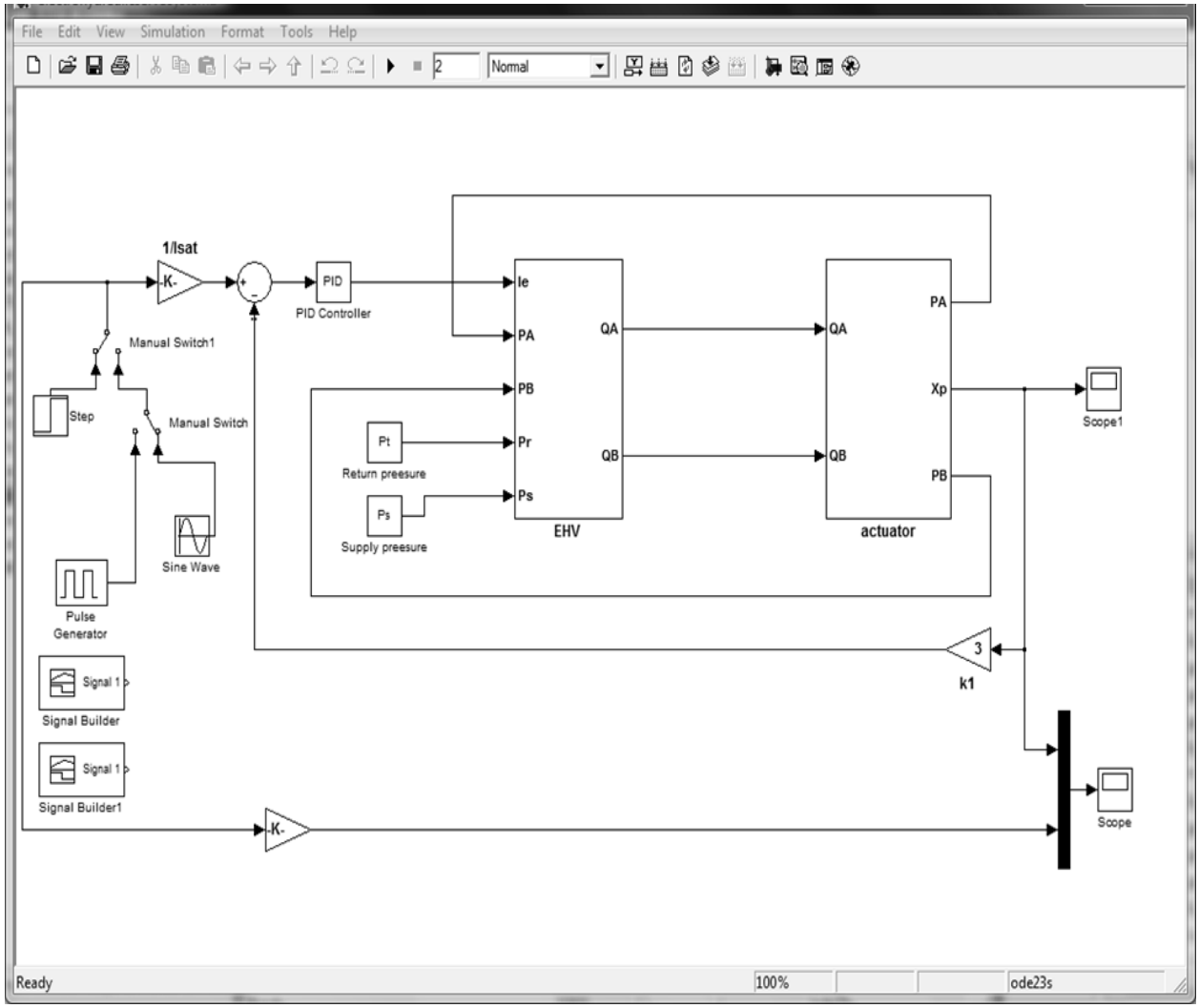

Top level system diagram

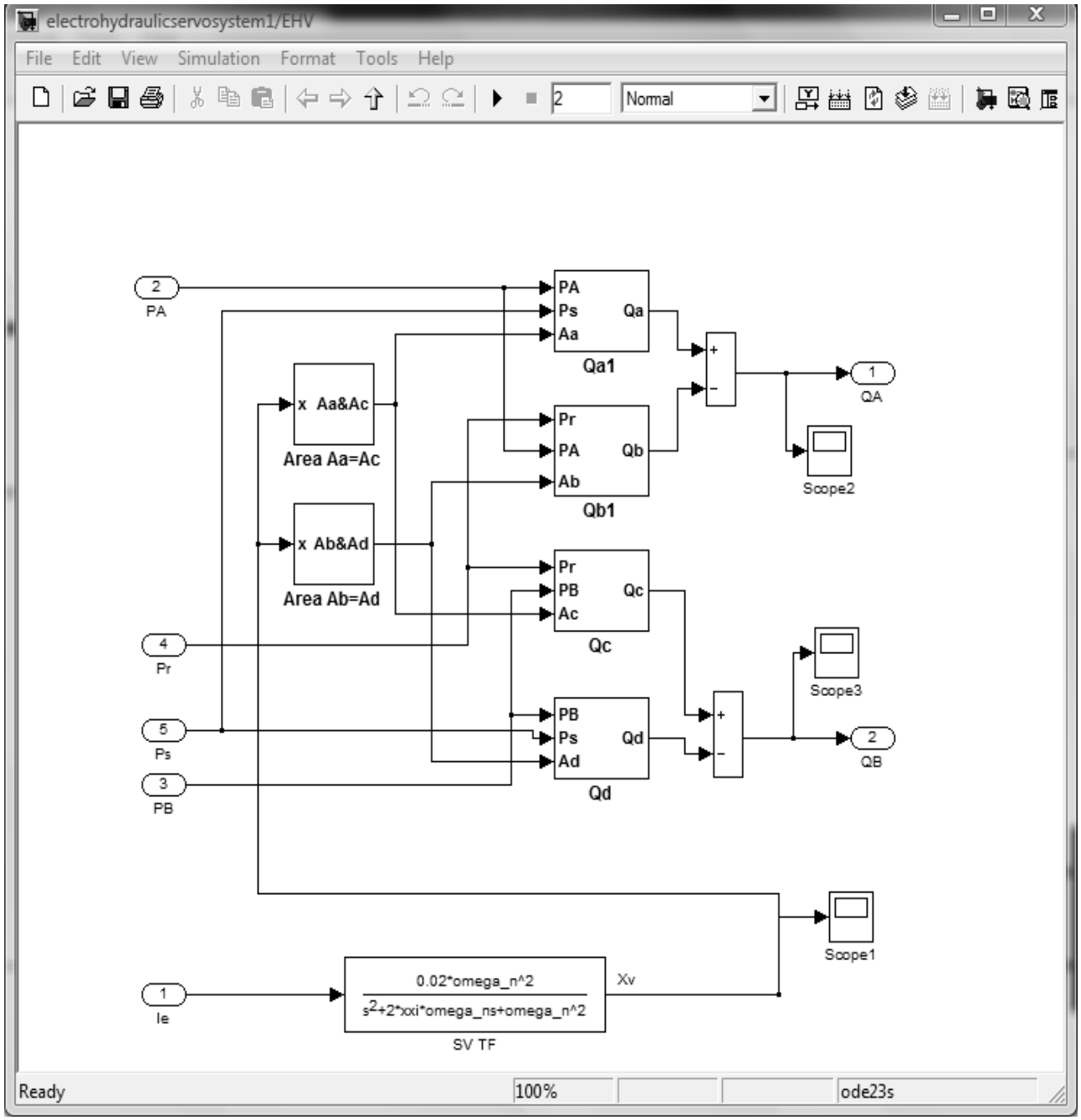
electrohydraulicservosystem1/EHV
File Edit View Simulation Format Tools Help
Normal
2
PA
PA
Ps
Aa
Qa
Qa1
x Aa&Ac
Area Aa=Ac
Pr
PA
Ab
Qb
Qb1
1
QA
Scope2
x Ab&Ad
Area Ab=Ad
Pr
PB
Ac
Qc
Qc
4
Pr
Scope3
5
Ps
PB
Ps
Ad
Qd
Qd
2
QB
3
PB
Scope1
1
Ie
0.02*omega_n^2
s2+2*xxi*omega_ns+omega_n^2
SV TF
Xv
Ready
100%
ode23s

EHV

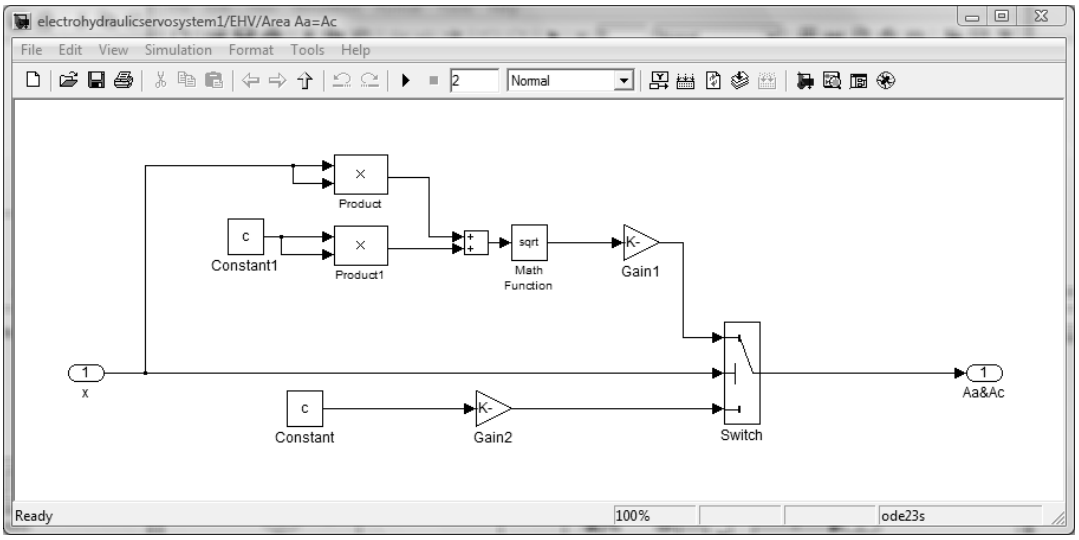

Restriction area

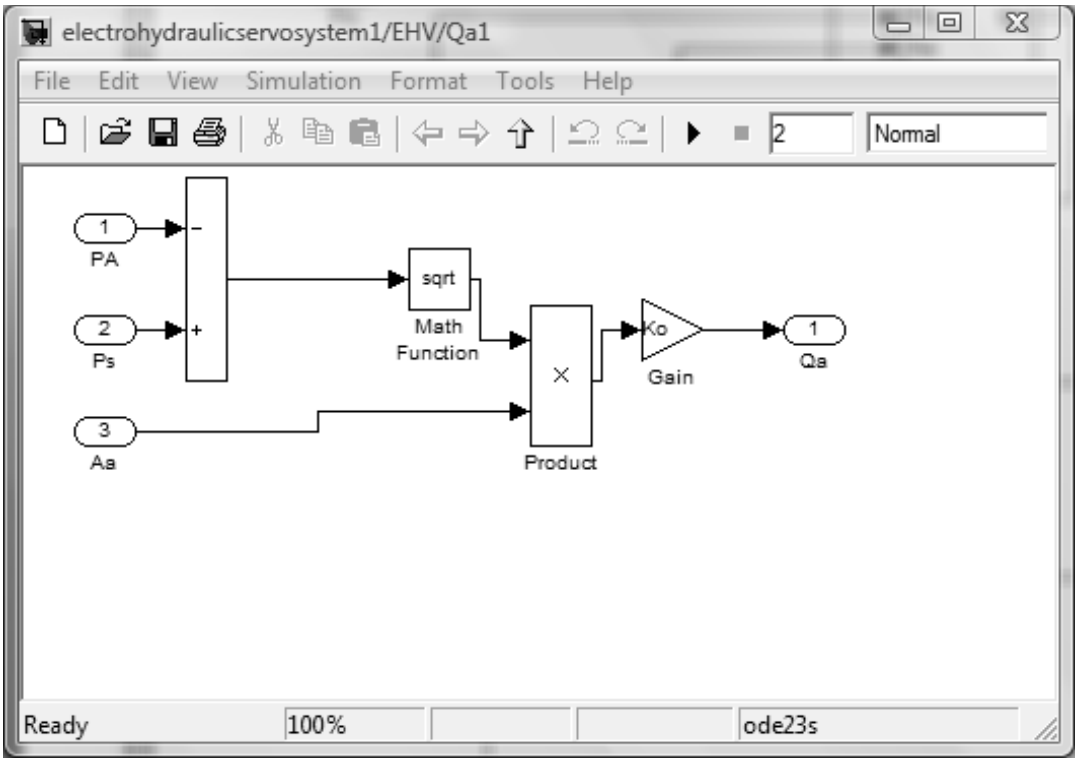

Flow

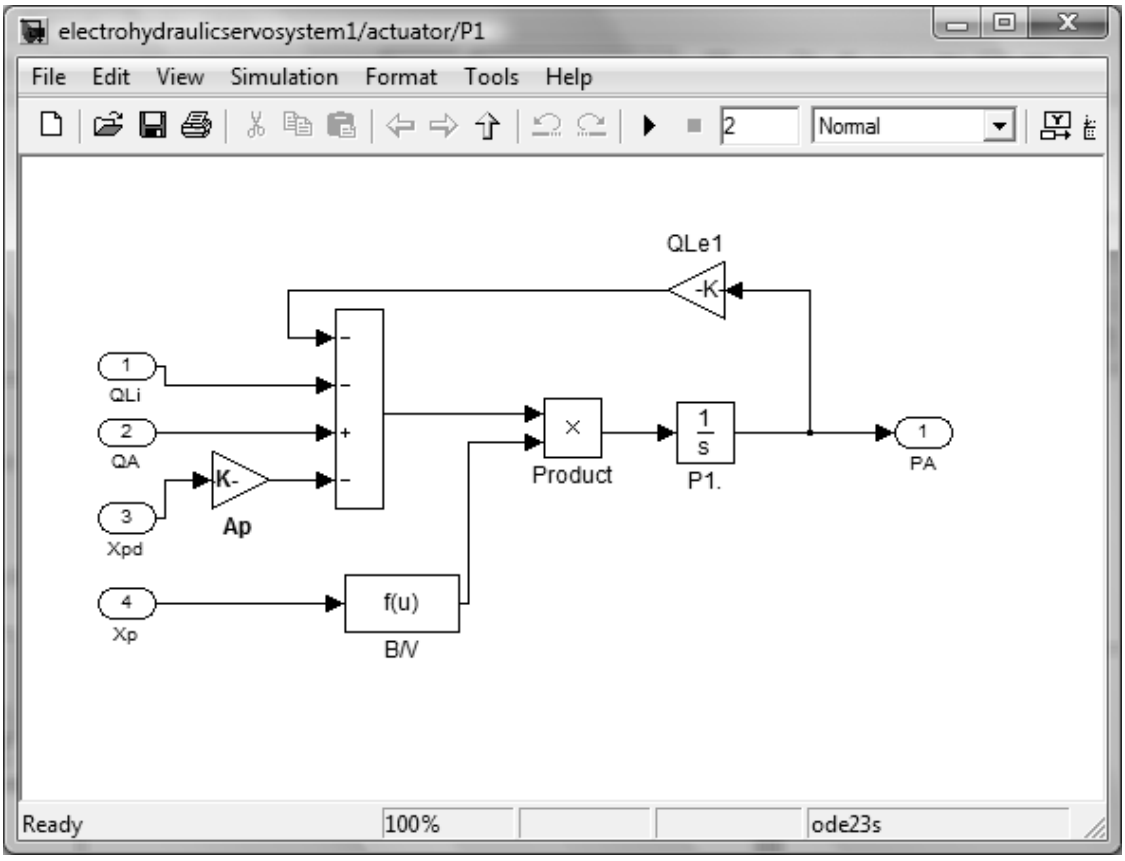
electrohydraulicservosystem1/actuator/P1
File Edit View Simulation Format Tools Help
2
Normal
QLe1
-K
1
QLi
2
QA
3
Xpd
K-
Ap
4
Xp
f(u)
B/V
Product
1
s
P1.
1
PA
Ready
100%
ode23s

Pressure

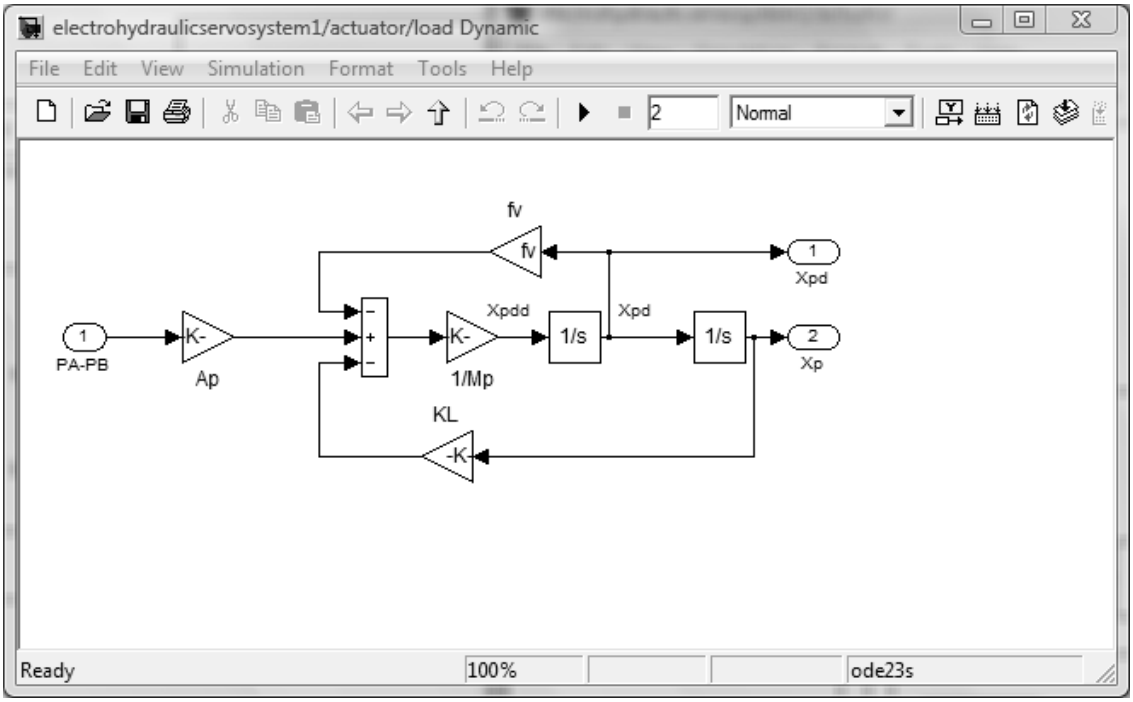
electrohydraulicservosystem1/actuator/load Dynamic
File Edit View Simulation Format Tools Help
2
Normal
fv
fv
1
Xpd
1
PA-PB
K-
Ap
Xpdd
K-
1/Mp
1/s
Xpd
1/s
2
Xp
KL
-K
Ready
100%
ode23s

Piston and load dynamic

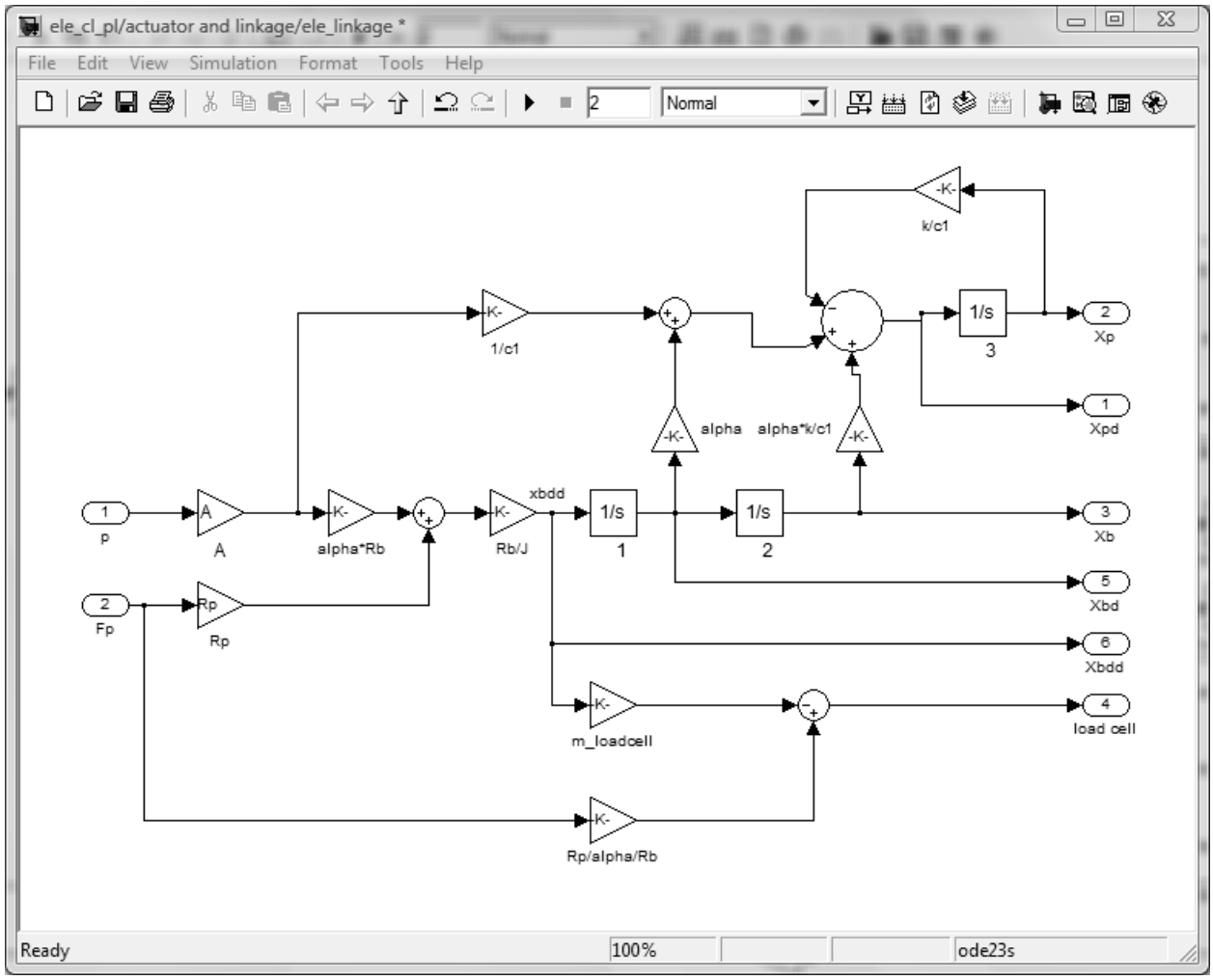

Elevator linkage and load cell

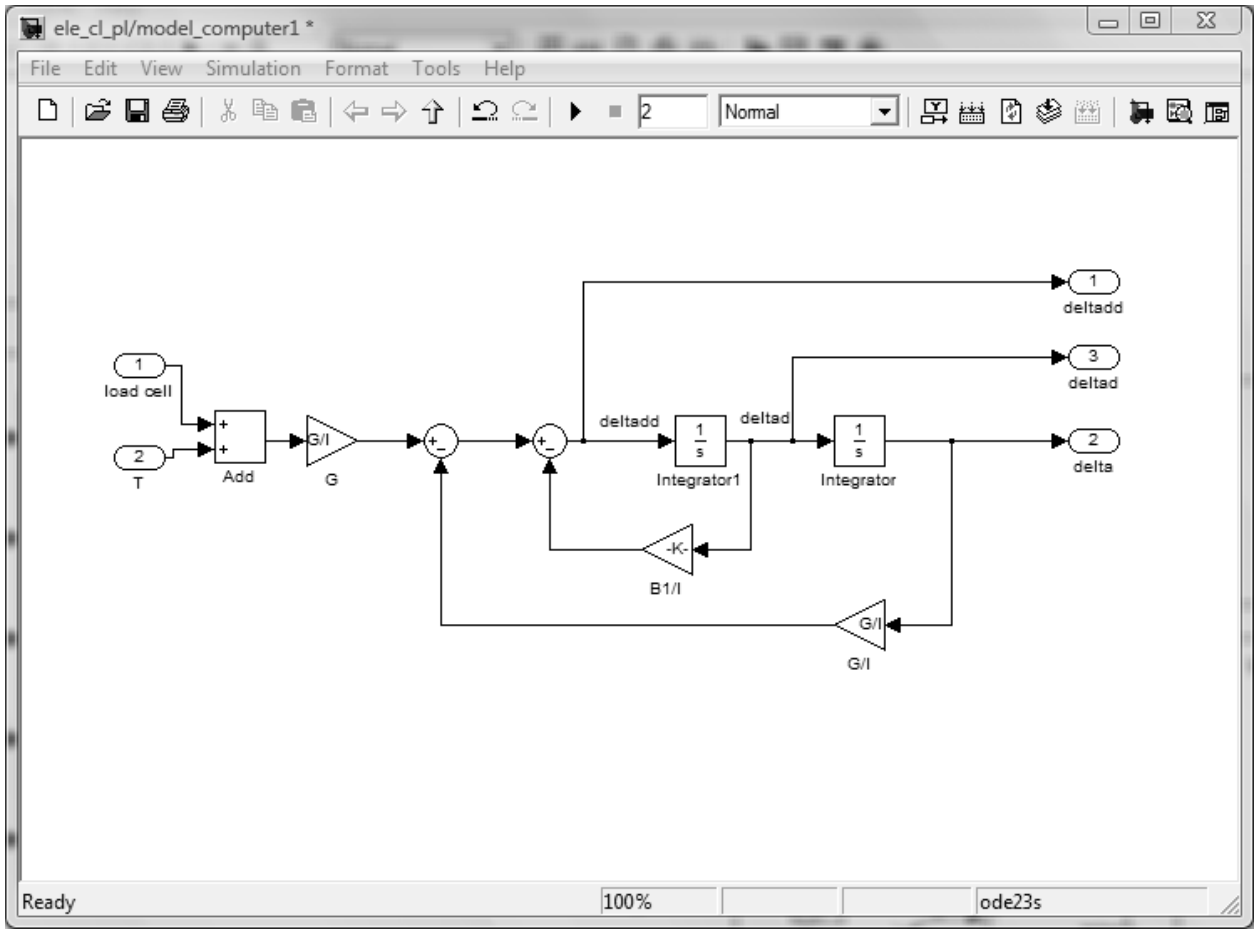

Control model

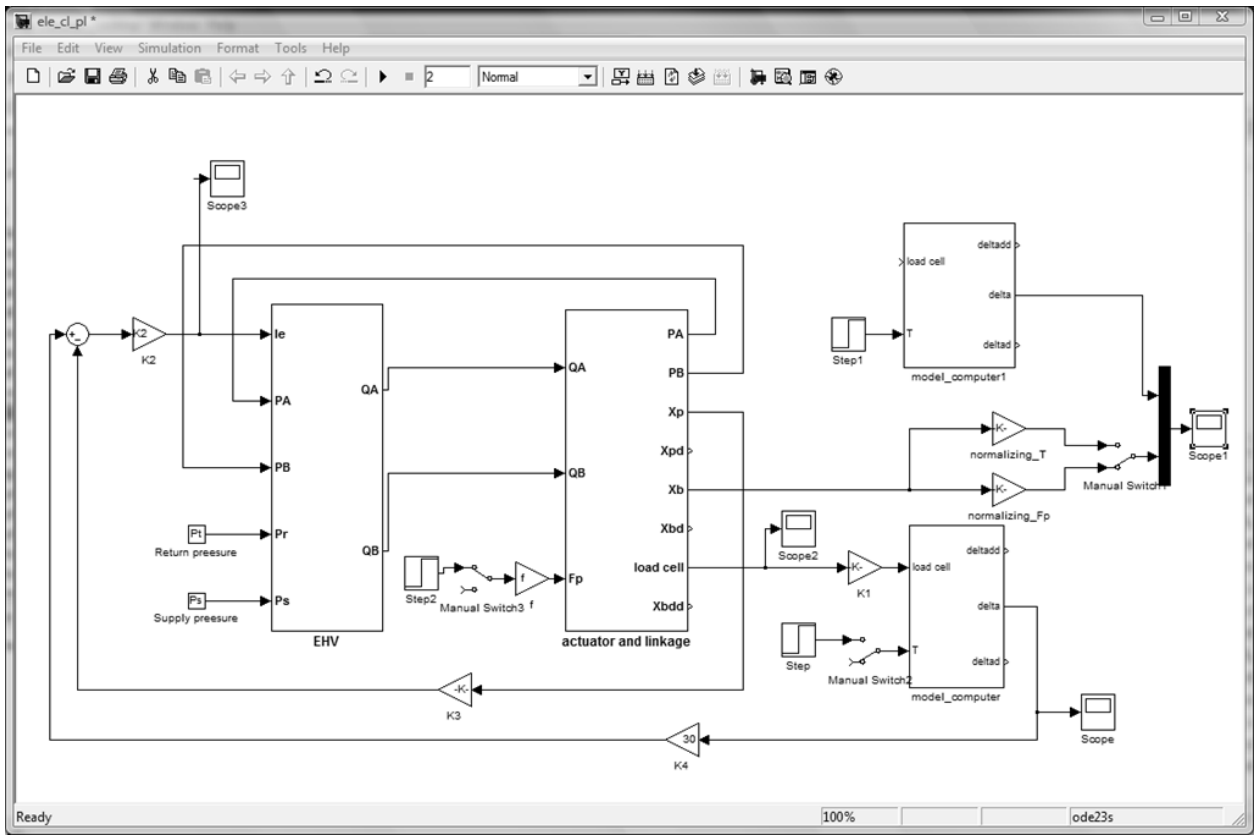

Elevator control loading—position follower

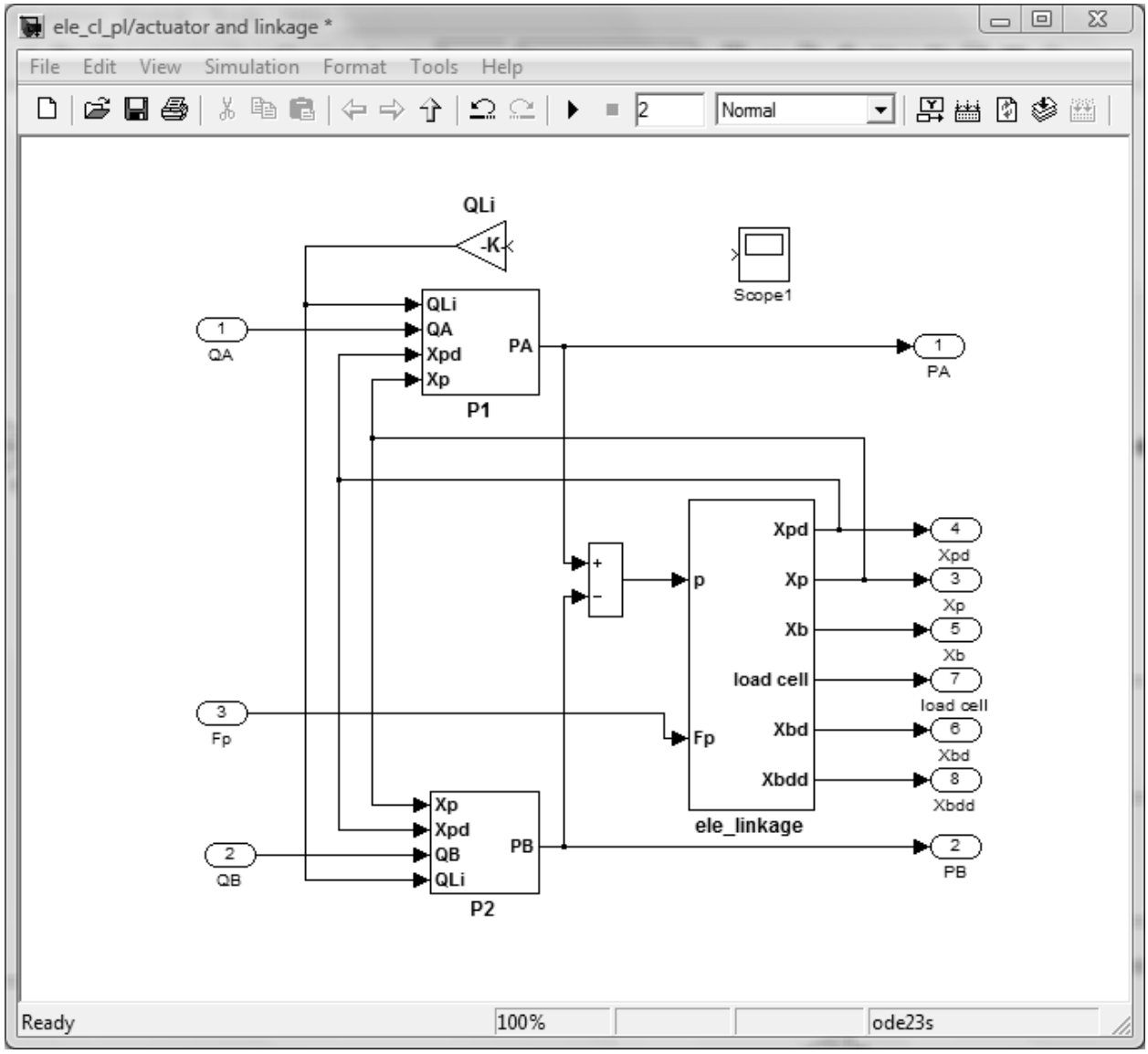

Actuator and linkage

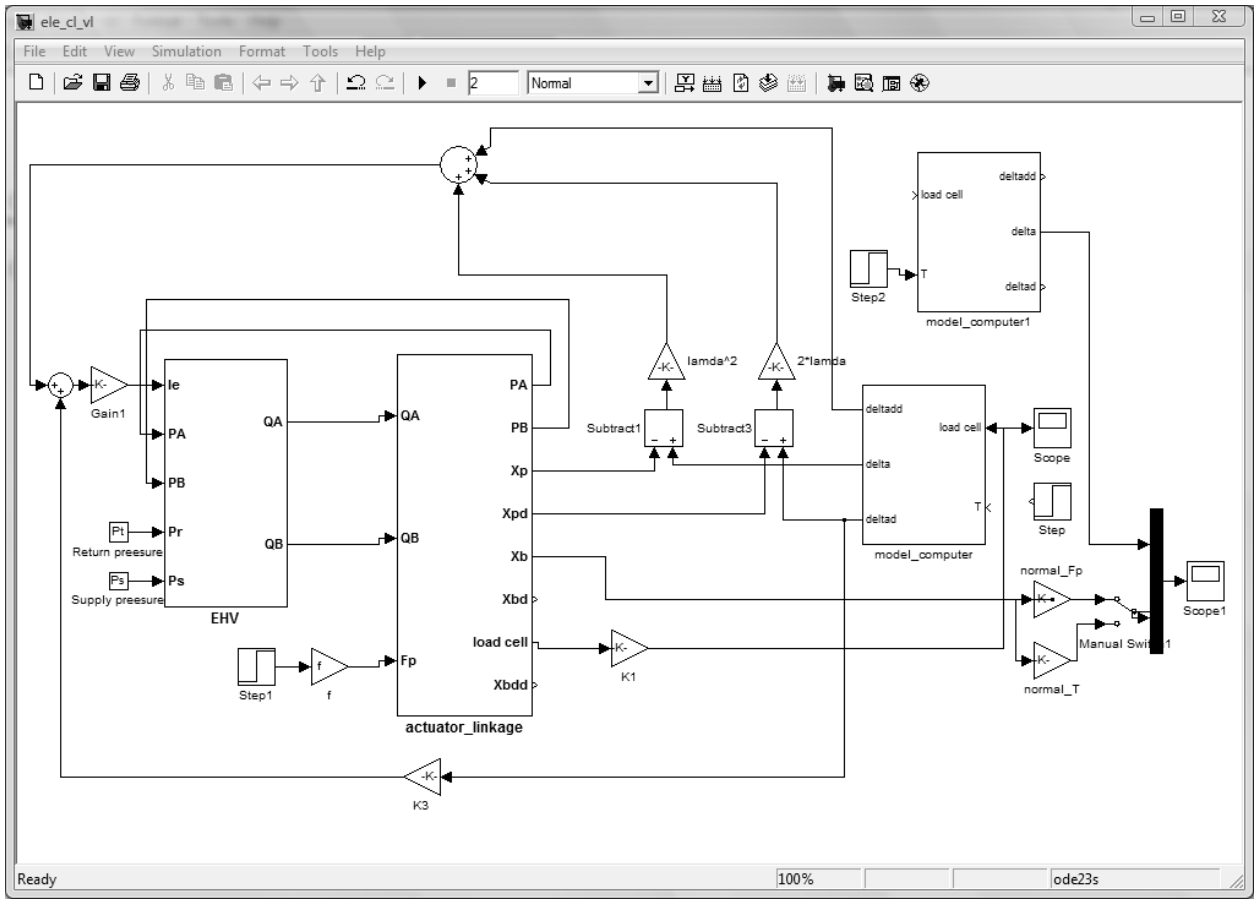

Elevator control loading—velocity follower

Appendix B, MATLAB Code

```
%%%%%%%%%%%%%%%%%%%%%%%%%%
%EHV Actuator and Control parameters%
%%%%%%%%%%%%%%%%%%%%%%%%%%
%Part A
% Oil density Ro (kg/Cum)
Ro=867
% Cd*(2/Ro)^0.5
Cdro=0.611*(2/Ro)^0.5
% Initial volume of oil in spool side chamber Vo (Cu m)
Vo=32.25e-6
% Bulk modulus os oil B (Pa)
B=1.5e9
% Supply Pressure Ps (Pa)
Ps=2e7
% Return Pressure Pt (Pa)
Pt=0
% Spool port width Omiga Omiga (m)
Omiga=0.002
% Spool radial clearance c (m)
c=1e-6
% Piston area Ap (Sq m)
Ap=645e-6
% Resistance to internal leakage
Ri=1e20
% Resistance to external leakage
Re=1e20
% Piston and load mass (kg)
Mp=9
% Friction coefficient on piston
fv=2000
% Piston loading coefficient Ky
Ky=0
%servovalve damping ratio
xxi=0.48
%rad/s, servovalve natural frequency
omega_n=534
%H, servovalve coil inductance
Lc=0.59
%Ohm, servovalve coil resistance
Rc=100
%A, servovalve coil satuate current
Ivsat=20e-3
k_tune=6.66
Isat=k_tune*Ivsat
%Nm, load spring stiffness
KL=2 000
```

```
Xlim =0.001
% Constant = Cd*(2/Ro)^0.5
Ko =0.0293
%Resiatance to internal leakage

%PartB
%control loading
%parameters (units are converted from cm to m)
A = 15.22;                  %cm 2
A=Ap                        %using previous EHV
B1 =15434.74/100;           %N-m-sec (between 65434-15434)
c1 = 28.372*100;            %N-sec/m
%Ci = 89.309;               %cm^3 /sec-mA (5.45 in 3/sec-mA)
%Cp = 0.24243;              %cm^5/N-sec (0.0102 in5/lb-sec)
Fp = 427;                   %N (96 lb)
%G = 108466;                %N-cm/rad (9600 lb-in/rad)
Gmax= 325396/100;           %N-m/rad
G=Gmax/2;
%Gmax = 3253960;            %used for stability analyze
                            %to align zero DB lines coincide at same
                            %frequency for both rigid and compliant
                            %open-loop frequency response
lamda=0.1;                  %feedback network parameter
I = 677.91/100;             %N-m-sec 2
J = 422.56/100;             %N-m-sec 2
k = 10695*100;              %N/m
K1 = 0.0011240;             %V/N
K2 = 1.56/1000;             %A/V
K3 =3.0047*100;             %V/m
Rb = 25.4/100;              %m
Rp = 79.6925/100;           %m
alpha = 0.59;               %gear ratio
f=1/((Rp/Rb/alpha)*K1);     %The factor to equalize step inputs to
                            %model between the pilot force with
                           %respect to control column and the trim
                           %force from host
m_loadcell=0.1;            %Kg

%END
```

```
%%%%%%%%%%%%%%%%%%%%%%%%%%%%
%Control Loading State Space Representation%
%%%%%%%%%%%%%%%%%%%%%%%%%%%%
clear;
%parameters
A = 15.22;                          %cm 2 (2.36 in 2 )
B =15434.74;                         %N-cm-sec (304 lb-in-sec)(6-15)(G=Gmax/2, B=6434.74 N-cm-s)
c = 28.372;                         %N-sec/cm (16.2016 Ib-sec/in.)
Ci = 89.309;                        %cm^3 /sec-mA (5.45 in 3/sec-mA)
Cp = 0.24243;                       %cm^5/N-sec (0.0102 in5/lb-sec)
Fp = 427;                           %N (96 lb)
%G = 108466;                        %N-cm/rad (9600 lb-in/rad)
Gmax= 325396  ;                     %N-cm/rad (28 800 ib-in/rad)
Gmax=Gmax/2;
G=Gmax;
%Gmax = 3253960 ;                   %used for stability analyze
                                    %to align zero DB lines coincide at same
                                    %frequency for both rigid and compliant
                                    %open-loop frequency response
lamda=0.1;                          %MRAC parameter
I = 677.91;                         %N-cm-sec 2 (60 lb-in-sec 2 )
J = 422.56;                         %N-cm-sec2 (37.4 lb-in-sec 2 )
k = 10695;                          %N/cm (6107.86 lb/in.)
K1 = 0.0011240;                     %V/N (0.005 V/lb)
K2 = 1.56;                          %mA/V (1.56 mA/V)
K3 =3.0047;                         %V/cm (7.632 V/in.)
Ps = 827.28;                        %N/cm 2 (1200 lb/in2 )
qr = 1638.7;                        %cm 3 /sec (100 in 3 /sec)
Rb = 25.4;                          %cm (10 in.)
Rp = 79.6925;                       %cm (31.375 in.)
VE = 191.73;                        %cm 3 (11.7 in 3 )
alpha = 0.59;                       %gear ratio
beta = 172350;                      %N/cm 2 (250 000 lb/in2 )
xi= 0.2;                            %servovavle damping ratio
omega_n = 377;                      %rad/sec (377 rad/sec)
f=1/((Rp/Rb/alpha)*K1);             %The factor to equalize step inputs to
                                    %model between the pilot force with
                                    %respect to control column and the trim
                                    %force from host
K=0.2;                              %load cell inertial force factor
%%%
%%System with rigid linkage%%
%closed-loop: inner-loop feedback->K3*xp,outer loop feedback->loadcell
%state vector:[xp dotxp p qi dotqi delta dotdelta]'
%closed-loop (order 7)
Ar_cl=[0 1 0 0 0 0 0;               %closed-loop system matrice
        0 0 alpha^2*Rb^2*A/J 0 0 0 0;
        0 -4*A*beta/VE -4*beta*Cp/VE 4*beta/VE 0 0 0;
```

```
        0 0 0 0 1 0 0;
       -Ci*omega_n^2*K2*K3 0 0 -omega_n^2 -2*xi*omega_n Ci*omega_n^2*K2 0;
        0 0 0 0 0 0 1;
        0 0 -K*K1*G*A/I 0 0 -G/I -B/I];
Br_cl_Fp=f*[0 alpha*Rb*Rp/J 0 0 0 0 (1-K)*(Rp/Rb/alpha)*K1*G/I]';   %input
Br_cl_F=f*[0 0 0 0 0 0 0;                                          %n x n form
        0 0 0 0 0 0 alpha*Rb*Rp/J;
        0 0 0 0 0 0 0;
        0 0 0 0 0 0 0;
        0 0 0 0 0 0 0;
        0 0 0 0 0 0 0;
        0 0 0 0 0 0 (1-K)*(Rp/Rb/alpha)*K1*G/I];
Br_cl_T=[0 0 0 0 0 0 G/I]';                                        %input trim force
Cr_cl_xb=[1/alpha/0.62 0 0 0 0 0 0];                               %output xb. normalized divider:
                                                                   %0.56 fot T input
                                                                   %0.62 for Fp input
Cr_cl_Ap=[0 0 A*K1 0 0 0 0];                                       %output Ap
Cr_cl_T_loadcell=[0 0 -0.1*A*K1 0 0 0 0];                          %m_loadcell=0.1
Cr_cl_Fp_loadcell=[0 0 -K*A*K1 0 0 0 0];
Dr_cl_Fp_loadcell=[0 0 0 0 0 0 f*(1-K)*(Rp/Rb/alpha)*K1];
D=zeros;
%Fp
%closed-loop (Fp-->xb)
r_cl_Fp_xb=ss(Ar_cl,Br_cl_Fp,Cr_cl_xb,D);
%closed-loop (Fp-->Ap)
r_cl_Fp_Ap=ss(Ar_cl,Br_cl_F,Cr_cl_Ap,D);
%closed-loop (Fp-->loadcell)
r_cl_Fp_loadcell=ss(Ar_cl,Br_cl_F,Cr_cl_Fp_loadcell,Dr_cl_Fp_loadcell);
%T
%closed-loop (T-->xp)
r_cl_T_xb=ss(Ar_cl,Br_cl_T,Cr_cl_xb,D);
%closed-loop (T-->Ap)
r_cl_T_Ap=ss(Ar_cl,Br_cl_T,Cr_cl_Ap,D);
%closed-loop (T-->loadcell)
r_cl_T_loadcell=ss(Ar_cl,Br_cl_T,Cr_cl_T_loadcell,D)
%open loop(delta), eT input,i=K2*Ci*(eT-K3*xp) +f*(1-K)*(Rp/Rb/alpha)*K1)
%state vector:[xp dotxp p qi dotqi delta dotdelta]'
%rank(Ar_op)=7
Ar_op=[0 1 0 0 0 0 0;                                              %open loop system matrice
          0 0 alpha^2*Rb^2*A/J 0 0 0 0;
          0 -4*A*beta/VE -4*beta*Cp/VE 4*beta/VE 0 0 0;
          0 0 0 0 1 0 0;
         -Ci*omega_n^2*K2*K3 0 0 -omega_n^2 -2*xi*omega_n 0 0;
          0 0 0 0 0 0 1;
          0 0 K1*Gmax*A/I 0 0 -G/I -B/I];
Br_op_eT= [0 0 0 0 Ci*omega_n^2*K2 0 0]';                          %input eT
Cr_op_del=[0 0 0 0 0 1 0];                                         %output delta
```

```
%overall open loop eT-->delta
r_op_eT_del=ss(Ar_op,Br_op_eT,Cr_op_del,D);
%%%
%%System with compliant linkage, k, c
%closed-loop: inner-loop feedback->K3*xp, outer loop feedback->loadcell
%state vector:[xp p qi dotqi delta dotdelta xb dotxb]'
%closed-loop order 8
Ac_cl= [-k/c A/c 0 0 0 0 alpha*k/c alpha;                                    %closed-loop system matrice
        4*A*beta*k/VE/c -4*beta*(A^2+Cp*c)/VE/c 4*beta/VE 0 0 0 -4*A*beta*...
        alpha*k/VE/c -4*A*beta*alpha/VE;
        0 0 0 1 0 0 0 0;
       -Ci*omega_n^2*K2*K3 0 -omega_n^2 -2*xi*omega_n Ci*omega_n^2*K2 0 0 0;
        0 0 0 0 0 1 0 0;
        0  -K*K1*G*A/I 0 0 -G/I -B/I 0 0;
        0 0 0 0 0 0 0 1;
        0 alpha*Rb^2*A/J 0 0 0 0 0 0];
Bc_cl_Fp=f*[0 0 0 0 0 (1-K)*(Rp/Rb/alpha)*K1*G/I 0 Rb*Rp/J]';          %input Fp
Bc_cl_F=f*[0 0 0 0 0 0 0 0 ;                                          %input n x n
           0 0 0 0 0 0 0 0 ;
           0 0 0 0 0 0 0 0 ;
           0 0 0 0 0 0 0 0 ;
           0 0 0 0 0 0 0 0 ;
           0 0 0 0 0 0 0 (1-K)*(Rp/Rb/alpha)*K1*G/I ;
           0 0 0 0 0 0 0 0 ;
           0 0 0 0 0 0 0 Rb*Rp/J];
Bc_cl_T=[0 0 0 0 0 G/I 0 0]';                                          %input T, trim force
Cc_cl_xb=[0 0 0 0 0 0 1/0.76 0];                                       %output xb. normalized
divider
                                                                       %0.567 fot T input
                                                                       %0.76 for Fp input
Cc_cl_Ap=[0 A*K1 0 0 0 0 0 0];                                         %output press
Cc_cl_T_loadcell=[0 -0.1*A*K1 0 0 0 0 0 0];                            %m_loadcell=0.1
Cc_cl_Fp_loadcell=[0 -K*A*K1 0 0 0 0 0 0];
Dc_cl_Fp_loadcell=[0 0 0 0 0 0 0 f*(1-K)*(Rp/Rb/alpha)*K1];
%Fp
%closed-loop (Fp-->xb)
c_cl_Fp_xb=ss(Ac_cl,Bc_cl_Fp,Cc_cl_xb,D);
%closed-loop (Fp-->Ap)
c_cl_Fp_Ap=ss(Ac_cl,Bc_cl_F,Cc_cl_Ap,D);
%closed-loop (Fp-->loadcell)
c_cl_Fp_loadcell=ss(Ac_cl,Bc_cl_F,Cc_cl_Fp_loadcell,Dc_cl_Fp_loadcell);
%T
%closed-loop (T-->xb)
c_cl_T_xb=ss(Ac_cl,Bc_cl_T,Cc_cl_xb,D);
%closed-loop (T-->Ap)
c_cl_T_Ap=ss(Ac_cl,Bc_cl_T,Cc_cl_Ap,D);
%closed-lopp (T-->loadcell)
c_cl_T_loadcell=ss(Ac_cl,Bc_cl_T,Cc_cl_T_loadcell,D)
```

```
%open loop(delta), eT input,i=K2*Ci*(eT-K3*xp)
%state vector:[xp p qi dotqi delta dotdelta xb dotxb]'
%rank(Ac_op)=8
Ac_op= [-k/c A/c 0 0 0 0 alpha*k/c alpha;
        4*A*beta*k/VE/c -4*beta*(A^2+Cp*c)/VE/c 4*beta/VE 0 0 0 -4*A*beta*...
        alpha*k/VE/c -4*A*beta*alpha/VE;
        0 0 0 1 0 0 0 0;
        -Ci*omega_n^2*K2*K3 0 -omega_n^2 -2*xi*omega_n 0 0 0 0;
        0 0 0 0 0 1 0 0;
        0 K1*Gmax*A/I 0 0 -G/I -B/I 0 0;
        0 0 0 0 0 0 0 1;
        0 alpha*Rb^2*A/J 0 0 0 0 0 0];
Bc_op_eT=  [0 0 0 Ci*omega_n^2*K2 0 0 0 0]';                    %input eT
Cc_op_del=[0 0 0 0 1 0 0 0];                                    %output delta

%overall open loop (eT-->delta)
c_op_eT_del=ss(Ac_op,Bc_op_eT,Cc_op_del,D);

%%%stand alone analog computer model
%state vector:[delta dotdelta]'
A_m=[0 1;
     -G/I -B/I];
B_m_Fp=[0 G/I]';
C_m_del=[1 0];          %xb
model=ss(A_m,B_m_Fp,C_m_del,D);

%%% analize output
%%Bode, Gmax = 3253960, open loop(delta), eTinput,i=K2*Ci*(eT-K3*xp)
%bode(r_op_eT_del,c_op_eT_del)

%%step response (Fp step input with respect to control column)
 %step(model,r_cl_Fp_xb,c_cl_Fp_xb)
  step(r_cl_Fp_Ap,r_cl_Fp_loadcell,c_cl_Fp_Ap,c_cl_Fp_loadcell )


%step response (T step input, trim force from host)
  %step(model,r_cl_T_xb,c_cl_T_xb)
  %step(r_cl_T_Ap,r_cl_T_loadcell,c_cl_T_Ap,c_cl_T_loadcell )
%end
```